Joint Reconstruction of Longitudinal Positron Emission Tomography Studies for Tau Protein Imaging

Amal Tiss

SORBONNE UNIVERSITÉ

Joint Reconstruction of Longitudinal Positron Emission Tomography Studies for Tau Protein Imaging

A Dissertation
by

Amal Tiss

In Partial Fulfillment
of the Requirements for the Degree
Doctor of Philosophy
École Doctorale ED130 : Informatique, télécommunications et électronique de Paris

Sorbonne University
September 2019

Joint Reconstruction of Longitudinal Positron Emission Tomography Studies for Tau Protein Imaging

Reviewers:

Dr. Alain Prigent, Professor,
University Paris-Saclay

Dr. Vincent Lebon, Professor,
University Paris-Sud

TABLE OF CONTENTS

LIST OF TABLES

LIST OF FIGURES

LIST OF SYMBOLS AND ABBREVIATIONS

AD	Alzheimer's Disease
PET	Positron Emission Tomography
SPECT	Single Photon Emission Computed Tomography
MR	Magnetic Resonance
LOR	Line of Response
MLEM	Maximum Likelihood Expectation-Maximization
OSEM	Ordered Subsets Expectation Maximization
SUV	Standard Uptake Value
SUVR	Standard Uptake Value Ratio
PHF	Paired Helical Filament
ROI	Region Of Interest
EC	Entorhinal Cortex
FG	Fusiform Gyrus
HC	Hippocampus
ITG	Inferior Temporal Gyrus
PHG	ParaHippocampal Gyrus
STIR	Software for Tomographic Image Reconstruction
HABS	Harvard Aging Brain Study
CDR	Clinical Dementia Rating
MMSE	Mini Mental State Exam
NC	Normal Control
MCI	Mild Cognitive Impairment

SUMMARY

The accumulation of the paired helical filament tau protein leads to the cognitive decline seen in Alzheimer's disease (AD). The Positron Emission Tomography tracer, [^{18}F]-AV-1451, permits the observation of PHF tau in vivo. To determine the rate of tau deposition in the brain, the conventional approach involves scanning the subject two times (2-3 years apart) and reconstructing the images separately. Region-specific rates of accumulation are derived from the difference image which suffers from an increased intensity variation making this approach inadequate for clinical trial looking at the effect of a candidate drug on tau because the increased variation leads to a higher sample size required.

We propose a joint longitudinal image reconstruction where the tau deposition difference image is reconstructed directly from measurements leading to a lower intensity variation. This approach introduces a linear temporal dependency and accounts for spatial alignment, and the different injected doses.

We validate the reconstruction method by simulating higher tau accumulation in real data at different intensity levels. We additionally reconstruct the data from 123 subjects: 109 healthy subjects, 10 suffering from mild cognitive impairment, and 4 diagnosed with AD.

The joint reconstruction shows better contrast in the difference image obtained by the numerical simulations and a drastically reduced variance in the change of the Standard Uptake Value Ratio (SUVR) among subjects.

The decreased variance of our method leads to a smaller sample size for a potential clinical trial evaluating the effect of a candidate drug against AD.

Introduction

Positron Emission Tomography (PET) is a functional, nuclear imaging modality that has become an integral part of patient management in a clinical setting. Nuclear imaging permits the observation of a physiological process as opposed to anatomical imaging which show the structures inside the body. As we explain in **Chapter 1**, PET enables the imaging of the spatiotemporal distribution of a radiotracer injected in the patient's body. As the attached radionuclide undergoes a radioactive decay, a positron is emitted and eventually encounters an electron leading to the production of two annihilations 511 keV photons that are detected by the PET camera. Reconstruction algorithms, incorporating data correction factors, produce a quantitative image reflecting the distribution of the radiotracer which has been designed to target a specific process in the body. The multitude of radiotracers available explains the broad use of PET imaging in the clinic and research settings. In this work, we focus on one recently developed radiotracer: [^{18}F]-AV-1451 which permits the observation of the distribution of Paired Helical Filament (PHF) tau protein in the brain.

The appearance of excessive amounts of the PHF tau protein has been linked to the process of cognitive decline seen in dementia caused by Alzheimer's disease (AD). AD is an irreversible chronic neurodegenerative disease, the most common cause of dementia among the elderly. It is one of the biggest health problems facing our society. The cost of caring for AD patients is around $290 billion per year in the United States alone and is expected to increase as the population ages[1]. In **Chapter 2**, we give a brief presentation of AD and the role of tau protein in the disease. Recent histopathological and tau PET studies (using [^{18}F] AV-1451) suggest that prodromal AD may be monitored by following

the spread of PHF tau in the entorhinal cortex (EC), parahippocampal gyrus (PHG), fusiform gyrus (FG), inferior temporal gyrus (ITG), and the hippocampus (HC). We mainly focus on the role of PET imaging to accurately estimate the changes in tau protein deposition in the brain of subjects undergoing longitudinal studies.

The aim of this work, as presented in **Chapter 3**, is the development of a PET reconstruction framework enabling the estimation of tau deposition rate directly from two longitudinal [^{18}F] AV-1451 scans to improve the accuracy of diagnosis in early stages of AD and aid the development of treatments that halt its advancement. As we explain in **Chapter 4**, the proposed joint reconstruction framework for longitudinal studies results in a reduction in the variance of the estimated difference image as compared to the one produced using the conventional method consisting in taking the difference between images reconstructed separately. In **Chapters 5** and **6**, we apply our joint framework to simulations and to longitudinal patient studies. The validation of the joint method is discussed in **Chapter 7**, first by comparing the images obtained after considering a single scan from a patient study to the clinical image; second, by evaluating the results on the simulations. In **Chapter 8**, we present the results applied to the patient cohort and use them to derive sample sizes for both methods for a hypothetical clinical trial aiming at separating between groups exhibiting different rates of tau accumulation. Finally, in **Chapter 9**, we discuss the limitations of the proposed approach and provide an alternative formulation for the reconstruction problem using temporal priors.

PART I BACKGROUND

CHAPTER 1. Positron Emission Tomography

Positron Emission Tomography (PET) is a powerful imaging technique that provides quantitative evaluation of imaged tissues. It has been reported as the most specific and sensitive technique for *in vivo* imaging of molecular interactions[2] as its performance exceeds by far that of Single Photon Emission Computed Tomography (SPECT)[3]. The quantitative information inferred from PET images enables a fast and reliable assessment of various conditions, leading to the prevalence of PET imaging in clinical applications[4]. In this chapter, we discuss the physical foundations[5], [6] of PET imaging from the radioactive decay to the photon detection in the scanner. The measurements are then converted to PET data that are reconstructed into images after applying several corrections techniques.

1.1 Physical Foundations

A PET study begins by the injection of a radioactive tracer in the patient's body. Different tracers can be used depending on the purpose of the study. The process of radioactive decay leads to positron emission inside the patient's body. As a positron encounters an electron, annihilation occurs, which leads to the emission of two 511 keV photons travelling in almost opposite directions. The PET scanner detects photon pairs and backtracks their paths to localize the annihilation points, thereby generating a map of the distribution of the radiotracer: a PET image.

1.1.1 Radiotracers

The radiotracer is a compound formed by attaching a radionuclide to a molecule to enable the tracking of said molecule inside the patient's body. Two important principles govern the radiotracer design: it is assumed to behave the same way as the original molecule or at least in a known and predictable matter, and its mass and/or concentration should not interfere with the physiologic process that is being imaged.

Fluorine 18 (^{18}F) is widely used as the labelling radionuclide in PET imaging: its half-life of 109 minutes is long enough to perform an imaging study and short enough to limit the radiation exposure. The most used radiotracer is fluorodeoxyglucose [^{18}F]-FDG which is a marker for tissue uptake of glucose and has become indispensable in oncology. Table 1 below presents examples of radiotracer and the corresponding physiological processes they target.

Isotope	Radiotracer	Function
^{18}F	[^{18}F]-FDG	Glucose uptake in heart[7], lungs[8], brain[9], and tumors[10]
	[^{18}F]-FMISO	Tissue hypoxia [10], [11]
	[^{18}F]-FLT	DNA replication for tumor cell proliferation[12]
	[^{18}F]-AV-1451	Tau accumulation in the brain[13]
^{11}C	[^{11}C]-Choline	Membrane biosynthesis for tumor cell proliferation[14]
	[^{11}C]-PIB	β-amyloid plaques in the brain[15]
^{13}N	[^{13}N]-NH3	Myocardial perfusion[16]
^{15}O	H_2[^{15}O]	Myocardial[16] and cerebral[17] perfusion

Table 1: Imaging of different physiological processes using different PET tracers

1.1.2 Radioactive decay and interactions

A positron emitting radionuclide (${}^{A}_{Z}X$) decays to a stable nucleus (${}^{A}_{Z-1}Y$) by emitting a positron (e^{+}) and an electron neutrino (ν_e):

$$ {}^{A}_{Z}X = {}^{A}_{Z-1}Y + e^{+} + \nu_e $$

For example, ^{18}F, with 9 protons and 9 neutrons, decays to ^{18}O which a stable isotope of oxygen with 8 protons and 10 neutrons, by emitting a positron.

The positron and the neutrino are ejected with the kinetic energy produced by the decay. The positron loses its energy after few collisions with its surrounding atoms. Once it slows down, it annihilates with an electron. The rest energy of both the positron and the electron is 511 keV. The annihilation leads to the appearance of two 511 keV photons that are travelling in almost opposite directions.

In practice, the positron is not fully stopped when it interacts with the electron. As a result, the photons are not perfectly collinear: they form an angle deviating from the theoretical 180° by a few tenths of a degree. Since PET imaging relies on the photons path to recover the location of the annihilation event, the non-collinearity of the photons limits the spatial resolution of the PET system. Furthermore, the distance travelled by the positron before annihilation occurred – called the positron range – introduces uncertainty about the real spatial distribution of the radiotracer: the image reflects the location of the annihilation event, not the location where the radioactive decay occurred. In the case of the ^{18}F tracer, the positron range is estimated between 0.6 mm and 2.4 mm in water[18], and the angle between the annihilation photons ranges from 179.75° and 180.25°[19].

As the emitted photons travel through the matter, they undergo two types of interactions that are important in PET imaging:

- Photoelectric effect: the photon is absorbed by an atom and an electron is emitted.
- Compton scattering: the photon is deflected after it collides with an electron in the outer shell of an atom. It loses some of its energy, but it is not completely absorbed by the atom as in the photoelectric effect. The angle between the incident photon and the deflected one can vary from 0 to 180°[20].

As a result, the photons detected by the PET scanner may display a different energy and a different direction from what is expected after an annihilation. These are known as scattered events.

1.1.3 Coincidence detection

A PET scanner contains blocks of photons detectors arranged in concentric rings around the object to be imaged. Figure 1 shows the configuration of a scanner with 4 block detector rings where two annihilation photons reach two detector blocks in opposite sides.

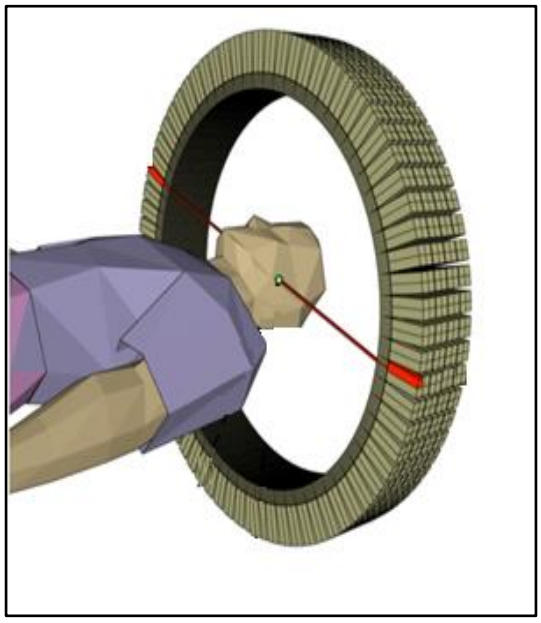

Figure 1: Schema of a PET scanner. It is composed of 4 block detector rings. The red line shows two annihilations photons reaching two detector blocks in opposite sides.

Most detectors in commercial scanners are inorganic scintillation detectors[21] whose role is to absorb the incident photon and convert it to many visible light photons. A photomultiplier tube detects these photons and produces a proportional electric signal that contains information about the time when the incident photon was

detected, as well as its energy. A pulse-height analysis is then performed to record annihilation events: only a pair of collinear photons each at 511 keV arriving to the detectors at the same time constitute a counted event. In practice, a temporal window, around 10 ns[6], defines the accepted delay between the photons and an energy window, generally set to (440 keV, 650 keV)[6], defines the accepted deviation from the ideal 511 keV level for the detected photons.

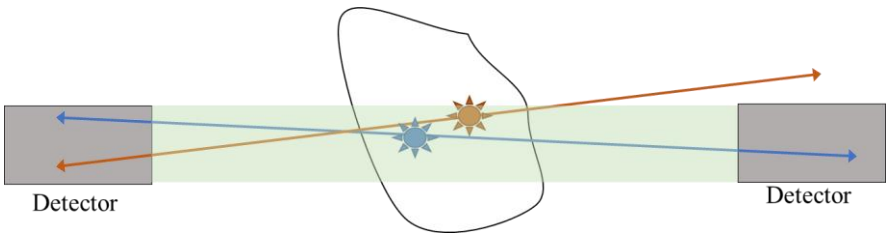

Figure 2: Annihilation events: accepted (Blue) and rejected (Brown) by coincidence detection.

Figure 2 shows an example of an annihilation event (in blue) that has been counted by a pair of the detectors, if the photons arrive within the temporal window and with an accepted energy. The annihilation event in brown is not counted for the shown pair of detectors as one of the resulting photons is outside of the green area, which represents a 3D tube linking the two detectors, and therefore it is not detected. Every time an annihilation event occurs in that tube – if the resulting photons remain inside the tube, the number of events recorded for that pair of detectors is incremented. The 3D tube between the two detectors is commonly called the Line of Response (LOR).

Based on their detected positions, their energies, and the times of the detection, some photons resulting from annihilation events are discarded. The opposite can also occur: the scanner incorrectly records events known as random coincidences. In Figure 3, the scanner increments the count of the LOR shown by the dashed lines leading to incorrect positioning of the true annihilation events[5]:

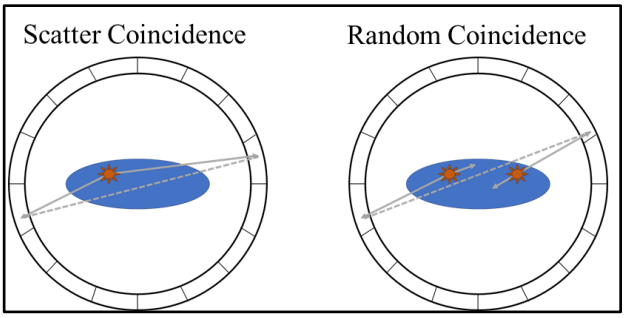

Figure 3: Scatter and random coincidences

- Scatter coincidence occurs when one photon is scattered and is therefore recorded in a detector different from the one that would be involved in the true LOR. Even if the scattered photon ends up hitting the detector with a small delay compared to the other photon involved in the annihilation event, the time difference is usually smaller that the temporal window.
- Random coincidence occurs when two annihilation events are mistakenly recorded as one. For example, if two photons from two unrelated annihilation events get absorbed in the imaged body and the two remaining photons hit a pair of opposing detectors within the temporal window, then the scanner will increment the counted events for that LOR although no annihilation occurred along that line.

The process of coincidence detection sometimes rejects true events and counts false ones. This contributes to the loss of contrast in the PET images. However, there are techniques to correct for some of these effects (Section 1.2).

1.1.4 Data formation

PET data acquisition can be performed in 2D or 3D modes, as shown in Figure 4. In 2D PET mode, lead septa are used to only allow the detection of coincidences in the same ring or in adjacent rings. This acquisition scheme leads to a reduction in accidental coincidences but also a reduction in the scanner sensitivity. The septa are removed in 3D mode so that coincidence from different planes can be detected[6].

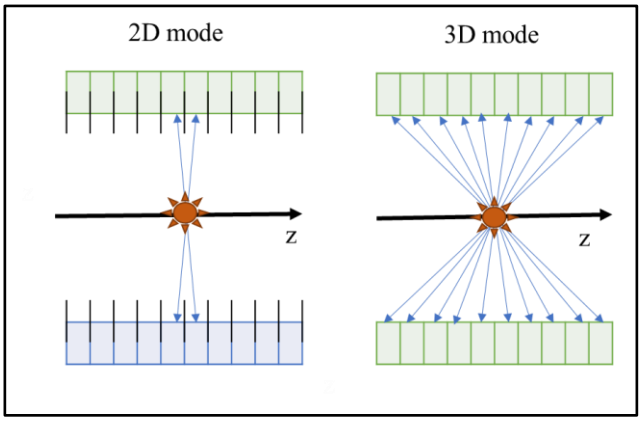

Figure 4: 2D and 3D acquisition modes

2D PET imaging sees the volume as transverse slices along the z axis. The LOR contained inside the specified plane is parametrized with an angle ϕ and its distance from the center s as shown in Figure 5. For a given plane z and a given direction ϕ, the LORs are defined by their distances from the center. Each is assigned the number of annihilation events counted by the pair of the detectors. The set of LORs for varying directions and distances from the center is called a sinogram. Once the events along the LORs from all the slices forming the volume have been counted, we obtain a three-dimensional table composed by the superposition of sinograms from different planes.

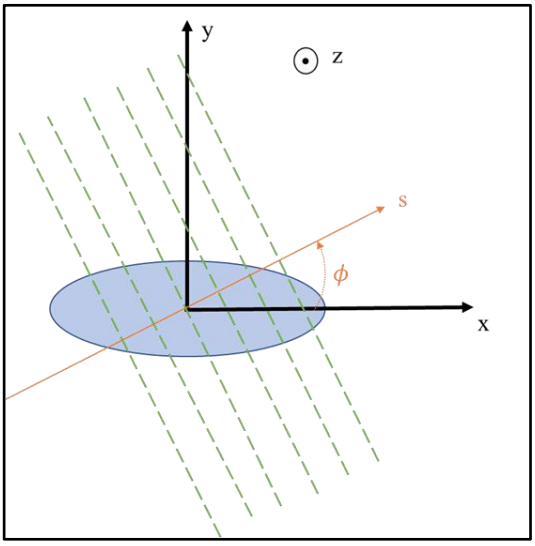

Figure 5: Parametrization of a LOR

The LORs composed by a pair of detectors in the same ring are called “direct”. Oblique planes link detectors from different rings as illustrated in Figure 4 and yield “indirect” LORs which are also organized in sinograms.

The PET data collected by the scanner is a matrix indexing every possible LOR and saves its assigned count reflecting the distribution of the radiotracer along that LOR. Image reconstruction algorithms transforms these measurements into a 3D image. However, some correction techniques should be applied to yield a quantitative image.

1.2 Corrections toward quantitative PET

To ensure that the reconstructed image truly reflects the underlying function, correcting for physical phenomena negatively affecting the detections is necessary. We have already discussed sources of errors in PET imaging resulting from the positrons and the photons interactions in the imaged object. We will describe how we can correct their effects when possible.

1.2.1 Random coincidences correction

Random coincidences occur when two unrelated annihilation events lead to two detected photons within the temporal window as shown in Figure 3. Their spatial distribution is uniform across the field of view and is nearly independent from the imaged object, as opposed to true coincidence which reflect the distribution of the radiotracer. Therefore, the fraction of random detections is higher for regions where true coincidences are highly attenuated and can lead to more pronounced quantitative errors in these regions.

To estimate the number of random coincidences, two methods exist:

- Single rates: The rate C_{ij} of random coincidences in a specified LOR (i, j) is a function of the temporal window length (2τ) and the rate of single counts in the detectors i and j forming that LOR[22], noted r_i and r_j: $C_{ij} = 2\tau r_i r_j$. The total number of random coincidences in that LOR is then estimated over the acquisition time T if the radiotracer redistribution is ignored[23]: $R_{ij} = \frac{2\tau}{T} R_i R_j$ where R_i is the total number of single photons counted in the detector i.
- Delayed coincidence channel[22]: the temporal window is delayed by a duration equal to many times its width so that the coincidences in the delayed window cannot arise from the same annihilation event or scattered photons. The counts detected in the delayed window is a direct measure of the number of random coincidences and are assumed to be the same in original temporal window as coincidences in both windows are subject to the same counting limitations.

The delayed coincidence channel is the most commonly implemented technique[24] as it is the most accurate. However, it propagates the noise of the estimated random coincidences directly into the corrected data.

1.2.2 Compton scatter correction

As photons travel through matter following annihilation events, they can be deflected from their original trajectory when they undergo a Compton scatter interaction. As a result, the annihilation event will be assigned to the wrong LOR (Figure 3). Scatter coincidences will induce large quantification errors if left uncorrected as they represent a large fraction of the measured coincidences.

Analytical estimation of the scatter is possible under the assumption that only one of the annihilation photons is scattered once. In that case, the following formula[25] gives the single scatter coincidence rate in the LOR of the detectors i and j:

$$D_{ij} = \int_V \left[\frac{\sigma_{iP}\sigma_{jP}}{4\pi d_{iP}^2 d_{jP}^2} \frac{\mu}{\sigma_c} \frac{d\sigma_C}{d\Omega} (I_i + I_j) \right] dV$$

- P is a moving point in the integration volume (noted V) where the Compton scattering occurs.
- σ_{iP} is the cross section of the detector i as seen from the point P.
- $d_{ip}$is the distance between the detector i and the scattering point P.
- μ is the attenuation coefficient in the point P.
- $\frac{d\sigma_c}{d\Omega}$ is the differential Compton scattering cross-section derived from the Klein-Nishina formula.
- I_i calculated the intensities of the attenuated photons if the scattered photon arrives on the detector j. The opposite case, where the scattered photon reaches the detector i, is accounted for in the twin term I_j.

The analytical estimation of the scatter is computationally expensive; thus, it is only performed in a reduced number of points picked randomly in the attenuation volume. It also requires the prior knowledge of the activity distribution: an iterative scheme is thus needed. First, the activity distribution is estimated without the scatter correction, then, the scatter is estimated using the analytical calculation. Finally, the scatter correction can be incorporated into the estimation of the activity distribution.

The analytical solution for scatter estimation is fast and noise free. However, it only accounts for single scatter events. This assumption is reasonable as a single scatter occurs in 75% to 80% of all scattering events in a ring of 10 cm axial field of view[26]. This means that the solution underestimates scatter by around 20%. Instead of modeling multiple scattering events or performing Monte Carlo calculations, it is possible to scale the obtained scatter sinogram to account for all scattering events. All the events detected

outside of the subject are due to Compton scattering. The ratio between these events and the simulated single scatter outside of the subject thus provides the scaling factor between the multiple scatter events and the single ones. It is therefore applied to the obtained single scatter sinogram to obtain an accurate estimation of all scattering events.

1.2.3 Attenuation correction

Attenuation correction aims to correct for photons that should have been detected but they were not either because they were completely absorbed or because their energy/direction following different interactions led the detection analyses to discard them.

In PET, the attenuation of the annihilation photons is independent of the position of the annihilation event along the LOR: for a homogenous object, the probability of detecting the pair of the photons is $p = \exp(-\mu T)$ where T is the thickness of the object, and μ is the linear attenuation coefficient of the tissue comprising the imaged object at 511 keV. The attenuation coefficient is around 0.095 cm^{-1} for soft tissue, between 0.12 and 0.14 cm^{-1} for bone, and around 0.04 cm^{-1} in the lungs[6].

Attenuation correction techniques rely on the estimation of the attenuation along all the LORs. It can be done by comparing the count rate from an external transmission source (transmission scan) with the count rate from the same source without the subject (blank scan). The ratio between the counts of transmission scan and those of the blank scan yields an estimation of the probability that the photons are not absorbed in each LOR: $\exp\left(-\int_{LOR} \mu(l)dl\right)$ [5].

Nowadays, most commercial PET scanners are combined systems incorporating both PET and CT imaging[27]. A CT scan measures the attenuation of photons after they travel through the patient body along each LOR. This is the measure we are trying to estimate to correct for photons attenuation in the PET image. An empirical bilinear function[28] permits the conversion of the attenuation coefficients measured by the CT scan to their equivalent at the PET energy level (511 keV).

1.2.4 Detector normalization

A PET scanner houses thousands of individual detectors. Inevitably, they will display variations in their performance[6]: some are due to intrinsic factors (crystal imperfections, difference in PMT gains, variation in the electronics used to detect signal…), others are geometric (the position of the detector in the ring/block , the incidence angle of the detected photon…). These variations are linked to the scanner itself and are independent of the imaged object. Correction for these effects is called normalization.

If all the detectors are exposed to the same radiation source, the difference in detected counts reflects directly the variation across the detectors. The blank scan used to derive the attenuation probability across LOR accomplishes the same outcome: all detector pairs receive the same number of annihilation photons after one revolution of the external source around the field of view. A noisy estimation of the normalization factors will affect the noise levels in the true coincidences counts. To diminish the noise in the normalization correction, a long acquisition is needed which is not always feasible. Instead, the factors are decomposed into many components each reflecting one source of variation. The estimation of these new factors can be done using simple phantoms, low activity levels,

and long acquisitions as they are dependent on the scanner and don't need to be repeated for each scan[29].

1.3 Tomographic Image Reconstruction

We have seen in Section 1.1.4 how the scanner saves the acquisition data in a matrix where each element represents one LOR and stores its corresponding count. Many factors undermine the accuracy of the recorded counts and correction techniques need to be implemented to get reliable data (Section 1.2). The next step consists in transforming the count data to a 3D image representing the distribution of the radiotracer in the imaged object. The transformation is known as tomographic image reconstruction.

Two types of algorithms are applied to the PET image reconstruction: the analytical methods which are based on an over-simplified model of the measured data and the iterative methods which use a more accurate model of the physical effects involved in PET imaging. In the following section, we present the widely used iterative reconstruction algorithm: Ordered Subsets Expectation Maximization (OSEM)[30].

1.3.1 Iterative reconstruction

The general concept of an iterative reconstruction algorithm is shown in Figure 6: the imaged object is approached by successive estimates, iteratively updated using the difference between the calculated projections from the preceding iteration and the real measured projections. The approximation is repeated until the difference between the measured data and the calculated projections is minimal. The latest estimate gives the reconstructed image.

From Figure 6, we can identify the five ingredients on an iterative reconstruction algorithm, the data model (the representation of the measured projections), the image model (based on the discretization of the field of view in contiguous and non-overlapping voxels), the system matrix (the link between the image model and the data model), the cost function (the comparison between the measured and the calculated projections), and the optimization algorithm (the definition of the update step in each iteration).

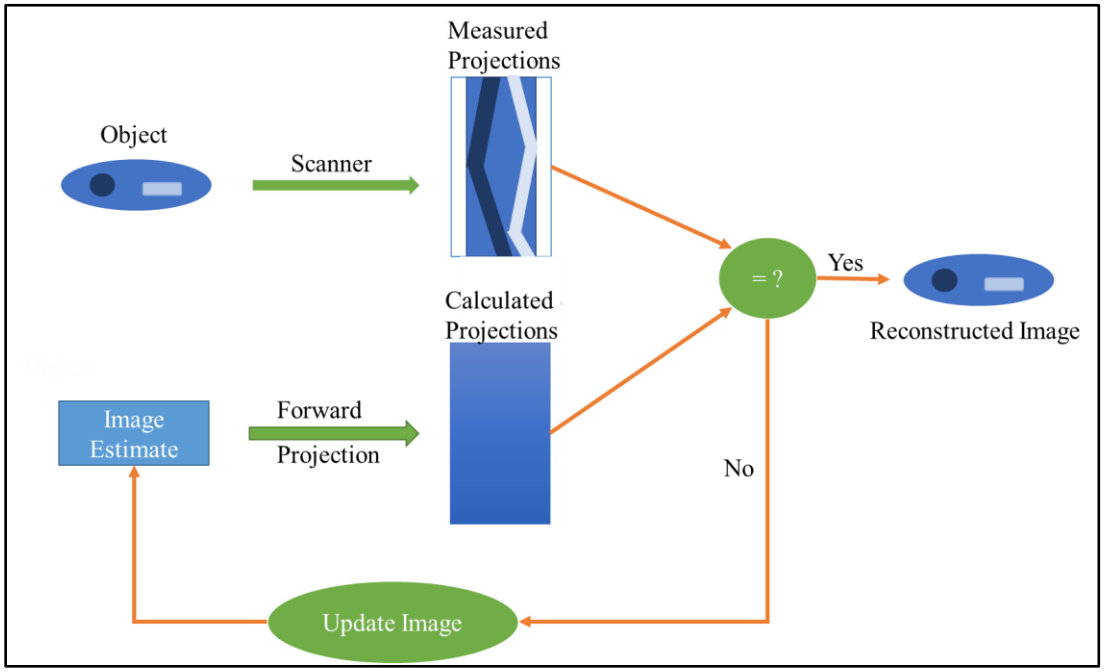

Figure 6: Principle of iterative reconstruction algorithms

To simplify the representation of the data, a single index j is used to define the LOR between two detectors (k,l). n_j denotes the number of events detected for the LOR j. The PET data is the result of photons annihilation following the emission of a positron in the radioactive decay process. Therefore, the n_j are distributed as independent Poisson variables[5]. The likelihood function defined as the probability of measuring the counts n_j as a function of the parameter to estimate (here, the image $\boldsymbol{\lambda}$) is given by:

$$L(\boldsymbol{\lambda}|\boldsymbol{n}) = \prod_{j=1}^{K} \frac{exp(-p_j)\, p_j^{nj}}{n_j!} \quad (1)$$

where K is the total number of LORs, and p_j is the expected value of the counts detected for the LOR j.

Likewise, the image $\boldsymbol{\lambda}$ is represented as a column vector of activity values in its voxels. Let's note M the number of the voxels in the image. The discretized problem is then composed of linear equations:

$$p_j = \sum_{i=1}^{M} h_{j,i}\lambda_i \quad (2)$$

The elements $h_{j,i}$ express the probability of detecting a primary emission from the voxel i in the LOR j. The system matrix $\boldsymbol{H}$, composed of the elements $h_{j,i}$, has the size $\boldsymbol{K} \times \boldsymbol{M}$. The vector form of the reconstruction problem is written: $\boldsymbol{p} = \boldsymbol{H\lambda}$, where $\boldsymbol{p}$ is a column vector $\boldsymbol{p} = \overline{\boldsymbol{n}}$.

In iterative reconstruction algorithms, a current image is fed to the system matrix yielding calculated projection data (Figure 6) that can be compared to the measured data. This comparison is enabled by the cost function. In the OSEM algorithm, the cost function is defined as the natural logarithm of the likelihood $L(\boldsymbol{\lambda}|\boldsymbol{n})$ in Equation (1):

$$\ln\big(L(\boldsymbol{\lambda}|\boldsymbol{n})\big) = \sum_{j=1}^{K} -p_j + n_j \ln\,(p_j) - \ln n_j! \quad (3)$$

Incorporating the forward model in Equation (2), we obtain:

$$\ln\big(L(\boldsymbol{\lambda}|\boldsymbol{n})\big) = \sum_{j=1}^{K}\left(-\sum_{i=1}^{M} h_{j,i}\lambda_i + n_j \ln\left(\sum_{i=1}^{M} h_{j,i}\lambda_i\right) - \ln n_j!\right) \quad (4)$$

The reconstructed image estimate is given by:

$$\hat{\boldsymbol{\lambda}} = \underset{\boldsymbol{\lambda}}{\operatorname{argmax}}\big(\ln\big(L(\boldsymbol{\lambda}|\boldsymbol{n})\big)\big) \quad (5)$$

If we ignore the terms that are independent from $\boldsymbol{\lambda}$, we finally obtain:

$$\hat{\boldsymbol{\lambda}} = \underset{\boldsymbol{\lambda}}{\operatorname{argmax}}\left(\sum_{j=1}^{K}\left(-\sum_{i=1}^{M} h_{j,i}\lambda_i + n_j\, ln\left(\sum_{i=1}^{M} h_{j,i}\lambda_i\right)\right)\right) \quad (6)$$

The optimization algorithm solves the problem defined in Equation (6) and yields the current estimated image.

To derive the Expectation-Maximization (EM) algorithm[31] used in OSEM, we need to look at the *complete* data: the measured data $\boldsymbol{n}$ is *incomplete* because it only gives the number of counts in LORs, but we ignore what fraction of these counts originated from a specific voxel. The complete data is defined as the number of counts detected in a LOR j and originated from the voxel i and it is noted $N_{j,i}$. The maximum likelihood for the complete data is given by:

$$L(\boldsymbol{\lambda}|\boldsymbol{N}) = \prod_{j=1}^{K}\prod_{i=1}^{M} \frac{\exp\big(-p_{j,i}\big)\, p_{j,i}^{N_{j,i}}}{N_{j,i}!} \quad (7)$$

where $p_{j,i}$ is the mean value of the counts in the LOR j that came from the voxel i. As we have previously stated, the probability of detecting an event in the LOR j originating in the

voxel i is given by the element $h_{j,i}$ of the system matrix. We have then: $p_{j,i} = h_{j,i}\lambda_i$. Finally, the log-likelihood for the complete data, noted $l(\boldsymbol{\lambda}|\boldsymbol{n})$, is given by:

$$l(\boldsymbol{\lambda}|\boldsymbol{n}) = \sum_{j=1}^{K}\sum_{i=1}^{M} -h_{j,i}\lambda_i + N_{j,i}\ln\left(h_{j,i}\lambda_i\right) - \ln\left(N_{j,i}!\right) \quad (8)$$

In the EM algorithm, instead of maximizing the log-likelihood directly, we want to maximize its mean value. If we note $\boldsymbol{\lambda}^k$ the estimated image at the iteration k of the optimization algorithm, then the expectation step of the EM gives:

$$\mathbb{E}[l(\boldsymbol{\lambda}|\boldsymbol{n})|\,\boldsymbol{n},\boldsymbol{\lambda}^{(\boldsymbol{k})}] = \sum_{j=1}^{K}\sum_{i=1}^{M} -h_{j,i}\lambda_i + \mathbb{E}\left[N_{j,i}|\boldsymbol{n},\boldsymbol{\lambda}^{(\boldsymbol{k})}\right]\, ln\left(h_{j,i}\lambda_i\right) - \mathbb{E}\left[ln\left(N_{j,i}!\right)|\,\boldsymbol{n},\boldsymbol{\lambda}^{(\boldsymbol{k})}\right] \quad (9)$$

The $N_{j,i}$ are Poisson distributed so the conditional probability distribution given their sum (since $n_j = \sum_{i=1}^{M} N_{j,i}$) is a binomial distribution with parameters $\left(n_j, \frac{h_{j,i}\lambda_i}{\sum_{q=1}^{M} h_{j,q}\lambda_q}\right)$. Therefore, the expectation of the complete data given their sum and the current image is:

$$\mathbb{E}\left[N_{j,i}|\boldsymbol{n},\boldsymbol{\lambda}^{(k)}\right] = n_j\,\frac{h_{j,i}\lambda_i^{(k)}}{\sum_{q=1}^{M} h_{j,q}\lambda_q^{(k)}} \quad (10)$$

We can ignore the last term in Equation (9) because it will be set to zero in the maximization step as it is independent of $\boldsymbol{\lambda}$.

The maximization step consists in differentiating the Equation (9) with respect to a voxel λ_l and setting the derivative to zero. Finally, we obtain the update formula:

$$\lambda_l^{(k+1)} = \frac{\lambda_l^{(k)}}{\sum_{j=1}^{K} h_{j,l}} \sum_{j=1}^{K} \frac{h_{j,l} n_j}{\sum_{q=1}^{M} h_{j,q} \lambda_q^{(k)}} \quad (11)$$

The Maximum Likelihood Expectation Maximization (MLEM) algorithm in Equation (11) is guaranteed to converge and it is unbiased[32]. However, it may require many iterations to reach convergence. The resulting image, after many iterations, is then too noisy to be useful in practice. To minimize the noise level in the reconstructed image, the process is stopped before reaching convergence and therefore bias is introduced in the final image. Around 100 iterations are still needed to get a reasonable solution. OSEM has been introduced to speed up the convergence: for every iteration, the measurements $\boldsymbol{n}$ are separated into subsets and the update step of the MLEM algorithm is applied multiple times, each time using the data from a single subset. This technique is widely used in clinical applications because it yields images like the MLEM's solution with a decreased reconstruction time. However, OSEM does not converge to the maximum-likelihood solution because not all the data is used for each update step[33].

We have derived the MLEM algorithm as an example of an iterative reconstruction algorithm. We have explained how it can be modified to get the widely used OSEM version. The question that we try to answer next is how to incorporate the data correction techniques seen in Section 1.2 in the reconstruction framework.

1.3.2 Corrected PET data reconstruction

We have previously introduced the elements of the system matrix $\boldsymbol{H}$ as the probability for a positron emitted in voxel i to be detected without scattering in LOR j. The matrix H can, in fact, be decomposed in a product of matrices, each modeling one phenomenon of the

acquisition scheme: $\boldsymbol{H} = \boldsymbol{SAG}$. $\boldsymbol{G}$ incorporates the geometry of the scanner and gives the geometric probability of detecting an annihilation event from the voxel i in the LOR j. $\boldsymbol{G}$ has the same size as the system matrix $\boldsymbol{H}$. $\boldsymbol{S}$ and $\boldsymbol{A}$ are diagonal matrices of size $K \times K$ containing the sensitivity (Section 1.2.4) of the LORs and their attenuation factors (Section 1.2.3), respectively.

The effect of the scattered and the random coincidence is seen directly in the measurements: $\boldsymbol{n} = \boldsymbol{t} + \boldsymbol{d} + \boldsymbol{r}$, where $\boldsymbol{t}$ reflects the number of true coincidences counted in each LOR, $\boldsymbol{d}$ is the number of scattered coincidences, and $\boldsymbol{r}$ is the number of random coincidences. t_j,d_j, and r_j are Poisson distributed, their sum is also Poisson. The mean of the t_j, true coincidences in the LOR j, is p_j as described in Equation (2). Let's note $\overline{d_j}$ and $\overline{r_j}$ the mean values of d_j and r_j. Then: $\mathbb{E}[n_j] = \sum_{i=1}^{M} h_{j,i}\lambda_i + \overline{d_j} + \overline{r_j}$. Additionally, the elements of the system matrix are rewritten as $h_{j,i} = a_j s_j g_{j,i}$ to show the contribution of the attenuation coefficients and the normalization factor. We can finally follow the same steps performed in Section 1.3.1 to rewrite the problem for the EM algorithm and obtain the following update step[31]:

$$\lambda_l^{(k+1)} = \frac{\lambda_l^{(k)}}{\sum_{j=1}^{K} a_j s_j g_{j,l}} \sum_{j=1}^{K} \frac{a_j s_j g_{j,l} n_j}{\sum_{q=1}^{M} a_j s_j g_{j,q} \lambda_q^{(k)} + \overline{d_j} + \overline{r_j}} \quad (12)$$

With the incorporated PET data corrections, the reconstruction algorithm yields a quantitative PET image which can be analyzed in a clinical setting.

1.4 Clinical applications of PET

The multitude of radiotracers and their different functions illustrated in Table 1 explains how prevalent PET imaging in patient management is. We focus on three main areas in this section.

1.4.1 Oncology

PET imaging serves primarily as a diagnostic tool in oncology. The widely used [^{18}F]-FDG tracer enables the imaging of glucose uptake in the body. Since most cancerous cells are glucose avid, the resulting PET images show an increased uptake where tumors are located[34]. This ability makes PET imaging valuable not only for diagnoses but also for patient management throughout their care as it can detect residual disease post-treatment. It is an integral part of the patient follow-up owing to its ability to distinguish between post-treatment scarring and active tumor recurrence[35].

Tumor detection and post-treatment imaging usually relies on a qualitative interpretation of the image. In oncology, a semi-quantitative metric has been introduced: Standard Uptake Value (SUV) is derived from the image and it reflects how much of the injected activity is concentrated in that region and/or voxel; it plays a major role in therapy assessment[36]. Tracking the change of the SUV following treatment helps determine how well the patient is responding to therapy and if a change of his/her course of treatment is needed.

Additionally, [^{18}F]-FDG PET imaging is present in radiation oncology. The therapy consists in defining the volume around the tumor and irradiating it. It is necessary to cover the whole volume where tumor cells are present for better outcome. It can be beneficial to

incorporate functional imaging in the definition of the contours of the regions to be targeted by radiation[37].

Finally, other radiotracers should be mentioned in cancer management: [^{18}F]-FMISO which detects hypoxia in tumors to inform about their potential resistance to treatment[10], [^{11}C]-Choline [14] and [^{18}F]-FLT which are both markers for tumor proliferation [12] and are used in patient follow-up.

1.4.2 Cardiology

PET imaging enables the measurements of myocardial perfusion using the tracer [^{13}N]-NH3 and myocardial viability using the tracer [^{18}F]-FDG. The former permits the comprehensive evaluation of the hemodynamic consequences of coronary artery disease (CAD) even before it becomes symptomatic, thus giving subjects with low cardiovascular risk earlier access to preventive therapy[38]. It is possible to monitor patients' response to therapy or lifestyle changes thanks to the quantitative measure of myocardial perfusion. [^{18}F]-FDG PET has also a high diagnostic value in assessing the myocardial viability of subjects with known CAD[7]. This assessment is very important considering that it is closely related to the risks and benefits of medical treatments and/or revascularization.

1.4.3 Neurology

PET imaging of the brain encompasses many areas. Naturally, one of the most prevalent uses is the diagnostic and management of brain cancers. As with most tumors, an increased [^{18}F]-FDG uptake is indicative of cancer in the brain. [^{18}F]-FDG is not the only tracer used in brain cancer: [^{18}F]-FMISO, H_2[^{15}O], and [^{18}F]-FLT have been used to assess hypoxia,

perfusion, and proliferation (respectively) in tumors[39], [40]. In the case of gliomas, [^{18}F]-FDG PET imaging findings have been linked to the tumor grade and the survival rates[41]. In epilepsy, it permits the localization of the seizure focus[42] needed in the case of required surgical therapy[43].

In addition, [^{18}F]-FDG PET is a biomarker for neuronal degeneration in dementia[44]: its spatial distribution enables clinicians to make early diagnosis and to distinguish between different subtypes of dementia[45]. Many other tracers have been developed for PET imaging in dementia. In the next chapter, we study their use to image tau protein in relation to AD.

CHAPTER 2. Tau Protein in Alzheimer's Disease

Alzheimer narrated his discovery of a new disease[46] after observing one patient in a mental health facility. He described her rapid memory loss and her spatial and temporal confusion. He noted a rapid decline in her cognition and behavior. She was believed to be delusional and incoherent in her answers and actions. Her case was unusual because of her young age: her ordeal started in her early fifties. Upon her death, Alzheimer performed an autopsy on her brain and discovered a general atrophy of the brain and noted the presence of fibrils inside of normal-appearance cells and the deposition of a substance in the cortex: Alzheimer was then describing the tangles (tau protein) and the plaques (amyloid protein) that define AD. In this chapter, we give a brief introduction of the disease and we focus on PET imaging of tau protein.

2.1 Alzheimer's disease

AD is an irreversible neurodegenerative disease and the most common cause of dementia among the elderly. Its symptoms consist in memory loss, language impairment, and a loss in the ability to recognize objects and/or people.

Age[47] is the most important risk factor for developing AD but there are many others such as environmental and genetic factors.

AD is characterized by the presence of two abnormal structures in histopathology studies: plaques (deposits of amyloid protein) and tangles (deposits of tau protein).

2.1.1 Clinical signs

The disease progression can be separated in three phases[48]: pre-clinical, mild cognitive impairment (MCI) due to AD, and dementia. The first phase can last up to decades and reflects the long and slow formation of tangles and plaques seen in AD but without the manifestation of any cognitive decline. The second phase corresponds to the appearance of the first clinical signs of AD; however, the tentative diagnosis is made in accordance to other biomarkers and imaging techniques and by eliminating other causes of clinical signs. Finally, the last stage is Alzheimer's dementia.

AD is a neurodegenerative disease characterized by a rapid decline in cognition: memory loss is the main feature of the disease. The episodic memory is related to personal events and experiences that are stored in the hippocampus[49], the first region to suffer damage in AD[50]. Therefore, the affected individual first forgets details about their own experiences. Semantic memory[49] loss occurs next: one forgets the general concepts of knowledge leading to language impairment[51] when the patient cannot recall the correct words. The inability to perform some tasks because of motor disorder as opposed to not understanding the tasks, also known as apraxia, is another sign of AD that can be present independently from memory loss[52]. Agnosia[51], or the inability to process sensory information, is present in AD under two types: the inability to perceive one's own condition and difficulties, and the failure to recognize familiar faces.

Behavioral changes, due to AD, consist in feeling angry, upset, worried, and/or depressed. Depression can precede AD, it is also a risk factor for dementia[53]. Anxiety[54] can be the result of confusion due to the disease itself. Some patients display aggressive behavior[55] or at least become easily agitated[56]. Delusions and hallucinations are also common symptoms in AD that affect the individual's behavior[57].

2.1.2 Risk factors

As stated earlier, age is the most important risk factor in AD. The cases in individuals younger than 65 years old remain rare. However, the prevalence of the disease reaches 2% to 4% of the general population afterwards and keeps climbing to around 15% at 80 years old[58]. It is important to note that other pathologies which are common among the elderly, have the same clinical presentation as AD. Recently, a new condition has been recognized in older subjects with dementia: limbic-predominant age-related TDP-43 encephalopathy (LATE). It has been associated with cognitive impairment that mimicked AD's clinical syndrome. LATE is suspected to be present in up to 50% of adults over 80 years old[59]. As a result, the role of advanced age is not specific to AD: it is the most important risk factor for neurodegenerative diseases.

Other risk factors are fewer years of education[60], obesity[61], cardiovascular diseases[61], diabetes[62], and loneliness[63].

The presence of the apolipoprotein E4 (APOE4) allele was significantly associated with increased risk of Alzheimer's disease[60] because the E4 isoform does not effectively enhance the breakdown of the amyloid protein[64] leaving the carrier of the APOE4 allele vulnerable to AD.

2.1.3 Diagnosis

An interview with the patient and their family permits the evaluation of the individual's cognition, behavior, and daily function[65]. Many neuropsychological tests[66]–[68] have been developed to score the patient's cognitive abilities. Other laboratory tests should be

performed to rule out other conditions or to screen for risk factors associated with AD. MR imaging also enables the exclusion of other diseases that could explain the patient's symptoms. In addition, it shows if the brain displays global atrophy[69] as seen in histopathological studies. The extraction of the cerebrospinal fluid to measure the concentration of β-amyloid and tau protein is used to determine the likelihood of an AD diagnosis. Finally, biomarkers derived from PET imaging can give an insight on the presence of amyloid plaques[15] or tau tangles[13] in the brain, and therefore strengthen the confidence that the dementia symptoms are indeed due to AD. However, only postmortem study of the brain can confirm the diagnosis[70].

2.1.4 Pathology

AD is a neurodegenerative disease characterized by the presence of two histopathological lesions: the plaques formed by a deposit of amyloid protein and the tangles composed of tau protein. These lesions develop slowly during the pre-clinical phase of AD. Their temporal-spatial progression is used to define stages of the disease, known as Braak stages[71]. Figure 7 shows the hypothesized evolution[72] of these lesions as the disease progresses as well as the evolution of neuronal integrity, reflecting the cognitive ability of the subject.

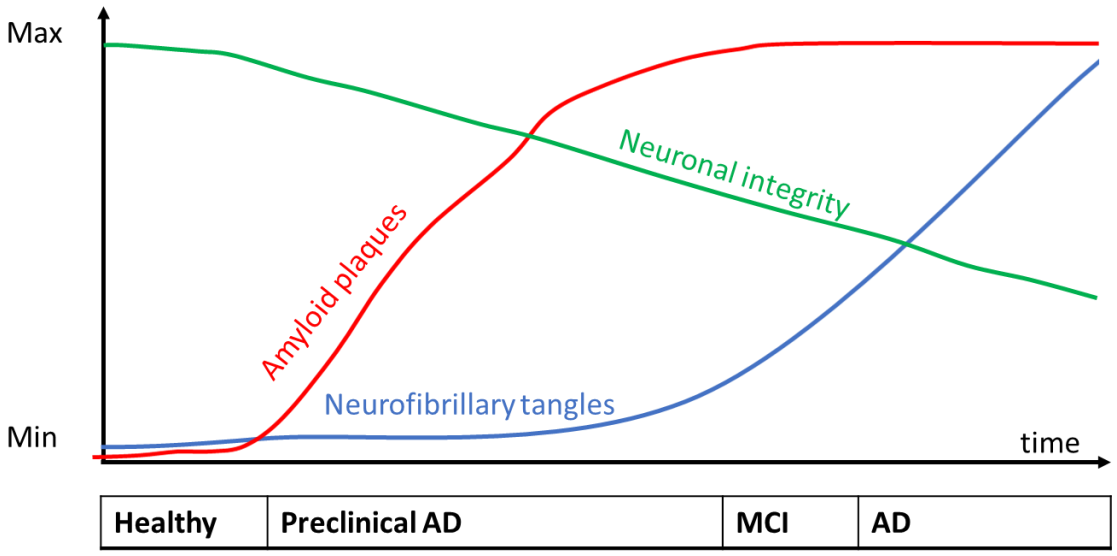

Figure 7: Hypothesized evolution of plaques and tangles in AD[72].

2.1.4.1 β-amyloid

β-amyloid is a fragment of the larger amyloid precursor protein (APP). The latter is present in the synapses of the neurons and it is believed to have a role in synaptic formation and repair. β-amyloids fold into soluble oligomers which aggregate in turn to eventually form amyloid plaques that are no longer soluble. This process is more likely if the concentration of β-amyloid is high, either because they are produced more often or because they are not eliminated fast enough. The oligomers are thought to be the most toxic to neurons whereas the plaques serve as reservoirs for these oligomers[73]. However, the mechanism leading to the brain cells death is not yet known.

Braak[71] defined three stages of β-amyloid accumulation in the brain:

- Stage A: small deposits in basal portions of the isocortex
- Stage B: deposits in association areas of the brain

- Stage C: large deposits throughout the association areas of the brain in addition to deposits in the primary areas.

The amyloid hypothesis[74] states that the accumulation of β-amyloid causes AD.

2.1.4.2 Tau

Neurofibrillary tangles appear inside of the neurons in histopathology studies of AD affected brains[75]. They are abnormal accumulation of tau protein. The latter is abundant in neurons as it stabilizes their microtubules. However, a higher concentration of defective tau[76] leads to the formation of paired helical filaments (PHF). They aggregate in neurofibrillary tangles disrupting the communication between neurons. PHF-tau block the distribution of nutrients to the brain cells resulting to their death[77].

Like amyloid, the spatial-temporal evolution of tau accumulation has been separated into 6 stages[71]: the tangles start in the transentorhinal region and progress to the hippocampus and the entorhinal cortex. They reach then the association areas of the brain and finally the entire isocortex.

The tau hypothesis states that PHF-tau protein accumulation in the brain causes AD[78].

2.2 PET imaging of tau protein

The appearance of excessive amounts of the PHF tau protein has been linked to the process of cognitive decline seen in dementia caused by Alzheimer's disease (AD)[79]. Until recently, the tangles could only be detected on postmortem evaluation of the brain. Therefore, it was not possible to monitor the progression of the tauopathy in living subjects. Thanks to the development of tau PET tracers, it is now possible to image the distribution

of the PHF tau in vivo. In this paragraph, we explain the importance of the evaluation of PHF tau in AD research and present the PET tracers developed for this goal.

2.2.1 Importance of tau PET imaging in AD research

The possibility to image β-amyloid using the [^{11}C]-PIB radiotracer paved the way to the design of clinical trials aiming to reduce the toxic plaques in the brain: longitudinal studies can be conducted to monitor the effect of an investigational drug against AD. The failure of most clinical trial involving anti-β-amyloid therapies lead the AD research community to question the validity of the amyloid hypothesis. Tau protein seems to play an important role in AD independent from the accumulation of β-amyloid.

Similarly, the design of clinical trials aiming to halt the accumulation of PHF tau or to break it down is possible if longitudinal studies of tau PET imaging are performed. The ability to accurately evaluate the distribution of tau protein in the brain and monitor its change is a pre-requisite for the successful conduct of such trials.

According to Braak[71] stages defined in Section 2.1.4.2, the accumulation of tau protein in regions such as the entorhinal cortex, the parahippocampal gyrus, the fusiform gyrus, the inferior temporal gyrus and the middle temporal gyrus precedes the development of AD clinical signs[80], [81]. Therefore, tracking the accumulation tau protein in those regions thanks to PET longitudinal studies enables the accurate diagnosis and the monitoring of prodromal AD. Tau PET imaging gives an opportunity to improve the accuracy of early diagnosis, an important step in the development of potential treatments against AD. There is indeed evidence that current treatments (although symptomatic) are more effective in the early stages of the disease[82].

In conclusion, the importance of tau PET imaging lies in two aspects: the possibility to conduct longitudinal studies in living subjects to monitor the effect of potential treatments, and the ability to diagnose AD early and therefore to start potential treatments before the disease advances and clinical signs manifest.

2.2.2 Tau protein PET tracers

A good candidate radiotracer for PET imaging of tau protein needs to satisfy the following requirements[83]:

- High selectivity for tau over β-amyloid and high binding affinity since tau tangles coexist with amyloid plaques in lower concentrations.
- Ability to cross the blood-brain barrier
- Possibility to be labelled with isotopes with long half-lives
- Low binding in the areas of the brain that do not contain tau protein

Many radiotracers have been developed for tau PET imaging. A few are listed in Table 2.

Radiotracer	Comments
[^{18}F]- FDDNP	Binds to both β-amyloid and tau tangles[84]
[^{18}F]- THK523	Selectively binds to PHF tau but exhibits high uptake in the white matter[85]
[^{18}F]- THK5105	Higher binding affinity to PHF tau than [^{18}F]- THK523[86]
[^{18}F]- THK5117	Higher binding affinity to PHF tau than [^{18}F]- THK523[86]
[^{18}F]- THK5351	Selectively binds to PHF tau and exhibits low uptake in the to the white matter[87]
[^{18}F]- T807	Higher selectivity for PHF-tau over β-amyloid[88]

Table 2: Radiotracers for tau PET imaging

The radiotracer [^{18}F]- T807, also known as [^{18}F]-AV-1451, has high binding affinity and high selectivity for PHF-tau over β-amyloid as shown in histopathological studies[88], [89]. Human PET imaging studies[90] showed an uptake in the cortical regions where PHF-tau accumulation is expected in the brains of patients with AD. In addition, the uptake was correlated to the severity of the tauopathy.

The modeling of the kinetics of the radiotracer identified the 80- to 100-minute time window[91] to calculate the Standard Uptake Value Ratio (SUVR), the cerebellum cortex being the reference region[92]. The SUVR is a region-dependent metric defined as:

$$\mathrm{SUVR}_{\mathrm{image}}(\mathrm{target}) = \frac{\mathrm{mean}\big(\mathrm{SUV}(\mathrm{target})\big)}{\mathrm{mean}\big(\mathrm{SUV}(\mathrm{reference})\big)} \quad (13)$$

The radiotracer [^{18}F]-AV-1451 is a promising PHF tau PET tracer. As a result, it is being used in longitudinal studies[79] to monitor the progression of tau accumulation in controls and patients with mild cognitive impairment or AD. **This work relies on the acquired data from these studies as we propose a joint reconstruction framework to image changes in PHF tau accumulation from the longitudinal PET scans.**

CHAPTER 3. Problem statement

AD leads to a drastic reduction in the quality of life of those affected. It also negatively impacts the society since the burden for caring of AD subjects falls on families who are now facing unsuspected challenges explained by the ballooning costs of AD care. Currently, approved treatments are few and of limited efficacy, typically serving to only temporarily slow the progression of the disease. Drug development for AD has so far been slow due, in part, to the inability to detect minor changes in AD biomarkers, therefore, it is imperative for the faster development of preventive treatments to detect the onset of AD as early as possible and observe its progression as frequently as possible.

The excessive accumulation of PHF tau protein has been linked to the process of cognitive decline seen in dementia caused by AD. Accurate estimation of changes in Tau protein deposition in the brain of subjects affected by AD in the very early stages can drastically improve accuracy of diagnosis and aid the faster development of effective treatments that halt its advancement. The tracer [^{18}F]-AV-1451 used in PET imaging enables the observation of the distribution of PHF tau in vivo. As a result, detection of changes in tau accumulation is possible through longitudinal PET studies. [^{18}F]-AV-1451 uptake also displayed strong association with the severity of the tauopathy: since tau protein accumulation in the entorhinal-hippocampal region begins before the clinical signs of the disease appear, an image of the distribution of tau in the brain helps in the diagnosis of early AD.

The rate of tau accumulation in the brain is more important than the distribution of tau itself for AD because some accumulation of tau is expected in normal aging. Only excessive amounts lead to the cognitive decline seen in AD. To determine the rate of tau deposition in prodromal AD, the conventional approach consists in scanning the subject at least twice separated by 2 to 3 years and reconstructing the images of each scan separately. An annual rate of tau accumulation in every region of interest is derived for each subject from the resulting difference image. This approach has low sensitivity to slight changes in tau deposition due to increased variation in the difference image. The high variance increases the sample size needed for hypothesis testing looking at the difference of the accumulation of the tau in two groups of subjects. Indeed, small increments of tau are masked by the high variation in the image. As a result, this approach also requires longer inter-scan times making any clinical trial for drug development expensive and slow.

We propose a joint longitudinal image reconstruction approach where the tau deposition difference image is reconstructed directly from measurements, drastically lowering the intensity variation in the difference image. The proposed approach increases sensitivity to slight changed in tau thereby reducing the sample size required to conduct a comparative population study, allowing shorter inter-scan times or smaller sample sizes required for hypothesis testing on progression of AD-related tauopathy.

PART II METHODS

CHAPTER 4. Joint Reconstruction

We propose the development of a joint image reconstruction method for longitudinal PET imaging of tau protein in the brain to increase sensitivity to subtle changes in tau accumulation between scans. The accurate estimation of tau changes paves the way to early diagnosis of AD and could also constitute a reliable metric to judge the efficacy of a drug candidate in clinical trial.

4.1 Advantages of the joint reconstruction

The conventional approach consists in reconstructing the images, noted $\boldsymbol{f_1}$ and $\boldsymbol{f_2}$, separately. The change of tau accumulation in a target region is noted ΔSUVR and is:

$$\Delta\mathrm{SUVR}_{\mathrm{conventional}}(\mathrm{target}) = \frac{\mathrm{SUVR}_{\mathbf{f_2}}(\mathrm{target}) - \mathrm{SUVR}_{\mathbf{f_1}}(\mathrm{target})}{\mathrm{SUVR}_{\mathbf{f_1}}(\mathrm{target})} \times 100 \quad (14)$$

Unlike the conventional approach, the joint reconstruction framework yields directly a difference image reconstructed from the concatenation of the measurements acquired in both scans. We hypothesize that the variance in the joint difference image will be lower compared to the conventional difference image as the latter is the result of a subtraction between two images reconstructed separately and thus exhibits a high variance.

Longitudinal studies can benefit greatly from the joint reconstruction. Taking advantage of the high degree of similarity between the acquisitions through the implementation of a constraint on the difference image reconstructed simultaneously leads to lower noise levels[93]. The constraint of the sparsity of the difference image is incorporated using the

one-step-late iterative reconstruction method[94]. Other priors on the difference image can be implemented instead:

- the entropy prior penalizes large variation of signal in tissue classes[95]
- the total variation prior ensures that the difference image's spatial gradient is sparse[96]

These priors have been implemented in longitudinal PET studies for tumor detection and tumor progression[97]. The obtained difference images exhibit lower noise levels, but a bias was introduced in the tumor.

Other joint reconstruction methods have been proposed in SPECT for two different applications: reconstruction of rest/stress myocardial perfusion scans[98], and reconstruction of ictal/inter-ictal data[99]. In this framework, the difference image is directly reconstructed from the two scans without the use of any prior. It also achieves better results in terms of detecting cardiac defect or epileptic foci localization. In the next section, we develop the same joint reconstruction framework for longitudinal PET studies.

4.2 The joint reconstruction algorithm

We want to infer the change in tau buildup from two measurements taken two to three years apart. Registration is required to account for the misalignment between the two time-points. Different injected doses during the two scans are also incorporated into the model thanks to the use of scaling factors.

4.2.1 The forward model for the joint reconstruction

We note the measured projections data $\boldsymbol{n_1}$ and $\boldsymbol{n_2}$ from the scans performed at the time-points t_1 and t_2. $\boldsymbol{p_1} = \overline{\boldsymbol{n_1}}$ and $\boldsymbol{p_2} == \overline{\boldsymbol{n_2}}$ denote the expected value of the measured projections for t_1 and t_2, respectively. We have already noted $\boldsymbol{f_1}$ and $\boldsymbol{f_2}$ the images corresponding to each time-point. The system matrix for each scan is noted $\boldsymbol{H}$ and can be decomposed into three components as seen in Section 1.3.2: $\boldsymbol{H} = \boldsymbol{SAG}$. The acquisitions are performed with the same imaging parameters on the same scanner, so the forward model for both acquisitions can be written as follows:

$$\begin{cases} \boldsymbol{p_1} = \boldsymbol{S_1 A_1 G f_1} \\ \boldsymbol{p_2} = \boldsymbol{S_2 A_2 G f_2} \end{cases} \quad (15)$$

Tau PET images are used to derive a region-wise SUVR using the cerebellum cortex as reference region. The change in SUVR between the two scans reflects the change in tau accumulation regardless of the differences in the injected doses. As a result, we defined two scaling factors α_1 and α_2 as the mean SUV in the reference region in $\boldsymbol{f_1}$ and $\boldsymbol{f_2}$. Additionally, we obtain a transformation matrix that registers the second image to the first one, noted $\boldsymbol{R}$. Using these notations, we can finally define the difference image as follows:

$$\boldsymbol{\tau} = \boldsymbol{R}\frac{\boldsymbol{f_2}}{\alpha_2} - \frac{\boldsymbol{f_1}}{\alpha_1} \quad (16)$$

Note that the obtained difference image maps the change in SUVR between the scans. To get the yearly rate of tau buildup in a region of interest, the ΔSUVR in the region is divided by the time difference $t_2 - t_1$. The assumption of a linear model is justified by the few

time-points we currently have. A more complex model could be studied on longer longitudinal studies with more tau PET scans.

We can then write the forward model for the joint reconstruction framework as:

$$\begin{bmatrix} \boldsymbol{p_1} \\ \boldsymbol{p_2} \end{bmatrix} = \begin{bmatrix} \boldsymbol{S_1 A_1 G} & 0 \\ \frac{\alpha_2}{\alpha_1} \boldsymbol{S_2 A_2 G R^T} & \alpha_2 \boldsymbol{S_2 A_2 G R^T} \end{bmatrix} \begin{bmatrix} \boldsymbol{f_1} \\ \boldsymbol{\tau} \end{bmatrix} \quad (17)$$

$\boldsymbol{R^T}$ denotes the inverse transformation which registers the first image to the second one.

We note $\boldsymbol{f_{com}}$ the common image given by the joint reconstruction to distinguish it from the $\boldsymbol{f_1}$ the first image reconstructed separately. Naturally, we have $\boldsymbol{f_{com} = f_1}$.

4.2.2 EM for the joint reconstruction

The general forward reconstruction problem is usually written in a matrix format as follows: $\bar{\boldsymbol{U}} = \boldsymbol{QV}$. The update formula for the EM algorithm then given by:

$$\boldsymbol{V^{(k+1)}} = \frac{\boldsymbol{V^{(k)}}}{\boldsymbol{Q^T 1}} \boldsymbol{Q^T} \frac{\boldsymbol{U}}{\boldsymbol{QV^{(k)}}} \quad (18)$$

Using the equations: $V = \begin{bmatrix} \boldsymbol{f_{com}} \\ \boldsymbol{\tau} \end{bmatrix}$, $\bar{\boldsymbol{U}} = \begin{bmatrix} \boldsymbol{p_1} \\ \boldsymbol{p_2} \end{bmatrix}$, and $\boldsymbol{Q} = \begin{bmatrix} \boldsymbol{S_1 A_1 G} & 0 \\ \frac{\alpha_2}{\alpha_1} \boldsymbol{S_2 A_2 G R^T} & \alpha_2 \boldsymbol{S_2 A_2 G R^T} \end{bmatrix}$, we finally get the following update formulas for the EM algorithm (including the scatter, noted $\overline{\boldsymbol{d_1}}$ and $\overline{\boldsymbol{d_2}}$, and the randoms, noted $\overline{\boldsymbol{r_1}}$ and $\overline{\boldsymbol{r_2}}$, corrections) [98], [99]:

$$\widehat{\boldsymbol{f_{com}}}^{(k+1)} = \frac{\widehat{\boldsymbol{f_{com}}}^{(k)}}{\boldsymbol{G^T A_1^T S_1^T \mathbb{1}} + \frac{\alpha_2}{\alpha_1}\boldsymbol{R G^T A_2^T S_2^T \mathbb{1}}} \left(\boldsymbol{G^T A_1^T S_1^T} \frac{\boldsymbol{n_1}}{\boldsymbol{S_1 A_1 G}\widehat{\boldsymbol{f_{com}}}^{(k)} + \overline{\boldsymbol{d_1}} + \overline{\boldsymbol{r_1}}} \right.$$

$$\left. + \frac{\alpha_2}{\alpha_1}\boldsymbol{R G^T A_2^T S_2^T} \frac{\boldsymbol{n_2}}{\alpha_2 \boldsymbol{S_2 A_2 G R^T}\left(\frac{\widehat{\boldsymbol{f_{com}}}^{(k)}}{\alpha_1} + \hat{\boldsymbol{\tau}}^{(k)}\right) + \overline{\boldsymbol{d_2}} + \overline{\boldsymbol{r_2}}} \right) \quad (19)$$

$$\hat{\boldsymbol{\tau}}^{(k+1)} = \frac{\hat{\boldsymbol{\tau}}^{(k)}}{\alpha_2 \boldsymbol{R G^T A_2^T S_2^T \mathbb{1}}}\, \alpha_2 \boldsymbol{R G^T A_2^T S_2^T} \frac{\boldsymbol{n_2}}{\alpha_2 \boldsymbol{S_2 A_2 G R^T}\left(\frac{\widehat{\boldsymbol{f_{com}}}^{(k)}}{\alpha_1} + \hat{\boldsymbol{\tau}}^{(k)}\right) + \overline{\boldsymbol{d_2}} + \overline{\boldsymbol{r_2}}} \quad (20)$$

Both the first image and the difference image are updated at each iteration k of the EM algorithm. Similarly, within each iteration, the update formulas are applied numerous times using different subsets of the projections data as explained in Section 1.3.1 for the OSEM algorithm.

For the joint reconstruction model, prior knowledge of the registration matrix and the scaling factors is needed. These parameters are determined from the prior separate reconstruction of the images $\boldsymbol{f_1}$ and $\boldsymbol{f_2}$.

From Equation (20), given an initial image $\widehat{\boldsymbol{\tau}^{(1)}}$ that is positive, the final estimated image cannot be negative. This positivity constraint is always present in any OSEM reconstruction and it is desirable since the distribution of the radiotracer (*i.e.* the reconstructed image) is never negative. In our case, the constraint is also justifiable: we want to estimate the change of PHF tau deposition from longitudinal PET studies in

different populations; the amount of tau is known to progress with age even in healthy subjects[100].

4.2.3 Cramer-Rao Bound

In this paragraph, we derive the Cramer-Rao bound for the joint reconstruction estimator of the difference image. The Cramer-Rao bound[101] gives the lowest possible variance for an unbiased estimator of a parameter. In the multivariate case, it is given by the following equation where $T(\boldsymbol{\theta})$ is an unbiased estimator of the unknown parameter θ, and $\boldsymbol{J}$ is the Fisher information matrix:

$$cov(T(\boldsymbol{\theta}) \geq \boldsymbol{J}^{-1} \quad (21)$$

Using the notations from Equation (1) and the model written Equation (17), we get the likelihood function for the joint reconstruction model:

$$L(\boldsymbol{\tau}, \mathbf{f_{com}} | \boldsymbol{n_1}, \boldsymbol{n_2}) = \prod_{j=1}^{K} \frac{exp(-p_{1,j})\, p_{1,j}^{n_{1,j}}}{n_{1,j}!} \times \prod_{j=1}^{K} \frac{exp(-p_{2,j})\, p_{2,j}^{n_{2,j}}}{n_{2,j}!} \quad (22)$$

For simplification, we assume that the images are co-registered and that $\boldsymbol{A_1} = \boldsymbol{A_2}$ and $\boldsymbol{S_1} = \boldsymbol{S_2}$. $\boldsymbol{H}$ is then the system matrix for both acquisitions and Equation (17) becomes:

$$\begin{bmatrix} \boldsymbol{p_1} \\ \boldsymbol{p_2} \end{bmatrix} = \begin{bmatrix} \boldsymbol{H} & 0 \\ \frac{\alpha_2}{\alpha_1}\boldsymbol{H} & \alpha_2 \boldsymbol{H} \end{bmatrix} \begin{bmatrix} \boldsymbol{f_{com}} \\ \boldsymbol{\tau} \end{bmatrix} \quad (23)$$

Let's note $\boldsymbol{x} = [\boldsymbol{f_{com}} \quad \boldsymbol{\tau}]^T$ and $\boldsymbol{y} = [\boldsymbol{n_1} \quad \boldsymbol{n_2}]^T$. The Fisher information matrix is:

$$\boldsymbol{J} = \mathbb{E}\left[-\frac{\partial^2 \ln\big(L(\boldsymbol{x}|\boldsymbol{y})\big)}{\partial \boldsymbol{x} \partial \boldsymbol{x}} | \boldsymbol{x} \right] = \begin{bmatrix} \boldsymbol{J}^{(\boldsymbol{f_{com}} \boldsymbol{f_{com}})} & \boldsymbol{J}^{(\boldsymbol{\tau} \boldsymbol{f_{com}})} \\ \boldsymbol{J}^{(\boldsymbol{f_{com}} \boldsymbol{\tau})} & \boldsymbol{J}^{(\boldsymbol{\tau}\boldsymbol{\tau})} \end{bmatrix} \quad (24)$$

The element $j_{q,r}^{(\boldsymbol{f_{com}f_{com}})}$ of the matrix $\boldsymbol{J}^{(\boldsymbol{f_{com}f_{com}})}$ is given by:

$$j_{q,r}^{(\boldsymbol{f_{com}f_{com}})} = \mathbb{E}\left[-\frac{\partial^2 \ln\big(L(\boldsymbol{x}|\boldsymbol{y})\big)}{\partial f_{com,q}\partial f_{com,r}}|\boldsymbol{x}\right]$$

$$= \mathbb{E}\left[\sum_{j=1}^{K}\frac{n_{1,j}h_{j,q}h_{j,r}}{\left(\sum_{i=1}^{M}h_{j,i}f_{com,i}\right)^2}|\boldsymbol{x}\right] + \left(\frac{\alpha_2}{\alpha_1}\right)^2 \mathbb{E}\left[\sum_{j=1}^{K}\frac{n_{2,j}h_{j,q}h_{j,r}}{\left(\sum_{i=1}^{M}h_{j,i}\left(\frac{\alpha_2}{\alpha_1}f_{com,i}+\alpha_2\tau_i\right)\right)^2}|\boldsymbol{x}\right]$$

$$= \sum_{j=1}^{K}\frac{h_{j,q}h_{j,r}}{\sum_{i=1}^{M}h_{j,i}f_{com,i}} + \left(\frac{\alpha_2}{\alpha_1}\right)^2\sum_{j=1}^{K}\frac{h_{j,q}h_{j,r}}{\sum_{i=1}^{M}h_{j,i}\left(\frac{\alpha_2}{\alpha_1}f_{com,i}+\alpha_2\tau_i\right)}$$

$$= \sum_{j=1}^{K}\frac{h_{j,q}h_{j,r}}{p_{1,j}} + \left(\frac{\alpha_2}{\alpha_1}\right)^2\sum_{j=1}^{K}\frac{h_{j,q}h_{j,r}}{p_{2,j}} \quad (25)$$

Let's note $\boldsymbol{F_1} = \boldsymbol{H^T}diag\{\frac{1}{\boldsymbol{p_1}}\}\boldsymbol{H}$ and $\boldsymbol{F_2} = \boldsymbol{H^T}diag\{\frac{1}{\boldsymbol{p_2}}\}\boldsymbol{H}$. Then:

$$\boldsymbol{J}^{(\boldsymbol{f_{com}f_{com}})} = \boldsymbol{F_1} + \left(\frac{\alpha_2}{\alpha_1}\right)^2\boldsymbol{F_2} \quad (26)$$

Similarly, we obtain: $\boldsymbol{J}^{(\boldsymbol{\tau f_{com}})} = \frac{\alpha_2^2}{\alpha_1}\boldsymbol{F_2}, \boldsymbol{J}^{(\boldsymbol{f_{com}\tau})} = \frac{\alpha_2^2}{\alpha_1}\boldsymbol{F_2}, \boldsymbol{J}^{(\boldsymbol{\tau\tau})} = \alpha_2^2\,\boldsymbol{F_2}$.

Therefore, the Fisher information matrix is:

$$\boldsymbol{J} = \begin{bmatrix} \boldsymbol{F_1} + \left(\frac{\alpha_2}{\alpha_1}\right)^2\boldsymbol{F_2} & \frac{\alpha_2^2}{\alpha_1}\boldsymbol{F_2} \\ \frac{\alpha_2^2}{\alpha_1}\boldsymbol{F_2} & \alpha_2^2\,\boldsymbol{F_2} \end{bmatrix} \quad (27)$$

The lower bound of the covariance for the estimator $\hat{\boldsymbol{x}} = [\widehat{\boldsymbol{f_{com}}} \quad \hat{\boldsymbol{\tau}}]^{\boldsymbol{T}}$ based on the joint reconstruction is given by the Cramer-Rao bound:

$$COV(\hat{\boldsymbol{x}}) \geq \boldsymbol{J^{-1}} = \begin{bmatrix} \boldsymbol{A} & \boldsymbol{B} \\ \boldsymbol{C} & \boldsymbol{D} \end{bmatrix} \quad (28)$$

The matrix **D** contains the lower bound of the covariance in the difference image $\boldsymbol{\tau}$ and it is written as[102], [103]:

$$COV(\hat{\boldsymbol{\tau}}) = \frac{1}{\alpha_1^2}\boldsymbol{F_1^{-1}} + \frac{1}{\alpha_2^2}\boldsymbol{F_2^{-1}} \quad (29)$$

We can also determine the Cramer-Rao bound for the estimator of the conventional method. Assuming the same system matrix for both acquisition, and in the absence of motion between the scans, the difference image is given directly by: $\boldsymbol{\tau} = \frac{\boldsymbol{f_2}}{\alpha_2} - \frac{\boldsymbol{f_1}}{\alpha_1}$ where $\boldsymbol{p_1} = \boldsymbol{Hf_1}$ and $\boldsymbol{p_2} = \boldsymbol{Hf_2}$. The covariance of the difference image equals to:

$$COV(\hat{\boldsymbol{\tau}}) = \frac{1}{\alpha_2^2}\, COV\left(\widehat{\boldsymbol{f_2}}\right) + \frac{1}{\alpha_1^2}\, COV\left(\widehat{\boldsymbol{f_1}}\right) \quad (30)$$

The covariances of the estimators for the images at both time-points are higher than the Cramer-Rao bounds given by the inverse of the Fisher information matrices $\boldsymbol{J_1}$ and $\boldsymbol{J_2}$. The same derivation applied earlier leads to the following equalities: $\boldsymbol{J_1} = \boldsymbol{F_1}$ and $\boldsymbol{J_2} = \boldsymbol{F_2}$. Finally, we have:

$$COV(\hat{\boldsymbol{\tau}}) \geq \frac{1}{\alpha_1^2}\boldsymbol{F_1^{-1}} + \frac{1}{\alpha_2^2}\boldsymbol{F_2^{-1}} \quad (31)$$

Both methods have the same lower bound for variance of the difference image. We know that OSEM algorithm deviates from the Cramer-Rao bound[104] although the Maximum Likelihood estimator reaches it asymptotically. Since the two methods are OSEM-based, the main difference between them is the positivity constraint introduced in the joint

reconstruction framework as explained in Section 4.2.1. It should act as a regularizer for the difference image and therefore reduce the variance.

4.3 Implementation

In addition to the tau PET scans, T1-weighted MR images are acquired and then processed in FreeSurfer[105] to yield subject-specific segmentation labels identifying the regions of interest in the brain. In our study, we focus on the regions involved in AD-related tauopathy such as the entorhinal cortex (EC), the para hippocampal gyrus (PHG), the fusiform gyrus (FG), the inferior temporal gyrus (ITG), and the hippocampus (HC). An additional region is important in our case: the cerebellum cortex as it serves as a reference region for computing the region-wise SUVR. Obviously, accurate registration between the MR and PET is needed to identify brain regions on PET images.

4.3.1 Registration

Like iterative image reconstruction, image registration[106] is an optimization problem wherein a cost function is minimized to match a desired input, commonly called the fixed image. The optimization concerns the parameters of a spatial transformation that successfully maps the moving image, noted $\boldsymbol{m}$, to the fixed one, noted $\boldsymbol{f}$. Our study only involves intra-subject head registration, which can be solved using rigid transformations[107]. Rigid transformations include rotation and translation and preserve the shape and the size of the registered object. In 3D, a rigid transformation can be described by 6 parameters (3 translations and 3 rotations) which are estimated iteratively during optimization. If $\boldsymbol{q}$ denotes the parameters, then the rigid transformation can be written as $\boldsymbol{R}(\boldsymbol{q})$.

For images of the same modality, the cost function aiming to minimize the voxel-wise squared differences between the images is usually enough to get an accurate transformation. Let x_i be the voxels in the fixed image. The cost function in this case is given by:

$$\hat{\boldsymbol{q}} = \arg\min_{\boldsymbol{q}} \left(\sum_i \left(\boldsymbol{m}(\boldsymbol{R}(\boldsymbol{q})x_i) - \boldsymbol{f}(x_i) \right)^2 \right) \quad (32)$$

The design of the cost function enables the registration of images with different modalities by incorporating the mutual information transformation[108] to match the signal intensities in both images. The mutual information of the moving image m and the fixed image f is[109]:

$$I(\boldsymbol{m}, \boldsymbol{f}) = \sum_k \sum_l p(m_k, f_l) \log \left(\frac{p(m_k, f_l)}{p(m_k)p(f_l)} \right) \quad (33)$$

The indexes k and l loop through the gray values (the intensity of the voxels) of the moving and the fixed images, respectively. $p(m_k)$ and $p(f_l)$ gives the probabilities of the gray values m_k and f_l in their corresponding images whereas $p(m_k, f_l)$ gives the joint probability of the gray values which can be estimated from the joint histogram of the images $\boldsymbol{m}$ and $\boldsymbol{f}$. Let $\boldsymbol{m}'(\boldsymbol{q})$ be the image obtained after applying the transformation $\boldsymbol{R}(\boldsymbol{q})$ to the moving image $\boldsymbol{m}$. The cost function aims at maximizing the mutual information between the current image $\boldsymbol{m}'(\boldsymbol{q})$ and the fixed image $\boldsymbol{f}$:

$$\hat{\boldsymbol{q}} = \arg\max_{\boldsymbol{q}} \left(I(\boldsymbol{m}'(\boldsymbol{q}), \boldsymbol{f}) \right) \quad (34)$$

In the joint reconstruction, both cross- and intra- modality registrations are required: the identification of the regions of interest on the PET images involves mapping the MR image to the PET space; the longitudinal studies require the registration between the PET images acquired at t_1 and t_2. The implementation of the registration was performed on Matlab[110] using the toolbox developed by Kroon[111].

4.3.2 ECAT EXACT HR +

The PET images are acquired on the Siemens/CTI ECAT EXACT HR +[112] using OSEM reconstruction with 4 iterations and 16 subsets. In this section, we focus on the details of the reconstruction for this scanner.

4.3.2.1 Acquisition parameters

The scanner operates in 3D acquisition mode with an angular mashing factor of 2 and a span of 9. Table 3 shows the parameters of the scanner under these conditions.

Number of rings	32
Detectors per ring	576
Number of views	144
Number of LORs per view	288
Number of sinograms	239
Image size	128×128×63
Voxel size (mm^3)	2.25×2.25×2.43

Table 3: ECAT HR+ parameters in 3D mashing mode

4.3.2.2 Sensitivity coefficients

The normalization factors file provided by the scanner for each acquisition contain information regarding:

- the geometric efficiency of the pair of detectors (k,l) forming the LOR j: f_j

- the crystal efficiency of the LOR: $\epsilon_j = \epsilon_k \epsilon_l$
- the crystal interference effect of the LOR: i_j
- the dead-time efficiency: d_j

The sensitivity coefficient for the LOR j is then given by[113]: $S_{j,j} = f_j \epsilon_j i_j d_j$.

4.3.2.3 Attenuation coefficients

An attenuation image is reconstructed from the blank and the transmission scan. The forward projection on the image yields an attenuation coefficient for each LOR.

4.3.2.4 Forward and back projection

As seen in Section 1.3.2, the system matrix incorporates the geometry of the scanner and performs the mapping between the image and projection spaces: forward projection consists in generating count data from an image while back projection yields an image from the counts. In our study, the forward and back projections for ECAT HR+ are implemented through the Software for Tomographic Image Reconstruction (STIR)[114].

4.3.2.5 Scatter correction

The number of counts due to scatter is estimated through the Single Scatter Simulation followed by the application of a scaling factor to account for all scattering events as seen in Section 1.2.2. The scatter estimation was also performed using STIR[115].

4.3.2.6 Randoms correction

The measured counts by the ECAT HR+ are already random-corrected: the coincidences detected in the delayed window, described in Section 1.2.1, are directly subtracted from the counted events during the acquisition. The mean random coincidences are then estimated from the total counts detected in the delayed window[116].

With the subtracted random coincidences, the measured counts no longer follow Poisson statistics. The shifted Poisson model[117] has been proposed as an approximation of the true log-likelihood of the pre-corrected data.

The EM algorithm for single image reconstruction using the shifted Poisson model is[116]:

$$\lambda_l^{(k+1)} = \frac{\lambda_l^{(k)}}{\sum_{j=1}^{K} a_j s_j g_{j,l}} \sum_{j=1}^{K} \frac{a_j s_j g_{j,l} (n_j + 2\overline{r_j})}{\sum_{q=1}^{M} a_j s_j g_{j,q} \lambda_q^{(k)} + \overline{d_j} + \overline{2r_j}} \quad (35)$$

A similar modification is added to the update formula for the joint reconstruction.

In the next two chapters, we apply the joint reconstruction framework to simulation studies and patient data.

CHAPTER 5. Numerical simulations

The joint reconstruction method requires an accurate registration and the definition of two scaling factors to compare two PET acquisitions performed two to three years apart. Numerical simulations are simplified problems for which the unknown parameters can be controlled enabling a robust evaluation of the method. In this chapter, we simulate a higher tau uptake in a subject's image and estimate the resulting difference image, making registration and scaling irrelevant.

We simulate an increased accumulation of tau in one subject's scan. We used the reconstructed PET image at t_1 as the background image. The baseline MR image is then registered to the background image; the resulting transformation is applied to the segmentation labels drawn on FreeSurfer. We can now identify the ROIs exhibiting higher tau uptake in AD directly on the PET image. Table 4 shows the size of the ROIs after they were mapped to the PET image. We chose to simulate the increase in the inferior temporal gyrus because its larger size lessens the impact of registration errors in our study: we get an image wherein every voxel in the ITG was set to the mean value of SUV in the ITG on the background image. The obtained image is forward projected to give a sinogram to which Poisson noise is added.

Region	**Size on PET image**
Entorhinal Cortex	348 voxels
Fusiform Gyrus	2076 voxels
Hippocampus	731 voxels
Inferior Temporal Gyrus	2384 voxels
Parahippocampal Gyrus	418 voxels

Table 4: The size of the considered ROIs on the PET image

The PET data for the simulated second time-point should be obtained by the sum of the sinogram from the t_1 and the simulated sinogram. However, since the tau accumulation was initially simulated as a 100% increase in the SUV value, additional processing is needed to make sure we control the value of the resulting ΔSUVR.

To find the appropriate scaling factor, we reconstruct the image obtained from the sum of the sinograms. The SUVR in the ITG in that image is noted $\mathrm{SUVR}_{\mathrm{simulated}_{100\%}}(\mathrm{ITG})$ as it reflects a 100% increase in the SUV value. The difference between the resulting image and the background image yields a $\Delta\mathrm{SUVR}^{(100\%)}$ expressed as a percentage increase of the SUVR in the background image:

$$\Delta\mathrm{SUVR}^{(100\%)} = \frac{\mathrm{SUVR}_{\mathrm{simulated}_{100\%}}(\mathrm{ITG}) - \mathrm{SUVR}_{\mathrm{background}}(\mathrm{ITG})}{\mathrm{SUVR}_{\mathrm{bakcground}}(\mathrm{ITG})} \times 100 \quad (36)$$

A scaled image is then produced: the voxels in the ITG are set to the mean value of the SUV in the ITG in the background image multiplied by a scaling factor $\frac{c}{\Delta\mathrm{SUVR}^{(100\%)}}$ where c reflects the desired increase of tau accumulation, also expressed as a percentage of the initial SUVR. The new scaled image is forward projected and Poisson noise is added to the resulting sinogram. The obtained data is then used as the simulated sinogram of t_2. The steps described above are summarized in Figure 8.

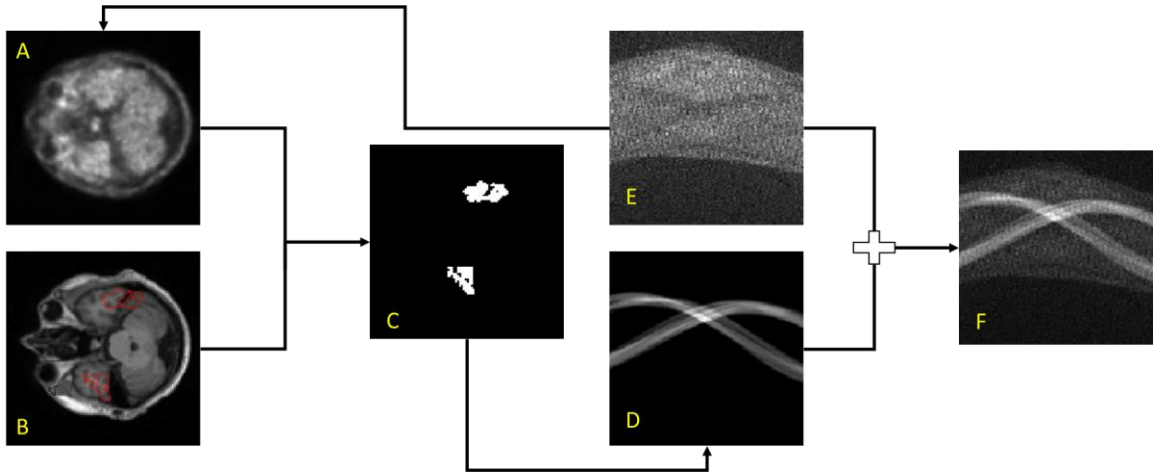

Figure 8: Generation of a simulated PET data with an increased tau accumulation. (A) shows the background image: the PET image at t_1. (B) represents the MR image and the segmentation label localizing the ITG after registration to the PET image. (C) is the obtained image after multiplying the mean value of SUV in ITG by a scaling factor. The image (C) is forward projected and a Poisson noise is added to get the sinogram (D). (E) is the initial PET data used to reconstruct the PET image. The summation of (E) and (D) yields the PET data for the simulated time-point t_2.

The initial and the simulated PET data can now be viewed as two separate acquisitions where the increase in tau uptake is known. The registration transformation between the time-points is the identity and the scaling factors are equal, leading to simplified equations for the joint reconstruction. We reconstruct the difference image using the conventional and the proposed methods at increasing levels of tau accumulation: 3, 5, 7 and 10%.

CHAPTER 6. Patient Data

The Harvard Aging Brain Study[118] (HABS) currently underway at Massachusetts General Hospital (MGH) provides an excellent testbed for the evaluation of the proposed joint reconstruction: it is a longitudinal observational study with the goal to distinguish between normal aging and pre-clinical AD. Additional studies[79] involving subjects at various degrees of tauopathy (MCI, AD) contribute to our testing dataset. For every subject, we reconstruct the difference image using the conventional method and the joint reconstruction framework. We study the resulting ΔSUVRs across the different groups.

6.1 Studies protocols

The goal of HABS is to follow the aging of a large cohort of subjects as some of them, inevitably, develop the symptoms of AD. The inclusion criteria are:

- Age: between 50 and 90
- Clinical Dementia Rating[67] (CDR): 0
- Mini Mental State Exam[68] (MMSE): between 27 and 30
- A study partner who can answer questions pertaining to daily functioning
- Absent or well-controlled vascular risk factor

Subjects who have an initial diagnosis of MCI or dementia are excluded. Subjects who progress to MCI and/or late stage of AD or develop other neurological processes that may influence cognitive decline can remain in the study.

Subjects who express interest in participating in the study undergo a Telephone Interview for Cognitive Status [119](TICS) to determine eligibility. If the subject passes the initial screening, he/she is invited to complete the 17 visits of the study summarized in Table 5.

Visit Number	1 to 7							8	9	10 to 15						16	17
Time (Months)	0 to 6							12	24	36						48	60
Consent	X																
Blood Draw		X						X	X	X						X	X
Neurological and physical exam	X									X							
Medical and family history	X									X							
Cognitive Screening (CDR)	X							X	X	X						X	X
Neuropsychological Exam		X						X	X	X						X	X
Pedometer 7-Day Evaluation		X															
Functional and **Structural MRI**			X	X							X	X					
Amyloid PET scan					X								X				
Tau PET scan						X								X			
Optional Lumbar Puncture							X								X		

Table 5: HABS visits

The tau PET scan visits are two to three years apart. For each visit, the subject receives an intravenous injection of the radiotracer [^{18}F]-AV-1451. After a period of 75 minutes, the PET scan starts and lasts 30 minutes. The baseline MR imaging is another important visit to our work: a 3T MRI scan using a standard Magnetization-Prepared RApid Gradient-Echo (MPRAGE) sequence[120], optimized for FreeSurfer[121], is acquired to generate high-resolution anatomical regions of interest for volumetric analyses.

Since subjects with a diagnosis of MCI or AD are excluded from HABS, we recruit additional subjects from the Memory Disorders Clinics at MGH or Brigham and Women's Hospital (BWH) and from the Massachusetts Alzheimer's Disease Research Center.

Cognitive evaluation is performed on all subjects including CDR and MMSE. Each subject undergoes at least two tau PET scan, two to three years apart, and one baseline high-resolution T-1 MR imaging.

Table 6 shows the details about the subjects included in this work.

	All	**NC**	**MCI**	**Late stage AD**
Number (%F)	123 (54%)	109 (59%)	10 (30%)	4 (0%)
Age: mean ± standard deviation (range)	75±7 (50-90)	76±6 (65-90)	69±8 (57-85)	60±10 (50-73)
Δt (tau PET scans): in years	2.1±0.7	2.2±0.6	1.7±0.7	1.6±1.3

Table 6: Demographics. (%F) refers to the proportion of female subjects enrolled. Δt refers to the time elapsed between the tau PET scans: mean $\pm$ t standard deviation.

As noted in Section 2.1.3, only post-mortem analysis can confirm an AD diagnosis because of the multitude of neurodegenerative diseases that manifest as cognitive decline. The category to which subjects have been assigned is based on their neurological evaluation. Many conditions can explain the symptoms of subjects in MCI and/or late AD category such as sleep disorders, depression, stress, heavy drinking… These conditions can be excluded based on the medical history. However, currently there is no straightforward way to exclude other neurodegenerative diseases such as Pick's dementia, Lewy body dementia, or Parkinson's disease. Therefore, in the rest of the text, the diagnoses Healthy, MCI or late stage AD are only suspected, not confirmed.

6.2 Images reconstruction

Slight differences in the PET acquisitions exist for two main reasons: first, the subjects included in this work have been recruited for different studies starting at different times; second, the longitudinal nature of this work means that the accepted protocols for the experimental tau PET scans evolved with time. The tau PET scan was originally performed 80 minutes after the radiotracer's injection and for a duration of 20 minutes. Later, it was taken 75 minutes after injection for a duration of 30 minutes.

All the images are acquired on the Siemens/CTI ECAT HR+ scanner (3D mode) in 5-minutes frames. As a result, some of the images are composed of 4 frames, others are composed of 6 frames. For most of the subjects included in this work, their first scan is composed of 4 frames whereas their second scan has 6 frames.

To ensure a fair comparison between the tested methods and among subjects, we decided to limit our analysis to the first 4 frames of each scan. We have already used the notations $\boldsymbol{n_1}$ and $\boldsymbol{n_2}$ for the PET data from the acquisitions at t_1 and t_2 and $\boldsymbol{p_1}$ and $\boldsymbol{p_2}$ for their expected values. We noted $\boldsymbol{f_1}$ and $\boldsymbol{f_2}$ the corresponding images. In reality, $\boldsymbol{n_t}$ is composed of 4 frames that can be noted: $\boldsymbol{n_{t,1}}, \boldsymbol{n_{t,2}}, \boldsymbol{n_{t,3}}$, and $\boldsymbol{n_{t,4}}$ with $t = 1, 2$. The same applies for the images $\boldsymbol{f_1}$ and $\boldsymbol{f_2}$. For each scan, we perform the following operations:

- Separate reconstruction of the data contained in each frame for each time-point: the forward model is written $\boldsymbol{p_{t,l}} = \boldsymbol{H_t f_{t,l}}$ where $\boldsymbol{H_t}$ is the system matrix for the time-point t with $t = 1,2$ and $l = 1,2,3,4$. The update formula for the shifted Poisson model is given in Equation (35) in Section 4.3.2.6.

- Joint reconstruction of the data contained in the first frame for each time-point: the forward model is written $\begin{bmatrix} \boldsymbol{p_{1,1}} \\ \boldsymbol{p_{2,1}} \end{bmatrix} = \begin{bmatrix} \boldsymbol{H_1} & 0 \\ \frac{\alpha_{2,1}}{\alpha_{1,1}} \boldsymbol{H_2 R_1^T} & \alpha_{2,1} \boldsymbol{H_2 R_1^T} \end{bmatrix} \begin{bmatrix} \boldsymbol{f_{com,1}} \\ \boldsymbol{\tau_1} \end{bmatrix}$ where $\boldsymbol{R_1}$ is the registration between $\boldsymbol{f_{2,1}}$and $\boldsymbol{f_{1,1}}$ and $\alpha_{t,1}$ is the mean SUV in the reference region in $\boldsymbol{f_{t,1}}$. The update formulas are given by Equations (19) and (20) in Section 4.2.1.
- Separate reconstruction of the data contained in the second and third frames for each time-point: the forward model is written $\begin{bmatrix} \boldsymbol{p_{i,2}} \\ \boldsymbol{p_{i.3}} \end{bmatrix} = \begin{bmatrix} \frac{1}{\beta_{i,2}} \boldsymbol{H_i R_{i,2}^T} \\ \frac{1}{\beta_{i,3}} \boldsymbol{H_i R_{i,3}^T} \end{bmatrix} \boldsymbol{f_{i,(2)}}$ where $\boldsymbol{R_{i,l}}$ is the registration between $\boldsymbol{f_{i,l}}$ and the first frame $\boldsymbol{f_{i,1}}$ and $\beta_{i,l}$ is the decay factor between $\boldsymbol{f_{i,l}}$ and the first frame $\boldsymbol{f_{i,1}}$ with $i = 1,2$ and $l = 2,3$. The update formula for this model is given by:

$$\widehat{\boldsymbol{f_{\iota,(2)}^{(k+1)}}} = \frac{1}{\sum_{l=2}^{3} \frac{1}{\beta_{i,l}} \boldsymbol{R_{i,l} H_i^T} \mathbb{1}} \widehat{\boldsymbol{f_{\iota,(2)}^{(k)}}} \left(\sum_{l=2}^{3} \frac{1}{\beta_{i,l}} \boldsymbol{R_{i,l} H_i^T} \frac{\boldsymbol{n_{i,l}} + 2\overline{\boldsymbol{r_{\iota,l}}}}{\frac{1}{\beta_{i,l}} \boldsymbol{H_i R_{i,l}^T} \widehat{\boldsymbol{f_{\iota,(2)}^{(k)}}} + \overline{\boldsymbol{d_{\iota,l}}} + 2\,\overline{\boldsymbol{r_{\iota,l}}}} \right) \quad (37)$$

- Separate reconstruction of the data contained in the second, third, and fourth frames for each time-point: the forward model is written $\begin{bmatrix} \boldsymbol{p_{i,2}} \\ \boldsymbol{p_{i,3}} \\ \boldsymbol{p_{i,4}} \end{bmatrix} = \begin{bmatrix} \frac{1}{\beta_{i,2}} \boldsymbol{H_i R_{i,2}^T} \\ \frac{1}{\beta_{i,3}} \boldsymbol{H_i R_{i,3}^T} \\ \frac{1}{\beta_{i,4}} \boldsymbol{H_i R_{i,4}^T} \end{bmatrix} \boldsymbol{f_{i,(3)}}$. The update formula is given by:

$$\widehat{\boldsymbol{f_{\iota,(3)}^{(k+1)}}} = \frac{1}{\sum_{l=2}^{4} \frac{1}{\beta_{i,l}} \boldsymbol{R_{i,l} H_i^T} \mathbb{1}} \widehat{\boldsymbol{f_{\iota,(3)}^{(k)}}} \left(\sum_{l=2}^{4} \frac{1}{\beta_{i,l}} \boldsymbol{R_{i,l} H_i^T} \frac{\boldsymbol{n_{i,l}} + 2\overline{\boldsymbol{r_{\iota,l}}}}{\frac{1}{\beta_{i,l}} \boldsymbol{H_i R_{i,l}^T} \widehat{\boldsymbol{f_{\iota,(3)}^{(k)}}} + \overline{\boldsymbol{d_{\iota,l}}} + 2\,\overline{\boldsymbol{r_{\iota,l}}}} \right) \quad (38)$$

We introduce the notation $\boldsymbol{\tau_1}$ to emphasize that only the first frame of each scan was used to generate the difference image obtained by the joint reconstruction.

We additionally define the difference image obtained by the separate reconstruction of the data contained in the first frame of each scan:

$$\boldsymbol{\delta_1} = \boldsymbol{R_1}\frac{\boldsymbol{f_{2,1}}}{\alpha_{2,1}} - \frac{\boldsymbol{f_{1,1}}}{\alpha_{1,1}} \quad (39)$$

Similarly, the difference image obtained by the separate reconstruction of the data contained in the second and third frames of each scan is:

$$\boldsymbol{\delta_2} = \boldsymbol{R_1}\frac{\boldsymbol{f_{2,(2)}}}{\alpha_{2,(2)}} - \frac{\boldsymbol{f_{1,(2)}}}{\alpha_{1,(2)}} \quad (40)$$

Finally, the difference image obtained by the separate reconstruction of the data contained in the second, third, and fourth frames of each scan is:

$$\boldsymbol{\delta_3} = \boldsymbol{R_1}\frac{\boldsymbol{f_{2,(3)}}}{\alpha_{2,(3)}} - \frac{\boldsymbol{f_{1,(3)}}}{\alpha_{1,(3)}} \quad (41)$$

Therefore, we obtain 4 different images per subject. $\boldsymbol{\tau_1}$ and $\boldsymbol{\delta_1}$ are generated using the same number of counts, whereas $\boldsymbol{\delta_2}$ and $\boldsymbol{\delta_3}$ use twice and three times as much, respectively.

The methods generating the images $\boldsymbol{\tau_1}$,$\boldsymbol{\delta_1}$, $\boldsymbol{\delta_2}$, and $\boldsymbol{\delta_3}$ are called respectively **Joint**, **Diff_1**, **Diff_2**, and **Diff_3** in the rest of this text.

We compute the voxel-wise variance in our ROIs (EC, FG, ITG, HC, and PHG) for each of the 4 obtained images:

$$\sigma_{\text{Diff}-1}(\text{target}) = \text{std}(\boldsymbol{\delta_1}(\text{target})) \quad (42)$$

$$\sigma_{\text{Diff}-2}(\text{target}) = \text{std}(\boldsymbol{\delta_2}(\text{target})) \quad (43)$$

$$\sigma_{\text{Diff}-3}(\text{target}) = \text{std}(\boldsymbol{\delta_3}(\text{target})) \quad (44)$$

$$\sigma_{\text{joint}}(\text{target}) = \text{std}(\boldsymbol{\tau_1}(\text{target})) \quad (45)$$

We compute the ΔSUVR in the ITG and the FG for the 4 methods:

$$\Delta\text{SUVR}_{\text{Diff}-1}(\text{target}) = \frac{\text{mean}\big(\boldsymbol{\delta_1}(\text{target})\big)}{\text{SUVR}_{\mathbf{f_{1,1}}}(\text{target})} \times 100 \quad (46)$$

$$\Delta\text{SUVR}_{\text{Diff}-2}(\text{target}) = \frac{\text{mean}\big(\boldsymbol{\delta_2}(\text{target})\big)}{\text{SUVR}_{\mathbf{f_{1,(2)}}}(\text{target})} \times 100 \quad (47)$$

$$\Delta\text{SUVR}_{\text{Diff}-3}(\text{target}) = \frac{\text{mean}\big(\boldsymbol{\delta_3}(\text{target})\big)}{\text{SUVR}_{\mathbf{f_{1,(3)}}}(\text{target})} \times 100 \quad (48)$$

$$\Delta\text{SUVR}_{\text{Joint}}(\text{target}) = \frac{\text{mean}\big(\boldsymbol{\tau_1}(\text{target})\big)}{\text{SUVR}_{\mathbf{f_{com,1}}}(\text{target})} \times 100 \quad (49)$$

We investigate the mean and the variance of the SUVR change among subjects and groups of subjects and study the separability between these groups.

PART III RESULTS & DISCUSSION

CHAPTER 7. Validation results

We have proposed a new joint reconstruction framework (Section 4.2) for deriving region-wise tau accumulation rate from longitudinal PET studies. We first implement the single time-point reconstruction for the ECAT HR + system (Sections 1.3.2 and 4.3.2) to produce the difference image used in the conventional subtraction method. To gauge the performance of the new method, we test it on images with artificially increased tau accumulation in the ITG (CHAPTER 5). In this chapter, we compare our OSEM reconstruction to the scanner's and present the results for the joint reconstruction for the numerical simulations.

7.1 Validation of the reconstruction scheme

We run the single time-point reconstruction (OSEM derived in Section 4.3.2.6, 4 iterations, 16 subsets) for the first frame of the first time-point measurement for one subject and we apply gaussian smoothing afterwards on the obtained image as there is a post-processing step included in the ECAT HR+ OSEM reconstruction (also with 4 iterations, 16 subsets). We compare the reconstructed image to the scanner's through a line plot across the two images. In Figure 9, (A) shows the line plot on the image from the scanner and (B) shows the same line on the image obtained with our reconstructed image. The profiles shown in (C) are similar meaning that our implementation for the single time-point reconstruction succeeds in retrieving the PET image.

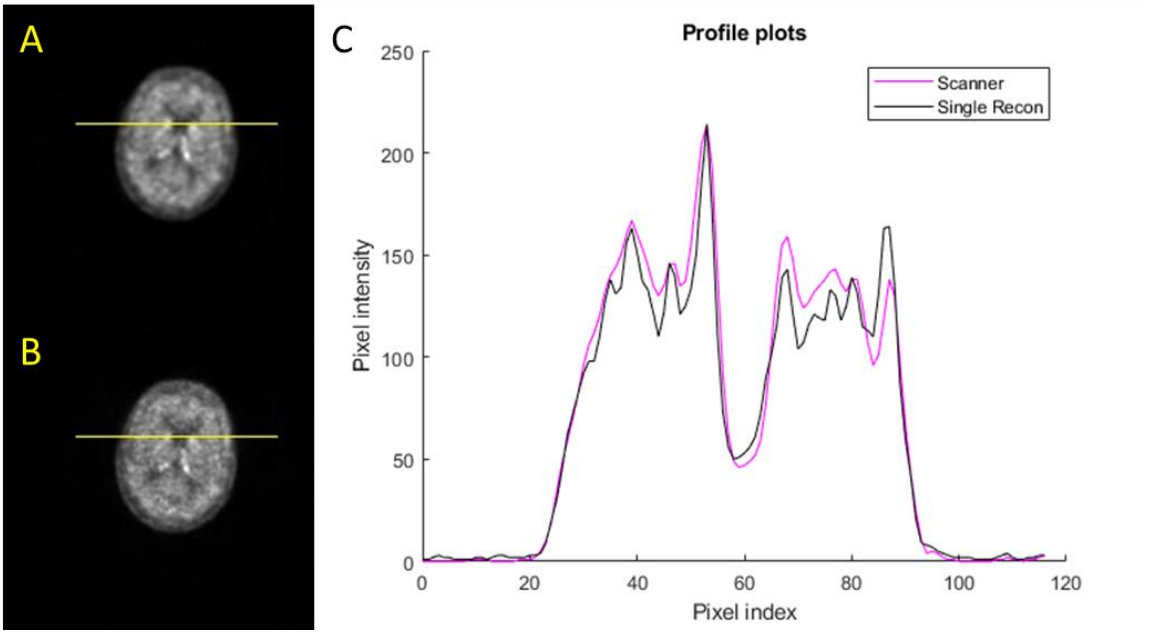

Figure 9: Comparison between the scanner and the implemented single time-point reconstruction. (A) is the image from the scanner with an overlaid line plot. (B) shows the same line plot on the reconstructed image using our OSEM implementation. (C) represents the profile plots along the line in (A) and (B).

The corrections techniques, explained in Section 1.2, were used for both the single and the joint reconstruction. Knowing that we get images like the scanner's gives us a higher confidence in the estimated sensitivity, attenuation, and scatter.

In the next section, we study the joint reconstruction's performance in estimating the difference image when the expected tau accumulation is known.

7.2 Evaluation on images with a known artificial increase in tau deposition

We simulate an artificial higher uptake in the ITG (simulated increases of 3, 5, 7 and 10%) in one subject's scan as described in CHAPTER 5. The original image before the simulated increase is called the background image and mimics the image obtained by the single time-point reconstruction for the first acquisition. The simulated image with the increase in tau

accumulation represents the image obtained by the single time-point reconstruction for the second acquisition.

Determining the position of the ITG in the background image requires accurate registration of the MR image and the segmentation labels onto the PET images. Figure 10 shows two slices used to study the registration of the ITG (A) and the cerebellum cortex (B) serving as a reference region. (A1) and (B1) show the volumes as they were defined on the high-resolution MR image. (A2) and (B2) show the MR image after it was registered to the PET image with the overlaid contours of the volumes of interest. Those same volumes are finally shown directly on the PET image (A3 and B3) and are used to compute the SUVR and subsequently to simulate a second time-point with an increasing level of a change in the SUVR.

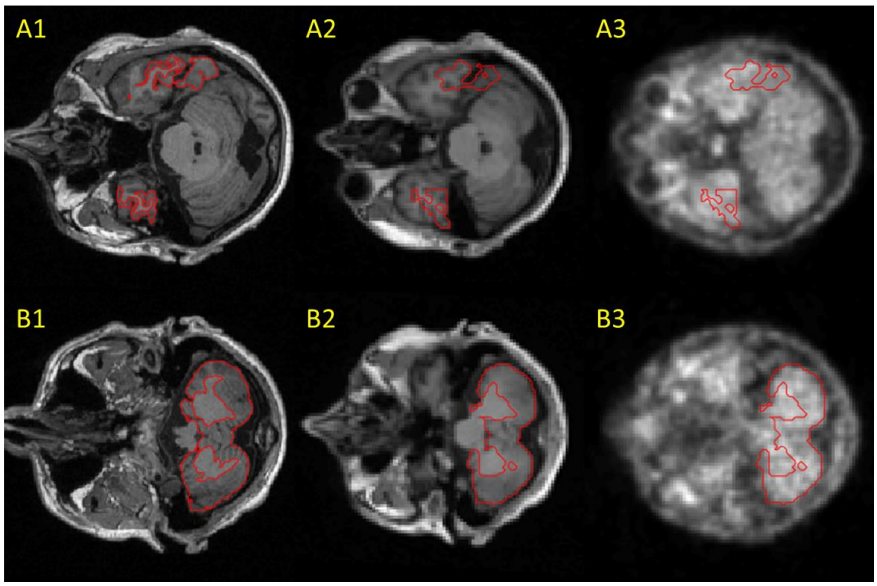

Figure 10: The performance of the image registration. (A) shows the ITG and (B) shows the cerebellum cortex used as the reference region. Panel (1) presents the MR images with the overlaid masks from FreeSurfer segmentation. Panel (2) shows the same MR volumes after they were registered to the PET images. Panel (3) overlays the registered masks on the PET images.

The background image and the simulated second time-point are subtracted to generate a difference image and their corresponding PET data are fed into the joint reconstruction framework. As explained in Section 4.2.1, the joint method produces two images: the common image which represents the background image in the case of the simulated increased tau uptake, and the difference image which directly gives a map of the simulated change in SUVR.

To validate our reconstruction, we look at the obtained common image and compare it to the background image (Figure 11) and the difference images for increasing levels of simulated tau uptake (Figure 12).

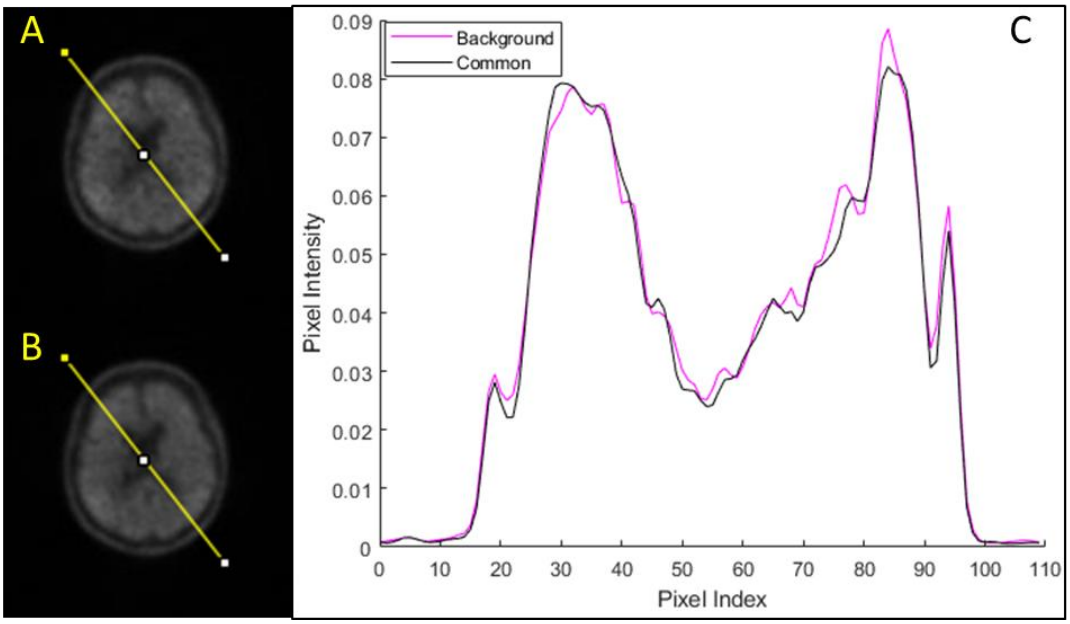

Figure 11: Comparison between the background image (A) and the common image (B) obtained by the joint reconstruction, The profile plots in (C) of the line displayed in (A) and (B) show that the images are very similar.

In Figure 12, it is obvious that the simulated tau accumulation is clearly visible for the joint reconstruction (B) whereas the conventional difference images barely show any signal (C). The MR image with the location of the simulated increase in tau uptake is given in (A).

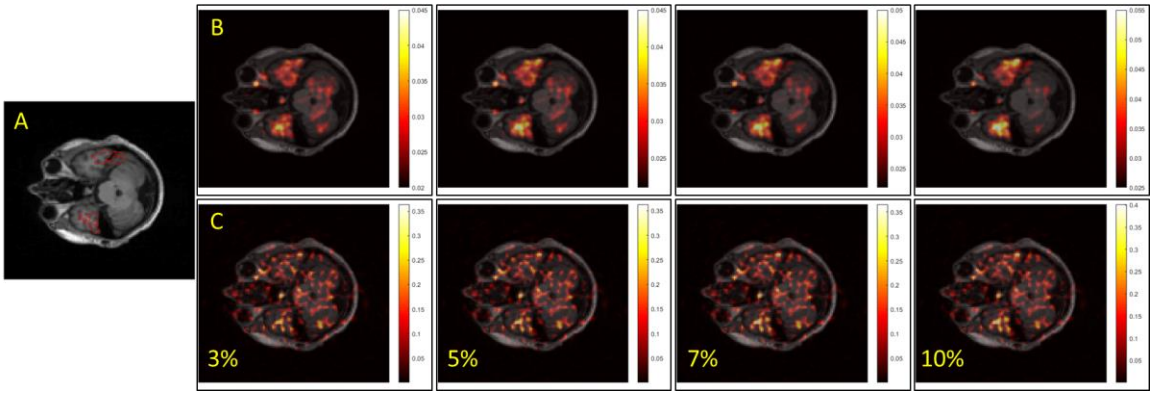

Figure 12: The difference images for the simulated increase in tau accumulation. (A) shows the MR image with the ITG mask. Panel (B), in the top row, is composed of the difference images obtained by the joint reconstruction. Panel (C), in the bottom row, shows the difference images obtained by subtraction of the two images reconstructed separately. The level of the simulated increase in the tau deposition is also displayed. In panels (B) and (C), the PET images are shown with the colormap "hot" overlaid over the MR images (gray scale).

To quantify the differences in signal shown in the images obtained by the two method, we introduce the sensitivity index, a measure of the signal detectability[122], given by:

$$d' = \frac{\mu_S - \mu_N}{\sqrt{\frac{1}{2}(\sigma_S^2 + \sigma_N^2)}}$$

μ_S is the mean value of the signal in the target region (here the ITG) and μ_N is the mean value of the signal in a background region. We chose to use the FG as a background region because it is also large enough to counter the effects of registration errors. σ_S and σ_N are the standard deviations of the signal in the target and the background regions, respectively. We compute the index for all reconstructed images, and we plot it as a function of the levels

of increase in tau accumulation. As seen before, Figure 13 shows that the sensitivity index is higher for the joint reconstruction for all levels of tau accumulation increases. Naturally, the sensitivity is proportional to the level of the simulated increase in tau uptake.

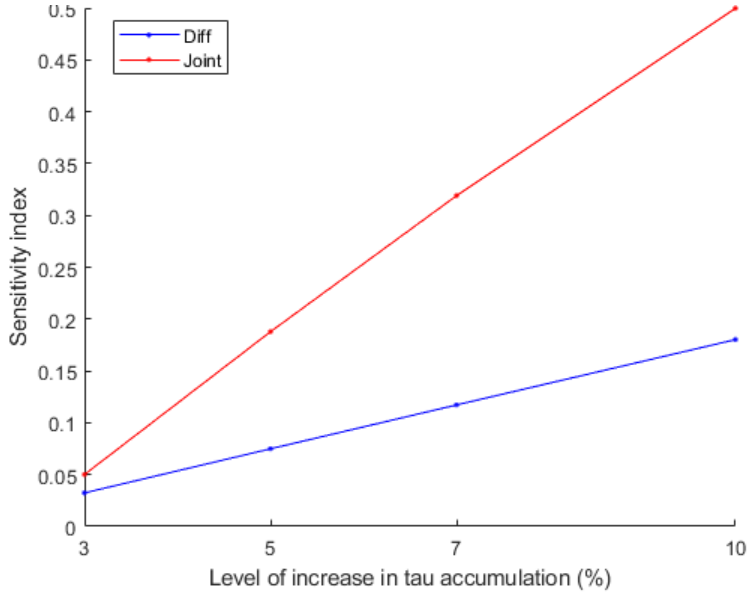

Figure 13: Sensitivity index in the difference images produced by the two methods as a function of the level of simulated increase in tau accumulation

We have explained in Section 6.2 that every subject scan performed on ECAT HR+ is composed of 4 to 6 frames. The reconstruction performed above only includes two frames: one frame was used as a background image and another one contained the artificially increased tau uptake. To realize 4 more noise realisations, we use the remaining frames to add the increased tau accumulation.

We calculate the ΔSUVR in the ITG for the conventional method (noted **diff**) as a percentage of the SUVR in the background image for each noise realization *s*:

$$\Delta\mathrm{SUVR}^{(s)}_{\mathrm{diff}}(\mathrm{ITG}) = \frac{\mathrm{SUVR}^{(s)}_{\mathbf{simulated}}(\mathrm{ITG}) - \mathrm{SUVR}_{\mathbf{background}}(\mathrm{ITG})}{\mathrm{SUVR}_{\mathbf{background}}(\mathrm{ITG})} \times 100 \quad (50)$$

For the joint reconstruction, noted Joint, for each noise realization, the difference image $\boldsymbol{\tau}^{(s)}$ is a map of the change in SUVR in every voxel whereas the common image $\boldsymbol{f}_{\boldsymbol{com}}^{(s)}$ reflects the background image. The ΔSUVR in the ITG is then given by the ratio between the mean value of the image $\boldsymbol{\tau}^{(s)}$ in the ITG and the SUVR of the ITG in the common image:

$$\Delta\mathrm{SUVR}_{\mathrm{joint}}^{(s)}(\mathrm{ITG}) = \frac{\mathrm{mean}\left(\boldsymbol{\tau}^{(s)}(\mathrm{ITG})\right)}{\mathrm{SUVR}_{\mathbf{f_{com}}}^{(s)}(\mathrm{ITG})} \times 100 \quad (51)$$

We have noticed that some of the signal added to the second time-point is retrieved in the common image. We estimate this signal loss thanks to the difference between the common and the background images. To avoid adding additional noise to the difference image reconstructed with the proposed method, we average the estimated signal loss across the ROI and add it to back to the difference image. We can now compute the bias and the variance across the noise realizations for both methods.

For a simulated increase c, the bias and the standard deviation for each method, for $N = 5$ noise realizations, are:

$$\mathrm{bias}_{\mathrm{method}}(\mathrm{ITG}) = \frac{1}{\mathrm{N}}\sum_{\mathrm{s=1}}^{\mathrm{N}}\left(\Delta\mathrm{SUVR}_{\mathrm{method}}^{(s)}(\mathrm{ITG}) - c\right) \quad (52)$$

$$\sigma_{\mathrm{method}}(\mathrm{ITG}) = \sqrt{\frac{1}{\mathrm{N}-1}\sum_{\mathrm{s=1}}^{N}\left(\Delta\mathrm{SUVR}_{\mathrm{method}}^{(s)}(\mathrm{ITG}) - \frac{1}{5}\sum_{\mathrm{s=1}}^{5}\Delta\mathrm{SUVR}_{\mathrm{method}}^{(s)}(\mathrm{ITG})\right)^{2}} \quad (53)$$

We plot the bias and the standard deviation as a function of the iteration number in the OSEM reconstruction for a simulated increase of 5% in Figure 14 and Figure 15.

We notice that the joint reconstruction shows a drastically reduced variance compared to the conventional method. Both methods exhibit a comparable bias.

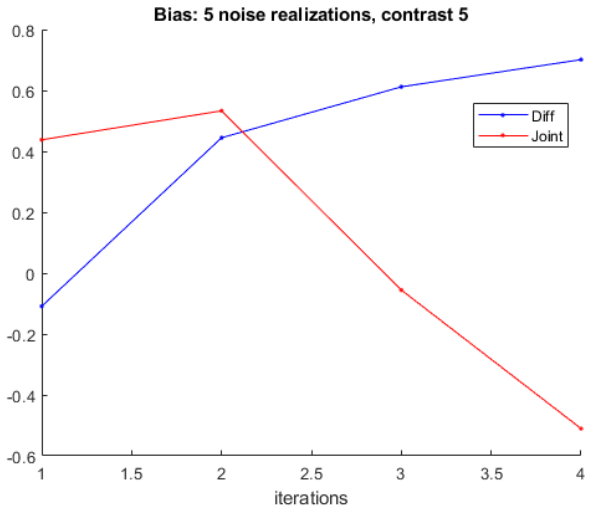

Figure 14: Bias of the conventional and the proposed methods.

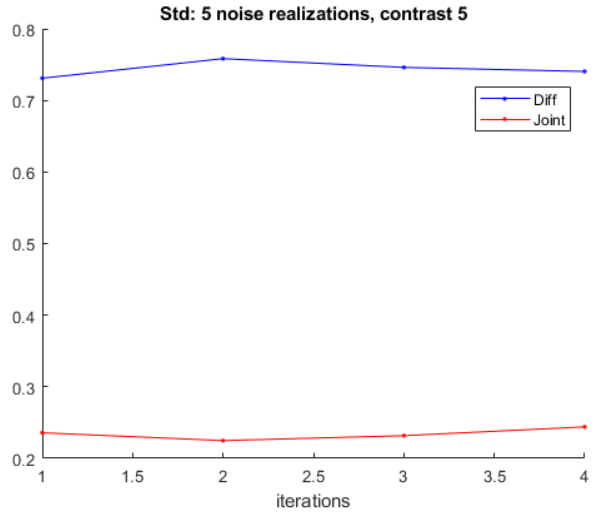

Figure 15: Standard deviation for the conventional and the proposed methods

CHAPTER 8. Application to human studies

We have validated our reconstruction implementation, including PET data corrections, against the scanner reconstruction. We have also tested the joint method on numerical simulations and showed it performed better than the conventional method for the signal detection. We now investigate its performance on the human subjects' dataset and compare it to the conventional method implemented using the same, double, and triple number of counts.

8.1 Image reconstruction

We have already seen the importance of registration to determine the ROIs for the reconstruction of the images wherein tau accumulation was artificially increased (Figure 10). Accurate registration plays an even more important role for the reconstruction of human subjects' dataset since the registration matrix is included in the model, whether it is the joint reconstruction framework (**Joint**) in Equations (19) and (20), or the conventional method incorporating more than one frame (**Diff_2** and **Diff_3**) in Equations (37) and (38). For the method **Diff_1**, the model does not include a registration matrix because acquisition is reconstructed separately using only the data from one frame. However, the registration is still needed to get the difference image as shown in Equation (39).

We followed the following steps for the registration in our implementation:

- the MR image is registered to the transmission image at t_1 and t_2
- the transmission image at t_2 is registered to the transmission image at t_1
- the transmission image is registered to the first frame for t_1 and t_2

- the subsequent frames are registered to the first frame for t_1 and t_2

Figure 16 shows an overlay of the first frame for each time-point before registration (A) and after registration (B).

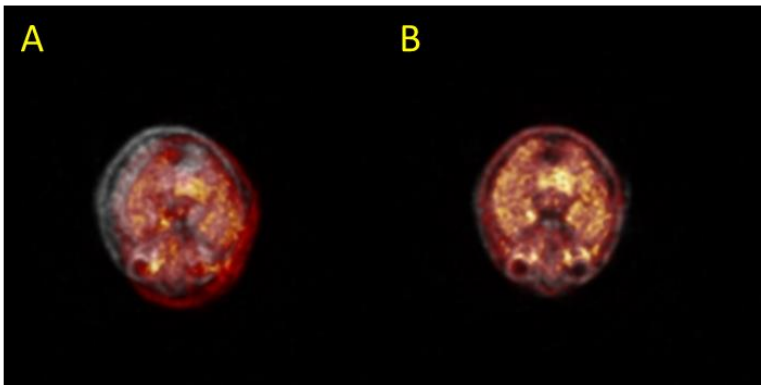

Figure 16: Registration between the time-points. We show the PET images at t_1 and t_2 before (A) and after registration(B). The image at t_1 is displayed with a gray scale. The image at t_2 is displayed with the colormap "hot".

Visually, the rigid registration works well. However, the results depend on the case considered as some cases display greater motion between the frames and/or drastic change between the two time-points. Therefore, we cannot ignore the possibility that our results might suffer from registration uncertainties.

We have implemented 4 methods for reconstructing subjects' images in Section 576.2:

- **Diff_1**: separate reconstruction of the data in the first frame
- **Diff_2**: separate reconstruction of all the data in both, the second and the third frames
- **Diff_3**: separate reconstruction of all the data in the second, the third and the fourth frames
- **Joint**: the joint reconstruction of the data in the first frame

All reconstructions were OSEM-based performed with 4 iterations and 16 subsets.

Figure 17 shows the voxel-wise change in SUVR given by the 4 difference images obtained for one dataset from each subgroup: $\boldsymbol{\delta_1}$ in Equation (39), $\boldsymbol{\delta_2}$ in Equation (40) , $\boldsymbol{\delta_3}$ in Equation (41), and $\boldsymbol{\tau_1}$.

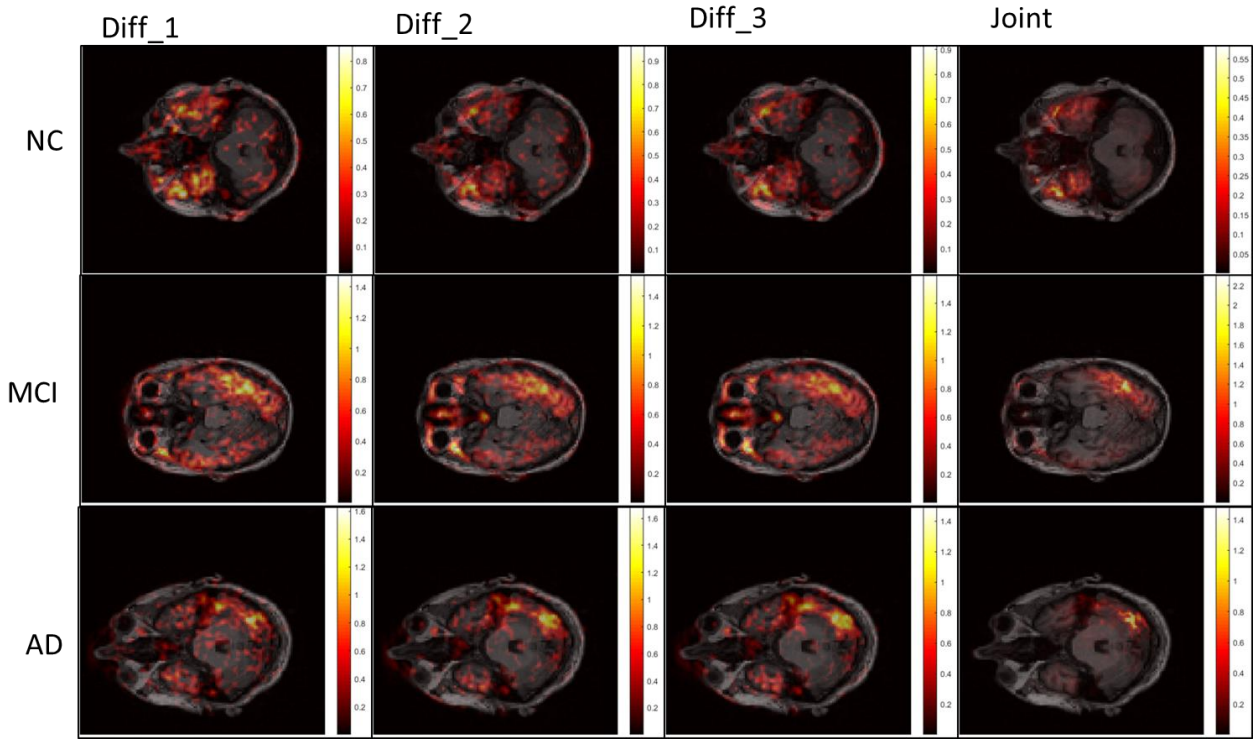

Figure 17: Example of difference images for the 4 reconstruction methods. The rows show the images from a healthy subject, an MCI subject, and an AD subject. The images in the first three columns are obtained by the conventional method with an increasing number of included frames in the reconstruction. The last column shows the images of the joint reconstruction. The PET images are displayed with the colormap "hot" overlaid over the MR images (gray scale).

As expected, the signal in the images obtained from **Diff_3** displays better contrast than **Diff_1** and **Diff_2**, but the noise is visible across all the images. The signal in the images obtained by **Joint** is well defined. High intensity regions are the same across all methods.

To quantify the variance reduction in the image, we compute the voxel-wise standard deviation in the ROI for each subject in the 4 images representing the change in SUVR in every voxel as explained in Equations (42), (43), (44), and (45).

We compute the average across all subjects, noted $\bar{\sigma}$, for our 5 ROIs and we report the results in Figure 18. The standard deviation indeed decreases as we add more frames, and therefore more signal, in the reconstruction. The drastic decrease in the variance by the joint reconstruction explains the improvement of the contrast exhibited in Figure 17.

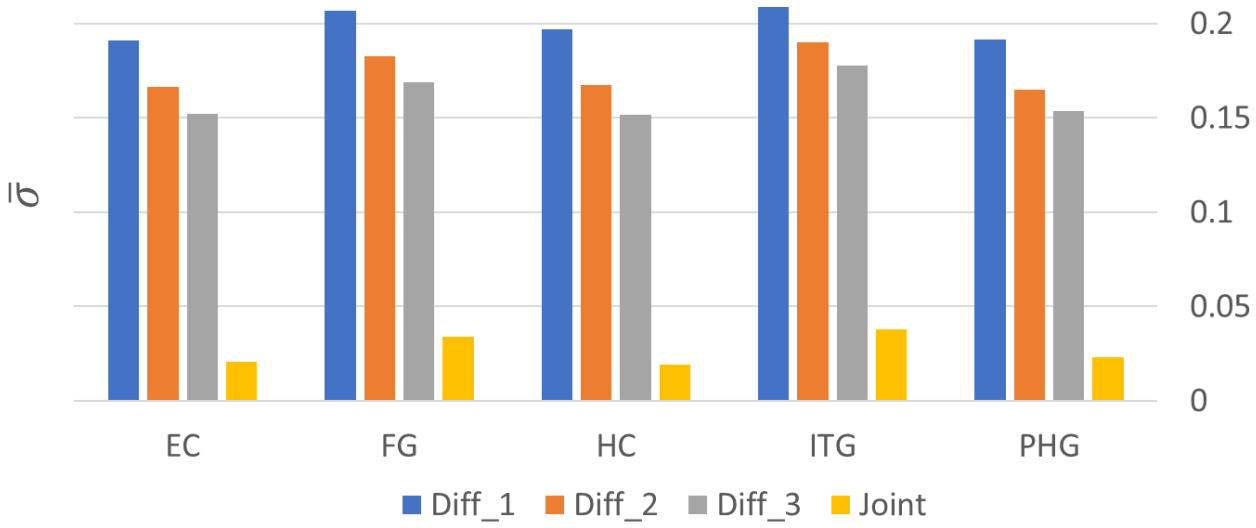

Figure 18: Regional variance averaged across all subjects obtained from the 4 difference images showing the voxel-wise change of SUVR between the two time-points.

8.2 Variance reduction in patient study

We apply the reconstruction methods explained earlier to all the subjects and compute the ΔSUVR for each method in the ITG and the FG as explained in Equations (46), (47), (48), and (49).

Figure 19 and Figure 20 show the boxplots[123] for the obtained ΔSUVR for each method for the ITG and the FG, respectively. The box is formed by the first (Q_1) and the third (Q_3) quartiles, while the red line in the middle of the box shows the median value (Q_2). The red + points reflect the data points that are considered outliers: they are greater than $Q_3 + 1.5 \times (Q_3 - Q_1)$ or smaller than $Q_1 - 1.5 \times (Q_3 - Q_1)$. The whiskers extend from the box to the most extreme data points that are not considered outliers.

First, we notice that adding more frames in the separate reconstruction does not translate to a smaller variance among subjects: the added signal only plays a role in the variance in the image (as seen in Figure 17 and Figure 18) but the value of change in SUVR does not change much. Indeed, the variance shown here is composed of the inherent variance of the SUVR change across the subjects and the variance related to the reconstruction method. Second, the separate reconstruction methods, regardless of the number of frames included, yield negative values for many subjects: we know that tau deposition can only increase with time, so those values reflect the noise of the acquisitions and/or the registration errors. By design, the joint reconstruction does not allow for negative ΔSUVR. As a result, the median value (1.5%) for the joint method is slightly elevated when compared to the conventional method. As expected, it is low for our dataset comprised mainly of healthy controls.

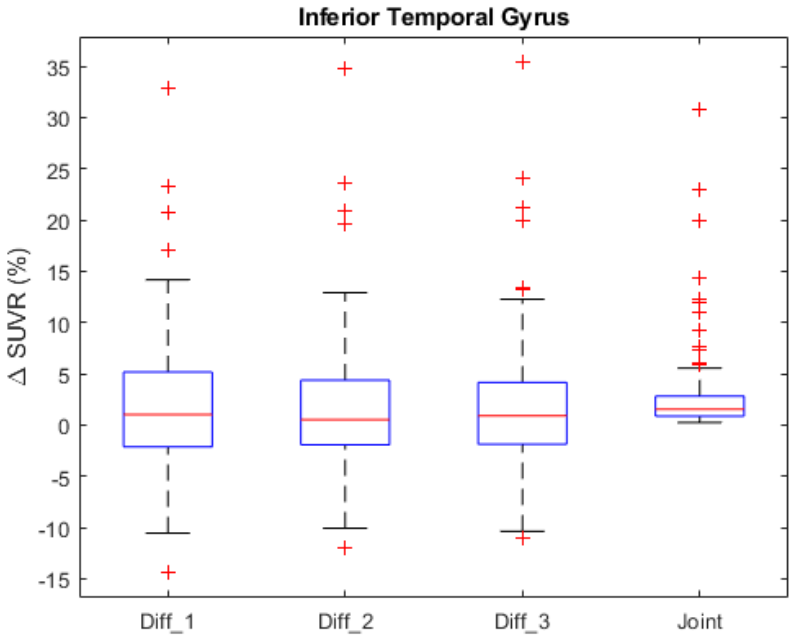

Figure 19: Boxplot of ΔSUVR (expressed as a percentage of the SUVR in image at t_1) in the ITG, computed for each subject, for each proposed method.

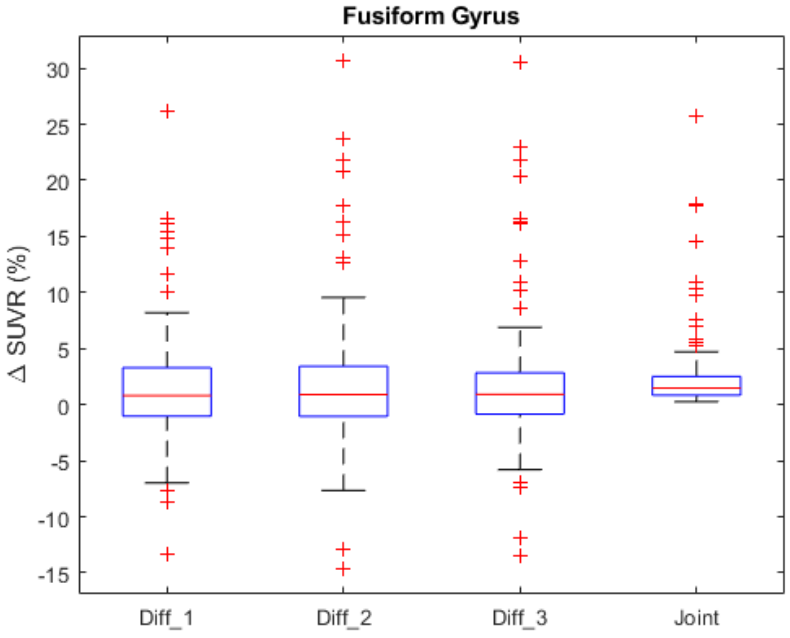

Figure 20: Boxplot of ΔSUVR (expressed as a percentage of the SUVR in image at t_1) in the FG, computed for each subject, for each proposed method.

The most important result from the figures above is the drastically reduced variance for the joint reconstruction. Naturally, it is explained in part by the lack of negative values, but it is not the only reason. The joint reconstruction inherently reduces the variance. We restrict the boxplot in the ITG for the separate reconstruction methods to positive values of ΔSUVR and we report the result in Figure 21. The variance is still a lot smaller for our proposed method as opposed to the conventional method regardless of the number of frames used. We notice that the exclusion of negative values from the separate reconstruction's results lead to a higher median for ΔSUVR. This contributes to the confusion about a typical/expected change for healthy controls and/or MCI/AD subjects tackled in APPENDIX A. Typical SUVR change in clinical studies.

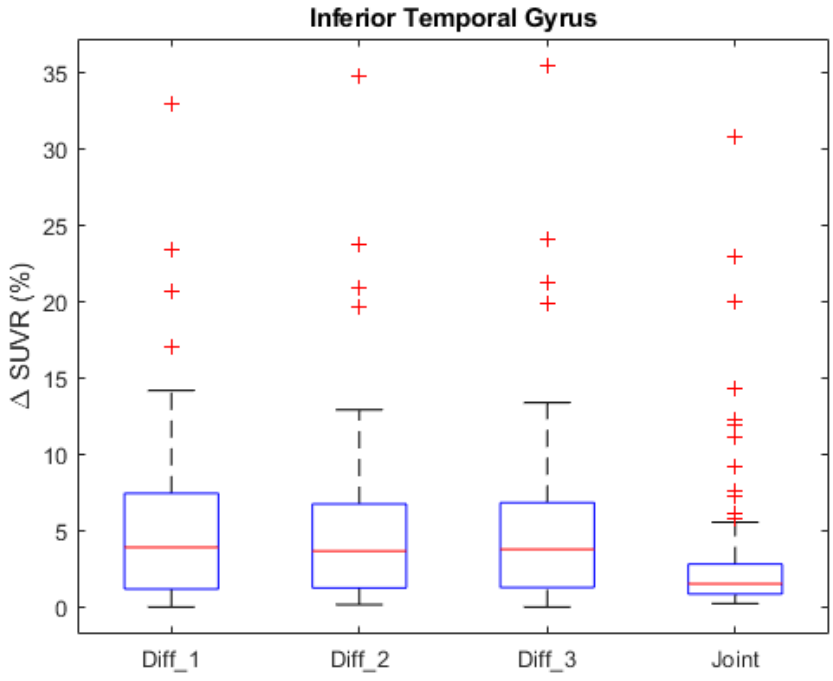

Figure 21: Boxplot of ΔSUVR in the ITG wherein only positive values are considered

8.3 Sample size

To investigate the separability between groups using the patients data, we extract 22 subjects from the healthy control's group exhibiting change in SUVR (based on Diff_3 separate reconstruction, in the FG) that falls between the 70th percentile (to exclude negative and small values) and the 90th percentile (to exclude outliers). This subgroup was compared against the 10 MCI subjects to gauge the performance of the two methods in separating between NC and MCI. We perform the t-test for the separation between the two groups for both methods: the p-value for Diff_3 is 0.4 and for Joint is 0.04. The joint reconstruction finds a significant difference between the two groups. We additionally plot the Receiver Operating Characteristic[124] (ROC) curve for both methods in Figure 22.

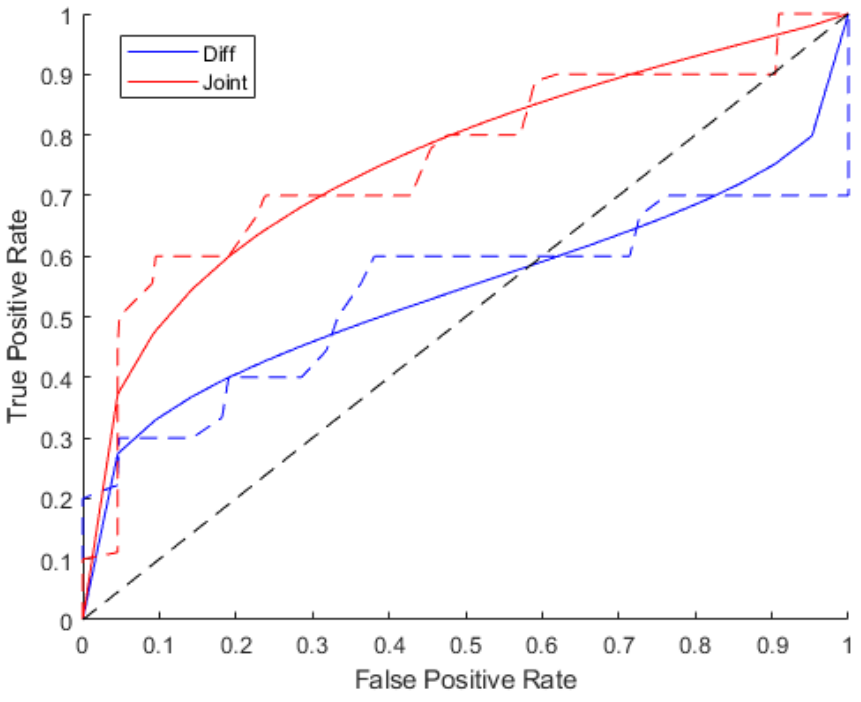

Figure 22: ROC for separability between NC and MCI

As previously noted, the difference method cannot separate between the groups of NC and MCI in this case. The joint reconstruction performs better but it is still far from ideal. This is related to the heterogeneous nature of tau uptake in the MCI group, as the values of SUVR changes varied from 1.1% to 20% for Diff_3 and from 0.6% to 7.6% for Joint. To explain the heterogeneity of the MCI group, it is important to remember that the distinction between the two groups is based on their cognitive function. The decline seen for the MCI subjects can be of various degrees depending on the nature of the neurodegenerative disease causing the decline and its progression.

Using the mean value and the variance from the groups above, we estimate the sample size based on two-sample pooled z-test[125] for normally distributed data with known and equal standard deviations. We assume the power of the test to be 90% ($\beta = 0.1$) with a significance level of 5% ($\alpha = 0.05$). The sample size for one-sided test ($H1:\ \mu_{MCI} > \mu_{NC}$) is then given by[125]:

$$n = \left(z_{1-\alpha} + z_{1-\beta}\right)^2 \frac{2\sigma^2}{(\mu_1 - \mu_2)^2} \quad (54)$$

μ_1 and μ_2 are the mean of the samples from the two different groups. σ is the pooled standard deviation: $\sigma = \sqrt{\frac{(n_1-1)\sigma_1^2+(n_2-1)\sigma_2^2}{n_1+n_2-2}}$. z_x is the critical value for the standard normal distribution evaluated at x.

We assume a ratio of 5 between the healthy controls and the MCI/AD subjects. **The sample size is 482 for the conventional method and 104 for the joint reconstruction.**

CHAPTER 9. Discussion

The joint reconstruction method reduces the variance in two ways: in the difference image leading to a better contrast, and in the change of SUVR across groups of subjects leading to a smaller sample size for a hypothetical clinical trial. Both reductions of variance can be imputed to the positive constraint as it restricts the signal and acts as a regularization of the signal.

Currently, the difference image is overlooked as the regional distribution of tau accumulation rates is not important. Instead, researchers focus only on the region-wise change derived from the subtraction of the SUVR from the images reconstructed separately at t_1 and t_2. As we are learning more about the properties of [^{18}F]-AV-1451, the difference image might become important to identify regions more suitable to be the reference if they don't show a change in tau uptake. Likewise, the decrease in the noise shown in the images obtained by joint reconstruction is useful to distinguish off-target binding from the noise.

As for the reduction of the variance among groups of subjects, more work is needed to determine if it holds true for all regions involved in AD. In our study, we were limited to the FG because of the values of ΔSUVR reported in the MCI group: most of them were negative for the conventional method in the other considered regions (EC, HC, ITG and PHG). The inherent noise in PET data and the registration errors can explain these findings. The effect may be minimized by a new registration scheme. In our work, the second time-point is transformed to match the first scan. The transformation applies a filtering that results in additional smoothing in the transformed image. The smoothing might reduce the signal in the second image leading to the detection of a negative change in the SUVR. We

can avoid this effect in the conventional method by registering the MR to the PET images separately and calculating the SUVR in each image without registering them to each other. However, the transformation between the two time-points is always needed in the joint reconstruction. The registration of both time-points to a common space to make the process symmetrical could be investigated. The definition of bigger regions composed of the weighted average of the studied ROIs might alleviate some of the registration problems[126], [127]. Currently, negative values are simply ignored during the analysis to determine the change in tau accumulation. Note that only the regions with negative values are discarded, and not the entire data from that subject. It is common that, for one subject, some regions exhibit detectable increases in tau deposition whereas others yield a negative change in the SUVR. Obviously, the joint reconstruction using OSEM with its positive constraint, circumvents the problem, but inevitably introduces bias in the estimated ΔSUVR. This bias is exacerbated by the pre-corrected PET data because the shifted Poisson model introduces bias when adding the estimated random coincidences back to the measured data. Thankfully, the performance of the method for the separability between two groups showing different tau uptake is linked to the variance and is independent of the bias, if it is the same for both groups. Subjects with low tau accumulation rate between the two scans are more likely to lead to negative ΔSUVR and thus to a bias in the joint reconstruction. If we assume that the healthy control group shouldn't report any tau accumulation, then the bias introduced by the proposed method in this group is expected to be larger than the one for a group of subjects with faster tau accumulation rate. Note that the good results we obtained for the separability task were estimated on a small subset of the data because we had to ignore many subjects with negative ΔSUVR in the FG.

Another limitation with the joint reconstruction using OSEM is its main highlight: the positive constraint. Remember that the reason behind this work is the importance of reducing the sample size to make clinical trial more affordable. The results reported in Section 8.2 show a dramatic decrease in the sample size for the proposed method. A hypothetical clinical trial would enroll X subjects with a known degree of tauopathy. At enrollment, all undergo a tau PET scan. Half of the subjects are given a drug that should slow down the tau accumulation. The other half is only monitored. After a year, a second tau PET scan is acquired and the joint reconstruction yields ΔSUVR per subject. If the monitored group exhibits 7% increase and the treated group has 5% increase, then the joint reconstruction can successfully separate between the two groups as long as the sample size is sufficient. However, if the treatment is very efficient and leads to a decrease in tau protein (which is the end goal for AD research), then the joint reconstruction can never retrieve the true ΔSUVR. The method itself should be modified to allow for negative values. Reconstruction algorithms like NEG-ML[128] and AB-ML[129] were proposed to reduce the bias introduced by the positivity constraint imposed by MLEM[130]. The question is then if the promising results reported in this work will hold.

Since the change of SUVR is only calculated in a small number of ROIs, we can also use a masked joint reconstruction: the difference image is only updated in one ROI. To avoid negative values in that region, we can then use the value given by the conventional method to tell us which time-point has higher tau uptake. The joint reconstruction can take advantage of such information to choose which time-point scan as the baseline. If the change in SUVR given by the conventional method is negative, then we can set the scan acquired at t_2 as the baseline scan.

In the future, we want to evaluate the joint reconstruction results using a BSREM[131] algorithm incorporating the two following priors:

- A temporal Huber penalty[132] ensures that the difference between the two time-points is small
- A Structural similarity (SSIM)[133] prior ensures that the images at t_1 and t_2 are similar.

Preliminary results are available and presented in APPENDIX B. Phantom study.

Conclusion

The goal of this work was to develop a joint reconstruction method for longitudinal tau PET studies to detect small regional changes in tau accumulation facilitating the design of clinical trials by the reduction of the sample size required. This new framework reconstructs the difference image between two time-points directly from the PET measurements by incorporating a registration transformation to account for the head misalignment in the two acquisitions and scaling factors to solve the problem of the different injected doses. It relies on the principle that the tau protein increases with age across all subjects.

We have, first, implemented our own reconstruction software to reproduce the images acquired on the ECAT HR+ scanner. The separately reconstructed images are used as a validation tool against the scanner's images to gauge the accuracy of our single time-point reconstruction algorithm. They are also needed for the estimation of the parameters needed for the proposed method such as the registration matrix and the scaling factors. Finally, we derive tau accumulation rates in regions known to be involved in early AD such as the inferior temporal gyrus and the fusiform gyrus according to the conventional method that consists in taking the difference between the SUVR calculated from each single time-point image.

We have developed the joint reconstruction model and discussed the implementation details to apply it on the PET data from the scanner. The joint approach produces two images: the common image that translates the common signal between the two scans and the difference image that reflects the accumulation in tau. We have used one subject's

images to simulate increasing levels of added accumulation in the inferior temporal gyrus to test our proposed solution. We have validated the method by comparing the common image to the background image. The jointly reconstructed difference image achieves better contrast in the target region than the one obtained for the conventional method. We have taken advantage of the frames composing each scan to simulate multiple noise realizations and evaluated the bias and the variance of our method. We confirmed the reduction of the variance attained by the proposed method.

The longitudinal studies performed at our institution gives us a unique opportunity to apply the joint reconstruction on a large dataset comprised of 123 subjects. We have calculated the change of the SUVR for each subject and reported a drastically reduced variance across subjects for the proposed method. This achievement can be explained by the positivity constraint required by the derivation of the joint reconstruction algorithm. The reduced variance leads to a smaller sample size estimated from two subgroups of the available dataset.

We finally discuss the limitations of the proposed method such as the uncertainty of the acquisitions, the registration errors, the evolution of our knowledge of the [^{18}F]-AV-1451 tracer, and the need for relaxing the positive constraint. We propose some ideas for further work on this project: the implementation of a reconstruction framework that allows for negative values, the incorporation of temporal priors on the difference image, and the modification of the registration scheme. The continuation of the HABS leading to longitudinal studies composed of three or more acquisitions entices us to expand our method for more time-points.

The achieved reduction of variance among subject is a very promising result in AD research as it paves the way for shorter inter-scans time, leading to more rapid assessment of the impact of the intervention on tau burden.

APPENDIX A. Typical SUVR change in clinical studies

Tau deposition increases with age but the accumulation rate of tau protein in the brain is accelerated in early AD. The goal of longitudinal studies is to track the change of tau accumulation with time. However, distinguishing between normal aging and signs of prodromal AD is not straightforward. We want to try and answer that question with HABS. Early results from Dr. Johnson seem to indicate a yearly increase of 1% to 10% in the SUVR. Another longitudinal study conducted at Mayo Clinic[127] reported no increase in healthy individuals whose amyloid PET scan is normal, a 0.5% yearly increase for healthy individuals with abnormal amyloid PET, and a 3% yearly increase for subject with MCI and an abnormal amyloid PET.

A test-retest study[126] on 21 subjects (5 NC, 6 MCI, and 10 AD) where [^{18}F]-AV-1451 PET scans were acquired within 48 hours to 4 weeks showed a change of 2% in the SUVR with an outlier at 10%. The SUVR were calculated on a large neocortical region to counter the errors introduced by the registration. It is safe to assume that our results exhibit an even larger variation in the ΔSUVR considering the relatively smaller regions and the time elapsed between the scans. Any detected change in ΔSUVR has a component that is present regardless of the advancement of tauopathy, making it hard to determine an expected change for healthy controls versus MCI/AD subjects. We also don't know the effect of this component as it can contribute to the increase of the decrease of the measured ΔSUVR regardless of the true change in SUVR. The negative values obtained by the conventional method (Figure 19 and Figure 20) can also be explained by this inherent variation of PET images.

Dynamic tau PET imaging[91] also suggests that the SUVR changes during the acquisition time used for our imaging (80-100 min or 75-105min post injection), especially for AD subjects[92].

We evaluated the change of SUVR between the 5min frames in one scan composed of 6 frames. The scan was chosen because the motion between the frames was minimal, and thus, we hope that the detected SUVR change is not due to registration errors. We report the change as a percentage of the SUVR in the previous frame in Figure 23:

$$\Delta\mathrm{SUVR}(\mathrm{Target}) = \frac{\mathrm{SUVR}_{\mathbf{f}}(\mathrm{Target}) - \mathrm{SUVR}_{\mathbf{f-1}}(\mathrm{Target})}{\mathrm{SUVR}_{\mathbf{f-1}}(\mathrm{Target})} \times 100 \quad (55)$$

The SUVR in the considered frame **f** is noted $\mathrm{SUVR}_{\mathbf{f}}(\mathrm{Target})$ and the SUVR in the previous frame is noted $\mathrm{SUVR}_{\mathbf{f-1}}(\mathrm{Target})$.

We note that the EC exhibits larger changes: its small size makes it particularly vulnerable to registration errors. This figure is the reason why we focused most of our analysis on the ITG and the FG. CWM is the cerebral white matter; its large size explains the small change in the SUVR, but it still reaches 2% for a duration of 5 min. Our limited understanding of the tracer can be behind this phenomenon: the off-target binding of [^{18}F]-AV-1451 makes it hard to quantify tau accumulation in some regions[134].

We conclude that the assumption that $\Delta\mathrm{SUVR} = 0$ in a group of healthy controls is rarely valid.

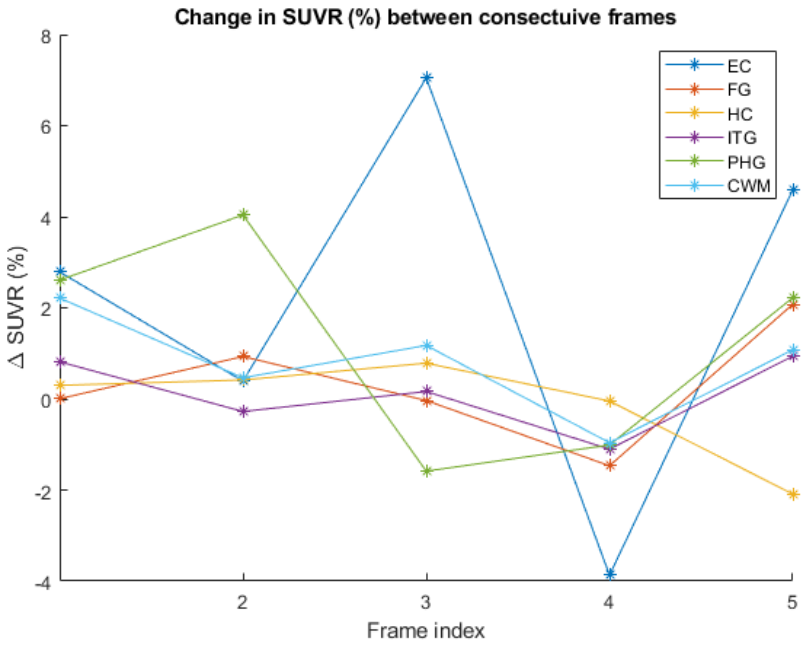

Figure 23: Change of SUVR between consecutive frames of the same scan of a healthy control subject

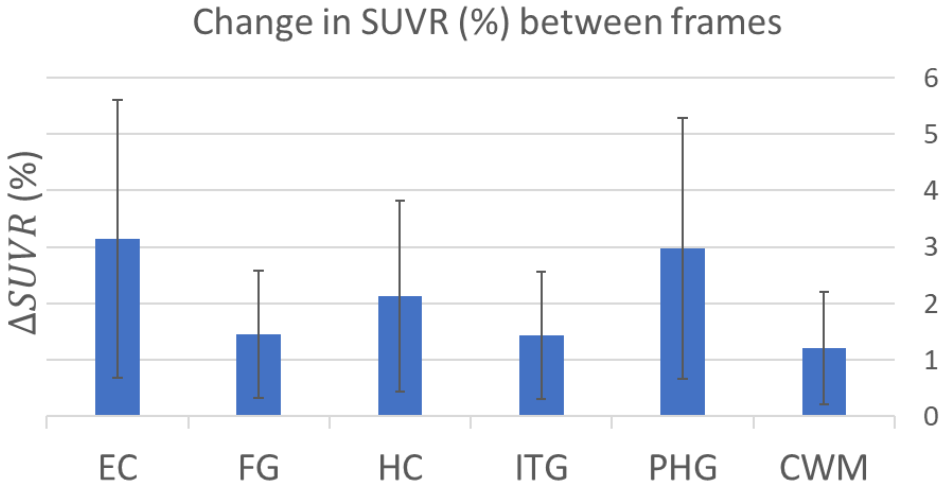

Figure 24: Average change of SUVR between consecutive frames expressed as the percentage of the SUVR in the previous frame

APPENDIX B. Phantom study

We applied the joint reconstruction method on a simulated phantom study. Here we explain how we generated the simulated data that was fed to the proposed method. We compare the obtained results to the conventional methods. We finally report the preliminary results for the model incorporating temporal priors, suggested in CHAPTER 9.

B.1 Phantom simulation

In dynamic PET studies, time activity curves (TAC) show the evolution of the concentration of the radiotracer in a region as a function of time. We have TACs measured for a control subject[135] in different regions of the brain with arterial blood sampling. We fit a MRTM2[136] model to get the kinetic parameters of the tracer, including the distribution volume ratio (DVR). We can now simulate two dynamic PET studies where one region's DVR is increased. Using Montreal Neurologic Institute (MNI) atlas[137] from FSL[138], we can generate a volume where the activity in each region is computed from the PET dynamic studies. An increase in the DVR in one region translates into an increase in the activity in that region. We successfully modeled an increase uptake in tau protein in one region at a second time-point.

We chose to use dynamic data for our simulation because kinetic modelling mimics the physiological process more accurately and therefore yields a more realistic phantom volume. The kinetic parameters for the tracer [^{18}F]-MK-6240 were quantified using a reversible two-tissue compartment model with 4 parameters as it has been found to yield the best fit for the TACs[139]. This precludes the use of Patlak graphical analysis as it is applied to tracers involving an irreversible uptake. We chose the MRTM2 model because

it was used to fit the TACs of the studies acquired at our center[140] as it has been found more accurate than Logan graphical analysis[141].

We created an attenuation map for our phantom using known attenuation factors for bone and water in PET (seen in Section 1.2.3). The simulated activity images and the attenuation map are forward projected using STIR to obtain the projection data for the two simulated time-points and the attenuation coefficients. The normalization factors from a human study scan on the HR+ are used to derive realistic sensitivity coefficients. The number of counts in the simulated projection data is also chosen to reflect the typical count level encountered in a human PET scan. Poisson noise was then added. Scatter and random events were not simulated for this study.

Like with static scans, the cerebellum cortex is used as a reference region. To mimic AD-related tauopathy, the DVR is increased in the hippocampus. Initial estimates from the Harvard Aging Brain Study[118] (HABS) point towards a yearly change of SUVR ranging from 1 to 10%, with MCI subjects exhibiting a higher tau accumulation rate[142]. We simulate a change of 5, 7 and 10% to gauge the joint method's performance in separating between groups exhibiting different rate of tau accumulation. 16 noise realizations are simulated for every contrast level.

We generate the phantom data based on time activity curves in different regions of the brain. We create a first time-point image and then simulate a second time-point with increasing levels of tau accumulation in the hippocampus. Figure 25 shows

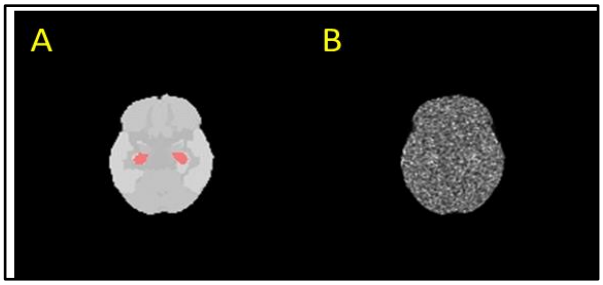

Figure 25: Phantom Simulations. (A) the simulated phantom (noiseless reference image) with the hippocampus mask in red. (B) the simulated image at t_1

(A) the simulated phantom (noiseless reference image) with the overlaid mask for the hippocampus (in red) and (B) the first time-point image.

B.2 Image reconstruction

We generate the difference image using both methods after increasing tau uptake by 10% in the second time-point. We show an example of the obtained difference images in Figure 26: (A) shows the result of the conventional method. (B) shows the jointly reconstructed difference image and the red arrows point to the visible uptake in the hippocampus region.

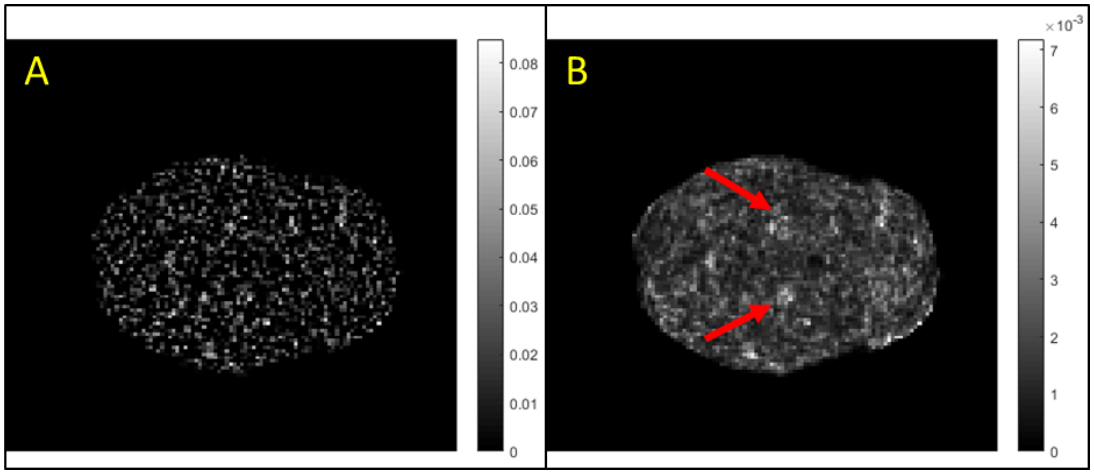

Figure 26: Difference image for a tau accumulation increase of 10%. (A) Conventional method. (B) Proposed method. The red arrows point to the signal detected in the hippocampus region.

We generate 16 noise realizations for three levels of increase in tau accumulation (5, 7, and 10%) to see how the methods perform in separating groups exhibiting different tau accumulation rate. We reconstruct the images using the conventional and the proposed methods and derive the corresponding measures of ΔSUVR in the hippocampus for every noise realization *s*:

$$\Delta\mathrm{SUVR}^{(s)}_{\mathrm{conventional}}(\mathrm{HC}) = \frac{\mathrm{SUVR}_{\mathbf{f_2}}(\mathrm{HC}) - \mathrm{SUVR}_{\mathbf{f_1}}(\mathrm{HC})}{\mathrm{SUVR}_{\mathbf{f_1}}(\mathrm{HC})} \quad (56)$$

For the joint reconstruction, we obtain a difference image $\boldsymbol{\tau}$ and a common image $\boldsymbol{f_{com}}$. We note $\boldsymbol{f_{2_{joint}}} = \boldsymbol{f_{com}} + \boldsymbol{\tau}$, so that we get:

$$\Delta\mathrm{SUVR}^{(s)}_{\mathrm{joint}}(\mathrm{HC}) = \frac{\mathrm{SUVR}_{\mathbf{f_{2_{joint}}}}(\mathrm{HC}) - \mathrm{SUVR}_{\mathbf{f_{com}}}(\mathrm{HC})}{\mathrm{SUVR}_{\mathbf{f_{com}}}(\mathrm{HC})} \quad (57)$$

B.3 Sample size

We compute the mean and the standard deviation of the ΔSUVR across noise realizations for each simulated increased in tau accumulation. The noise realizations represent different subjects and each level of simulated increase represent a specific group. The mean and the standard deviation then characterize artificial groups of subjects exhibiting different levels of tau uptake. They are used to compute a hypothetical sample size for the separation between the simulated groups. We assume a ratio of 5 between the populations: for every 5 subjects with a low tau accumulation rate (reflecting a healthy control), the sample has 1 subject with higher rate (MCI or AD diagnosis). For each method, we estimate the sample size based on two-sample pooled z-test for normally distributed data with equal and known standard deviations. We assume the power of the test to be 90% with a significance level of 5%. The results are reported in Table 7. As expected, the joint reconstruction leads to a smaller sample size.

Method / Groups to separate:	Conventional	Proposed
5% - 10%	13	7
7% - 10%	31	13
5% - 7%	72	34

Table 7: Sample sizes for the separation between groups with different tau accumulations using the two methods

We focus on the separability between the groups with 5% and 7% increase in tau accumulation. We assume here that the normal aging group exhibits 5% of increase in tau accumulation (See APPENDIX A. Typical SUVR change in clinical studies) and we aim to separate them from MCI/AD subjects with a small difference between the groups (around 2% difference). We plot the ROC curve for each method in Figure 27. As shown before with the sample size calculation, the joint method performs better than the direct difference image.

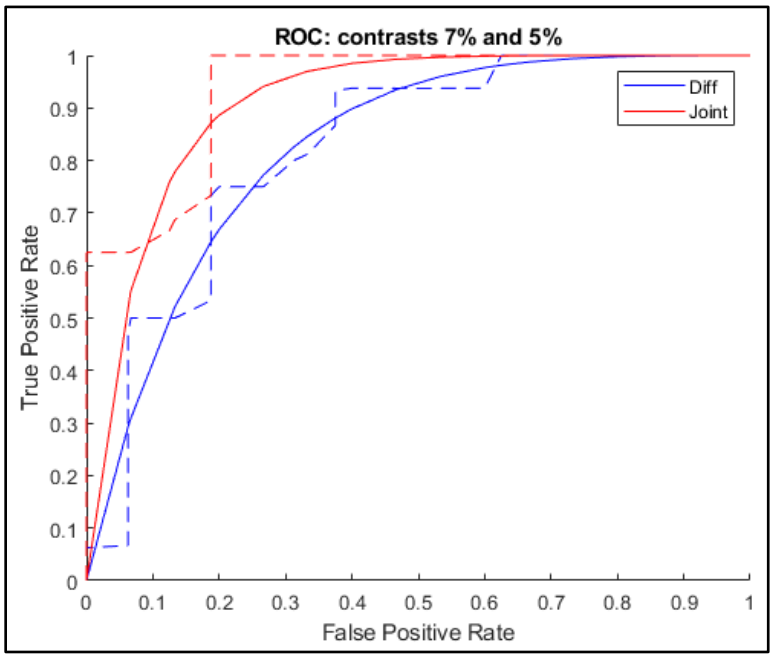

Figure 27: ROC for the separability between the groups with 7% and 5% increase in tau accumulation

B.4 Joint reconstruction with temporal prior

We implemented a BSREM reconstruction to incorporate two priors: the temporal Huber penalty and the structural similarity prior. We simulated 10 noise realizations with an increased DVR of 10% in the thalamus. We reconstructed the phantom images using the conventional method and the joint reconstruction with the two priors and looked at the ΔSUVR in the targeted region. We tested three sets of parameters for each prior reconstruction. We computed the bias and the variance for each method to get the Bias-Variance plot shown in Figure 28. The joint reconstruction incorporating the priors exhibits a lower variance and a similar bias when compared to the conventional method. These results give us confidence in the values of ΔSUVR yielded by the proposed method in subjects images where the real change is unknow and the only available estimate is the one provided by the conventional method.

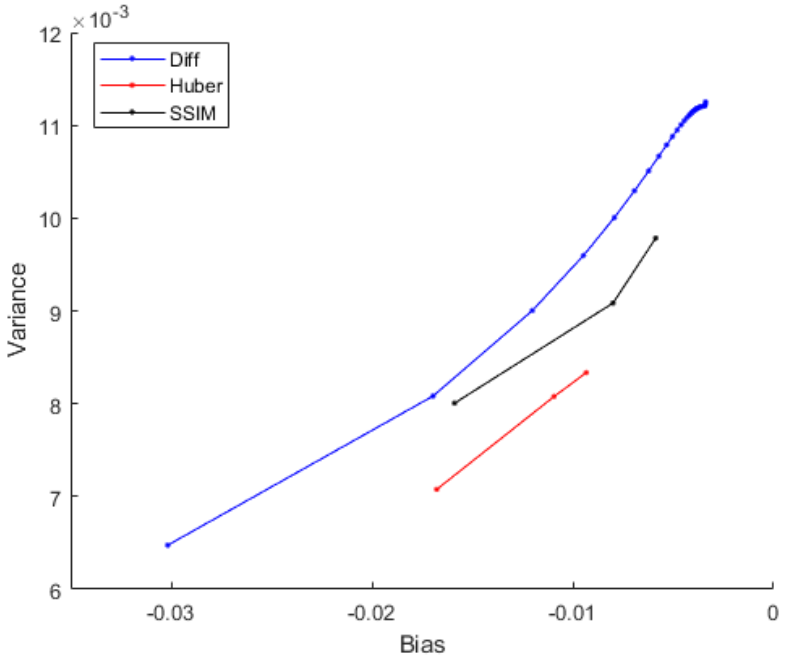

Figure 28: Bias-Variance plot for the joint reconstruction with two different priors compared to the conventional method.

REFERENCES

[1] Alzheimer's Association, "Alzheimer's facts and figures report," Alzheimer's Association. 2019.

[2] T. Jones, "The imaging science of positron emission tomography," European Journal of Nuclear Medicine, vol. 23, no. 7, pp. 807–813, Jul. 1996.

[3] D. Bailey, F. Zito, M.-C. Gilardi, A. Savi, F. Fazio, and T. Jones, "Performance comparison of a state-of-the-art neuro-SPET scanner and a dedicated neuro-PET scanner," European Journal of Nuclear Medicine, vol. 21, no. 5, May 1994.

[4] V. L. Villemagne, V. Doré, P. Bourgeat, S. C. Burnham, S. Laws, O. Salvado, C. L. Masters, and C. C. Rowe, "Aβ-amyloid and tau imaging in dementia," Seminars in Nuclear Medicine, vol. 47, no. 1, pp. 75–88, Jan. 2017.

[5] D. L. Bailey, D. W. Townsend, P. E. Valk, and M. N. Maisey. "Positron Emission Tomography". Springer-Verlag, 2005.

[6] S. R. Cherry, J. Sorenson and M. Phelps. "Physics in Nuclear Medicine". Elsevier, 2012.

[7] R. H. J. A. Slart, J. J. Bax, D. J. van Veldhuisen, E. E. van der Wall, R. Irwan, W. J. Sluiter, R. A. Dierckx, J. de Boer, and P. L. Jager, "Prediction of functional recovery after revascularization in patients with chronic ischaemic left ventricular dysfunction: head-to-head comparison between 99mTc-sestamibi/18F-FDG DISA SPECT and 13N-

ammonia/18F-FDG PET," European Journal of Nuclear Medicine and Molecular Imaging, vol. 33, no. 6, pp. 716–723, Mar. 2006.

[8] S. Capitanio, A. J. Nordin, A. R. Noraini, and C. Rossetti, "PET/CT in nononcological lung diseases: current applications and future perspectives," European Respiratory Review, vol. 25, no. 141, pp. 247–258, Aug. 2016.

[9] V. Berti, L. Mosconi, and A. Pupi, "Brain: normal variations and benign findings in fluorodeoxyglucose-PET/computed tomography imaging," PET Clinics, vol. 9, no. 2, pp. 129–140, Apr. 2014.

[10] J. G. Rajendran, D. C. Wilson, E. U. Conrad, L. M. Peterson, J. D. Bruckner, J. S. Rasey, L. K. Chin, P. D. Hofstrand, J. R. Grierson, J. F. Eary, and K. A. Krohn, "[18F]FMISO and [18F]FDG PET imaging in soft tissue sarcomas: correlation of hypoxia, metabolism and VEGF expression," European Journal of Nuclear Medicine and Molecular Imaging, vol. 30, no. 5, pp. 695–704, Mar. 2003.

[11] S. T. Lee and A. M. Scott, "Hypoxia positron emission tomography imaging with 18F-fluoromisonidazole," Seminars in Nuclear Medicine, vol. 37, no. 6, pp. 451–461, Nov. 2007.

[12] A. Salskov, V. S. Tammisetti, J. Grierson, and H. Vesselle, "FLT: measuring tumor cell proliferation in vivo with positron emission tomography and 3′-deoxy-3′-[18F]fluorothymidine," Seminars in Nuclear Medicine, vol. 37, no. 6, pp. 429–439, Nov. 2007.

[13] S. Mishra, B. A. Gordon, Y. Su, J. Christensen, K. Friedrichsen, K. Jackson, R. Hornbeck, D. A. Balota, N. J. Cairns, J. C. Morris, B. M. Ances, and T. L. S. Benzinger, "AV-1451 PET imaging of tau pathology in preclinical Alzheimer disease: defining a summary measure," NeuroImage, vol. 161, pp. 171–178, Nov. 2017.

[14] M. Picchio and P. Castellucci, "Clinical indications of 11C-Choline PET/CT in prostate cancer patients with biochemical relapse," Theranostics, vol. 2, no. 3, pp. 313–317, 2012.

[15] W. E. Klunk, H. Engler, A. Nordberg, Y. Wang, G. Blomqvist, D. P. Holt, M. Bergström, I. Savitcheva, G.-F. Huang, S. Estrada, B. Ausén, M. L. Debnath, J. Barletta, J. C. Price, J. Sandell, B. J. Lopresti, A. Wall, P. Koivisto, G. Antoni, C. A. Mathis, and B. Långström, "Imaging brain amyloid in Alzheimer's disease with Pittsburgh Compound-B," Annals of Neurology, vol. 55, no. 3, pp. 306–319, Jan. 2004.

[16] R. S. Driessen, P. G. Raijmakers, W. J. Stuijfzand, and P. Knaapen, "Myocardial perfusion imaging with PET," The International Journal of Cardiovascular Imaging, vol. 33, no. 7, pp. 1021–1031, Feb. 2017.

[17] J. Grüner, R. Paamand, L. Højgaard, and I. Law, "Brain perfusion CT compared with 15O-H2O-PET in healthy subjects," EJNMMI Research, vol. 1, no. 1, p. 28, 2011.

[18] M. Conti and L. Eriksson, "Physics of pure and non-pure positron emitters for PET: a review and a discussion," EJNMMI Physics, vol. 3, no. 1, May 2016.

[19] S. DeBenedetti, C. E. Cowan, W. R. Konneker, and H. Primakoff, “On the angular distribution of two-photon annihilation radiation,” Physical Review, vol. 77, no. 2, pp. 205–212, Jan. 1950.

[20] G. F. Knoll. “Radiation Detection and Measurement”. John Wiley & Sons, 2010.

[21] T. K. Lewellen, “Recent developments in PET detector technology,” Physics in Medicine and Biology, vol. 53, no. 17, pp. R287–R317, Aug. 2008.

[22] E. J. Hoffman, S.-C. Huang, M. E. Phelps, and D. E. Kuhl, “Quantitation in positron emission computed tomography,” Journal of Computer Assisted Tomography, vol. 5, no. 3, pp. 391–400, Jun. 1981.

[23] C. W. Stearns, D. L. McDaniel, S. G. Kohlmyer, P. R. Arul, B. P. Geiser, and V. Shanmugam, “Random coincidence estimation from single event rates on the Discovery ST PET/CT scanner,” in 2003 IEEE Nuclear Science Symposium.

[24] D. Brasse, P. E. Kinahan, C. Lartizien, C. Comtat, M. Casey, and C. Michel, “Correction methods for random coincidences in fully 3D whole-body PET: impact on data and image quality,” Journal of Nuclear Medicine, vol. 46, no. 5, pp. 859-867, May 2005.

[25] C. C. Watson, “A technique for measuring the energy response of a PET tomograph using a compact scattering source,” IEEE Transactions on Nuclear Science, vol. 44, no. 6, pp. 2500–2508, 1997.

[26] J. M. Ollinger, “Model-based scatter correction for fully 3D PET,” Physics in Medicine and Biology, vol. 41, no. 1, pp. 153–176, Jan. 1996.

[27] G. K. von Schulthess, H. C. Steinert, and T. F. Hany, “Integrated PET/CT: current applications and future directions,” Radiology, vol. 238, no. 2, pp. 405–422, Feb. 2006.

[28] C. Burger, G. Goerres, S. Schoenes, A. Buck, A. Lonn, and G. von Schulthess, “PET attenuation coefficients from CT images: experimental evaluation of the transformation of CT into PET 511-keV attenuation coefficients,” European Journal of Nuclear Medicine and Molecular Imaging, vol. 29, no. 7, pp. 922–927, Apr. 2002.

[29] R. D. Badawi, N. C. Ferreira, S. G. Kohlmyer, M. Dahlbom, P. K. Marsden, and T. K. Lewellen, “A comparison of normalization effects on three whole-body cylindrical 3D PET systems,” Physics in Medicine and Biology, vol. 45, no. 11, pp. 3253–3266, Oct. 2000.

[30] H. M. Hudson and R. S. Larkin, “Accelerated image reconstruction using ordered subsets of projection data,” IEEE Transactions on Medical Imaging, vol. 13, no. 4, pp. 601–609, 1994.

[31] L. A. Shepp and Y. Vardi, “Maximum likelihood reconstruction for emission tomography,” IEEE Transactions on Medical Imaging, vol. 1, no. 2, pp. 113–122, Oct. 1982.

[32] A. P. Dempster, N. M. Laird, and D. B. Rubin, “Maximum likelihood from incomplete data via the EM algorithm,” Journal of the Royal Statistical Society: Series B (Methodological), vol. 39, no. 1, pp. 1–22, Sep. 1977.

[33] I.-T. Hsiao, A. Rangarajan, P. Khurd, and G. Gindi, “An accelerated convergent ordered subsets algorithm for emission tomography,” Physics in Medicine and Biology, vol. 49, no. 11, pp. 2145–2156, May 2004.

[34] A. K. Buck, K. Herrmann, T. Stargardt, T. Dechow, B. J. Krause, and J. Schreyogg, “Economic evaluation of PET and PET/CT in oncology: evidence and methodologic approaches,” Journal of Nuclear Medicine, vol. 51, no. 3, pp. 401–412, Feb. 2010.

[35] T. Jones and D. Townsend, “History and future technical innovation in positron emission tomography,” Journal of Medical Imaging, vol. 4, no. 1, p. 11013, Mar. 2017.

[36] W. A. Weber, “Positron emission tomography as an imaging biomarker,” Journal of Clinical Oncology, vol. 24, no. 20, pp. 3282–3292, Jul. 2006.

[37] R. J. H. M. Steenbakkers, J. C. Duppen, I. Fitton, K. E. I. Deurloo, L. J. Zijp, E. F. I. Comans, A. L. J. Uitterhoeve, P. T. R. Rodrigus, G. W. P. Kramer, J. Bussink, K. De Jaeger, J. S. A. Belderbos, P. J. C. M. Nowak, M. van Herk, and C. R. N. Rasch, “Reduction of observer variation using matched CT-PET for lung cancer delineation: A three-dimensional analysis,” International Journal of Radiation Oncology • Biology • Physics, vol. 64, no. 2, pp. 435–448, Feb. 2006.

[38] T. H. Schindler, H. R. Schelbert, A. Quercioli, and V. Dilsizian, “Cardiac PET imaging for the detection and monitoring of coronary artery disease and microvascular health,” JACC: Cardiovascular Imaging, vol. 3, no. 6, pp. 623–640, Jun. 2010.

[39] M. Bruehlmeier, U. Roelcke, P. A. Schubiger, and S. M. Ametamey, “Assessment of hypoxia and perfusion in human brain tumors using PET with 18F-fluoromisonidazole and 15O-H2O,” Journal of Nuclear Medicine, vol. 45, no. 11, pp. 1851-1859, Nov. 2004.

[40] W. Chen, T. Cloughesy, N. Kamdar, N. Satyamurthy, M. Bergsneider, L. Liau, P. Mischel, J. Czernin, M. E. Phelps, and D. H.S. Silverman, “Imaging proliferation in brain tumors with 18F-FLT PET: comparison with 18F-FDG,” Journal of Nuclear Medicine, vol. 46, no. 6, pp. 945-952, Jun. 2005.

[41] M. V. Padma, S. Said, M. Jacobs, D. R. Hwang, K. Dunigan, M. Satter, B. Christian, J. Ruppert, T. Bernstein, G. Kraus, and J. C. Mantil, “Prediction of pathology and survival by FDG PET in gliomas,” Journal of Neuro-Oncology, vol. 64, no. 3, pp. 227–237, Sep. 2003.

[42] S. Hwang, J. H. Kim, S. W. Park, M. H. Han, I. K. Yu, S. H. Lee, D. S. Lee, S. K. Lee, C. Chung and K. Chang, “Comparative analysis of MR imaging, positron emission tomography, and ictal single-photon emission CT in patients with neocortical epilepsy,” American Journal of Neuroradiology, vol. 22, no. 5, pp. 937-946, May 2001.

[43] F. Chassoux, S. Rodrigo, F. Semah, F. Beuvon, E. Landre, B. Devaux, B. Turak, C. Mellerio, J.-F. Meder, F.-X. Roux, C. Daumas-Duport, P. Merlet, O. Dulac, and C. Chiron, “FDG-PET improves surgical outcome in negative MRI Taylor-type focal cortical dysplasias,” Neurology, vol. 75, no. 24, pp. 2168–2175, Dec. 2010.

[44] G. M. McKhann, D. S. Knopman, H. Chertkow, B. T. Hyman, C. R. Jack Jr., C. H. Kawas, W. E. Klunk, W. J. Koroshetz, J. J. Manly, R. Mayeux, R. C. Mohs, J. C. Morris,

M. N. Rossor, P. Scheltens, M. C. Carrillo, B. Thies, S. Weintraub, and C. H. Phelps, “The diagnosis of dementia due to Alzheimer’s disease: recommendations from the National Institute on Aging-Alzheimer’s Association workgroups on diagnostic guidelines for Alzheimer’s disease,” Alzheimer’s & Dementia, vol. 7, no. 3, pp. 263–269, May 2011.

[45] V. K. N. Shivamurthy, A. K. Tahari, C. Marcus, and R. M. Subramaniam, “Brain FDG PET and the diagnosis of dementia,” American Journal of Roentgenology, vol. 204, no. 1, pp. W76–W85, Jan. 2015.

[46] R. A. Stelzmann, H. Norman Schnitzlein, and F. Reed Murtagh, “An English translation of Alzheimer’s 1907 paper, “Über eine eigenartige Erkankung der Hirnrinde”,” Clinical Anatomy, vol. 8, no. 6, pp. 429–431, 1995.

[47] D. A. Drachman, “Aging of the brain, entropy, and Alzheimer disease,” Neurology, vol. 67, no. 8, pp. 1340–1352, Oct. 2006.

[48] [Editorial] “The three stages of Alzheimer’s disease,” The Lancet, vol. 377, no. 9776, p. 1465, Apr. 2011.

[49] E. Tulving and H. J. Markowitsch, “Episodic and declarative memory: role of the hippocampus,” Hippocampus, vol. 8, no. 3, pp. 198–204, 1998.

[50] Y. Mu and F. H. Gage, “Adult hippocampal neurogenesis and its role in Alzheimer’s disease,” Molecular Neurodegeneration, vol. 6, no. 1, p. 85, 2011.

[51] J. A. Yesavage, J. O. Brooks, J. Taylor, and J. Tinklenberg, “Development of aphasia, apraxia, and agnosia and decline in Alzheimer’s disease,” American Journal of Psychiatry, vol. 150, no. 5, pp. 742–747, May 1993.

[52] C. Christie, D. Martinez, M. Roca, S. O`Neill, J. Bustin, P. Richly, and F. Manes, “Apraxia as initial presentation of Alzheimer’s disease: a case series,” Alzheimer’s & Dementia, vol. 9, no. 4, pp. P751–P752, Jul. 2013.

[53] N. Tsuno and A. Homma, “What is the association between depression and Alzheimer’s disease?,” Expert Review of Neurotherapeutics, vol. 9, no. 11, pp. 1667–1676, Nov. 2009.

[54] L. Teri, L. E. Ferretti, L. E. Gibbons, R. G. Logsdon, S. M. McCurry, W. A. Kukull, W. C. McCormick, J. D. Bowen, and E. B. Larson, “Anxiety in Alzheimer’s disease: prevalence and comorbidity,” The Journals of Gerontology Series A: Biological Sciences and Medical Sciences, vol. 54, no. 7, pp. M348–M352, Jul. 1999.

[55] F. Margari, M. Sicolo, L. Spinelli, F. Mastroianni, A. Pastore, F. Craig and M. G. Petruzzelli, “Aggressive behavior, cognitive impairment, and depressive symptoms in elderly subjects,” Neuropsychiatric Disease and Treatment, p. 347, Aug. 2012.

[56] V. Senanarong, J. L. Cummings, L. Fairbanks, M. Mega, D. M. Masterman, S. M. O’Connor, and T. L. Strickland, “Agitation in Alzheimer’s disease is a manifestation of frontal lobe dysfunction,” Dementia and Geriatric Cognitive Disorders, vol. 17, no. 1–2, pp. 14–20, 2004.

[57] M. S. Mega, J. L. Cummings, T. Fiorello, and J. Gornbein, “The spectrum of behavioral changes in Alzheimer’s disease,” Neurology, vol. 46, no. 1, pp. 130–135, Jan. 1996.

[58] C. P. Ferri, M. Prince, C. Brayne, H. Brodaty, L. Fratiglioni, M. Ganguli, K. Hall, K. Hasegawa, H. Hendrie, Y. Huang, A. Jorm, C. Mathers, P. R. Menezes, E. Rimmer, and M. Scazufca, “Global prevalence of dementia: a Delphi consensus study,” The Lancet, vol. 366, no. 9503, pp. 2112–2117, Dec. 2005.

[59] P. T. Nelson, D. W. Dickson, J. Q. Trojanowski, C. R. Jack, P. A. Boyle, K. Arfanakis, R. Rademakers, I. Alafuzoff, J. Attems, C. Brayne, I. T. S. Coyle-Gilchrist, H. C. Chui, D. W. Fardo, M. E. Flanagan, G. Halliday, S. R. K. Hokkanen, S. Hunter, G. A. Jicha, Y. Katsumata, C. H. Kawas, C. D. Keene, G. G. Kovacs, W. A. Kukull, A. I. Levey, N. Makkinejad, T. J. Montine, S. Murayama, M. E. Murray, S. Nag, R. A. Rissman, W. W. Seeley, R. A. Sperling, C. L. White III, L. Yu, and J. A. Schneider, “Limbic-predominant age-related TDP-43 encephalopathy (LATE): consensus working group report,” Brain, vol. 142, no. 6, pp. 1503–1527, Apr. 2019.

[60] J. Lindsay, D. Laurin, R. Verreault, R. Hébert, B. Helliwell, G. B. Hill and I. McDowell, “Risk factors for Alzheimer’s disease: a prospective analysis from the Canadian study of health and aging,” American Journal of Epidemiology, vol. 156, no. 5, pp. 445–453, Sep. 2002.

[61] M. Kivipelto, T. Ngandu, L. Fratiglioni, M. Viitanen, I. Kåreholt, B. Winblad, E.-L. Helkala, J. Tuomilehto, H. Soininen, and A. Nissinen, “Obesity and vascular risk factors

at midlife and the risk of dementia and Alzheimer disease," Archives of Neurology, vol. 62, no. 10, Oct. 2005.

[62] Z. Arvanitakis, R. S. Wilson, J. L. Bienias, D. A. Evans, and D. A. Bennett, "Diabetes mellitus and risk of Alzheimer disease and decline in cognitive function," Archives of Neurology, vol. 61, no. 5, p. 661, May 2004.

[63] R. S. Wilson, K. R. Krueger, S. E. Arnold, J. A. Schneider, J. F. Kelly, L. L. Barnes, Y. Tang, and D. A. Bennett, "Loneliness and risk of Alzheimer disease," Archives of General Psychiatry, vol. 64, no. 2, p. 234, Feb. 2007.

[64] Q. Jiang, C. Y. D. Lee, S. Mandrekar, B. Wilkinson, P. Cramer, N. Zelcer, K. Mann, B. Lamb, T. M. Willson, J. L. Collins, J. C. Richardson, J. D. Smith, T. A. Comery, D. Riddell, D. M. Holtzman, P. Tontonoz, and G. E. Landreth, "ApoE promotes the proteolytic degradation of Aβ," Neuron, vol. 58, no. 5, pp. 681–693, Jun. 2008.

[65] C. Graf, "The Lawton instrumental activities of daily living scale," AJN, American Journal of Nursing, vol. 108, no. 4, pp. 52–62, Apr. 2008.

[66] Z. S. Nasreddine, N. A. Phillips, V. Bédirian, S. Charbonneau, V. Whitehead, I. Collin, J. L. Cummings, and H. Chertkow, "The Montreal Cognitive Assessment, MoCA: a brief screening tool for mild cognitive impairment," Journal of the American Geriatrics Society, vol. 53, no. 4, pp. 695–699, Apr. 2005.

[67] J. C. Morris, "The Clinical Dementia Rating (CDR): current version and scoring rules," Neurology, vol. 43, no. 11, pp. 2412–2412, Nov. 1993.

[68] T. N. Tombaugh and N. J. McIntyre, “The mini-mental state examination: a comprehensive review,” Journal of the American Geriatrics Society, vol. 40, no. 9, pp. 922–935, Sep. 1992.

[69] M. N. Braskie and P. M. Thompson, “A focus on structural brain imaging in the Alzheimer’s disease neuroimaging initiative,” Biological Psychiatry, vol. 75, no. 7, pp. 527–533, Apr. 2014.

[70] [Editorial] “Consensus Recommendations for the Postmortem Diagnosis of Alzheimer’s Disease,” Neurobiology of Aging, vol. 18, no. 4, pp. S1–S2, Jul. 1997.

[71] H. Braak and E. Braak, “Neuropathological staging of Alzheimer-related changes,” Acta Neuropathologica, vol. 82, no. 4, pp. 239–259, Sep. 1991.

[72] R. Craig-Schapiro, A. M. Fagan, and D. M. Holtzman, “Biomarkers of Alzheimer’s disease,” Neurobiology of Disease, vol. 35, no. 2, pp. 128–140, Aug. 2009.

[73] C. Haass and D. J. Selkoe, “Soluble protein oligomers in neurodegeneration: lessons from the Alzheimer’s amyloid β-peptide,” Nature Reviews Molecular Cell Biology, vol. 8, no. 2, pp. 101–112, Feb. 2007.

[74] J. Hardy and D. J. Selkoe, “The amyloid hypothesis of Alzheimer’s disease: progress and problems on the road to therapeutics,” Science, vol. 297, no. 5580, pp. 353–356, Jul. 2002.

[75] J. P. Brion, A. M. Couck, E. Passareiro, and J. Flament-Durand, “Neurofibrillary tangles of Alzheimer’s disease: an immunohistochemical study,” Journal of Submicroscopic Cytology, vol. 17, no. 1, pp. 89-96, Jan. 1985.

[76] L. Buée, T. Bussière, V. Buée-Scherrer, A. Delacourte, and P. R. Hof, “Tau protein isoforms, phosphorylation and role in neurodegenerative disorders,” Brain Research Reviews, vol. 33, no. 1, pp. 95–130, Aug. 2000.

[77] T. F. Gendron and L. Petrucelli, “The role of tau in neurodegeneration,” Molecular Neurodegeneration, vol. 4, no. 1, p. 13, 2009.

[78] E. Giacobini and G. Gold, “Alzheimer disease therapy—moving from amyloid-β to tau,” Nature Reviews Neurology, vol. 9, no. 12, pp. 677–686, Nov. 2013.

[79] K. A. Johnson, A. Schultz, R. A. Betensky, J. A. Becker, J. Sepulcre, D. Rentz, E. Mormino, J. Chhatwal, R. Amariglio, K. Papp, G. Marshall, M. Albers, S. Mauro, L. Pepin, J. Alverio, K. Judge, M. Philiossaint, T. Shoup, D. Yokell, B. Dickerson, T. Gomez-Isla, B. Hyman, N. Vasdev, and R. Sperling, “Tau positron emission tomographic imaging in aging and early Alzheimer disease,” Annals of Neurology, vol. 79, no. 1, pp. 110–119, Dec. 2015.

[80] H. Braak, I. Alafuzoff, T. Arzberger, H. Kretzschmar, and K. Del Tredici, “Staging of Alzheimer disease-associated neurofibrillary pathology using paraffin sections and immunocytochemistry,” Acta Neuropathologica, vol. 112, no. 4, pp. 389–404, Aug. 2006.

[81] H. Braak, D. R. Thal, E. Ghebremedhin, and K. Del Tredici, “Stages of the pathologic process in Alzheimer pisease: age categories from 1 to 100 years,” Journal of Neuropathology & Experimental Neurology, vol. 70, no. 11, pp. 960–969, Nov. 2011.

[82] M. Farlow, R. Anand, J. Messina Jr, R. Hartman, and J. Veach, “A 52-week study of the efficacy of rivastigmine in patients with mild to moderately severe Alzheimer’s disease,” European Neurology, vol. 44, no. 4, pp. 236–241, 2000.

[83] V. L. Villemagne, M. T. Fodero-Tavoletti, C. L. Masters, and C. C. Rowe, “Tau imaging: early progress and future directions,” The Lancet Neurology, vol. 14, no. 1, pp. 114–124, Jan. 2015.

[84] L. M. Smid, V. Kepe, H. V. Vinters, M. Bresjanac, T. Toyokuni, N. Satyamurthy, K. Wong, S. Huang, D. H.S. Silverman, K. Miller, G. W. Small, and J. R. Barrio, “Postmortem 3-D brain hemisphere cortical tau and amyloid-β pathology mapping and quantification as a validation method of neuropathology imaging,” Journal of Alzheimer’s Disease, vol. 36, no. 2, pp. 261–274, Jun. 2013.

[85] V. L. Villemagne, S. Furumoto, M. T. Fodero-Tavoletti, R. S. Mulligan, J. Hodges, R. Harada, P. Yates, O. Piguet, S. Pejoska, V. Doré, K. Yanai, C. L. Masters, Y. Kudo, C. C. Rowe, and N. Okamura, “In vivo evaluation of a novel tau imaging tracer for Alzheimer’s disease,” European Journal of Nuclear Medicine and Molecular Imaging, vol. 41, no. 5, pp. 816–826, Feb. 2014.

[86] N. Okamura, S. Furumoto, R. Harada, T. Tago, T. Yoshikawa, M. Fodero-Tavoletti, R. S. Mulligan, V. L. Villemagne, H. Akatsu, T. Yamamoto, H. Arai, R. Iwata,

K. Yanai, and Y. Kudo, “Novel 18F-labeled arylquinoline derivatives for noninvasive imaging of tau pathology in Alzheimer disease,” Journal of Nuclear Medicine, vol. 54, no. 8, pp. 1420–1427, Jul. 2013.

[87] R. Harada, S. Furumoto, T. Tago, F. Katsutoshi, A. Ishiki, N. Tomita, R. Iwata, M. Tashiro, H. Arai, K. Yanai, Y. Kudo, and N. Okamura, “Characterization of the radiolabeled metabolite of tau PET tracer 18F-THK5351,” European Journal of Nuclear Medicine and Molecular Imaging, vol. 43, no. 12, pp. 2211–2218, Jul. 2016.

[88] C.-F. Xia, J. Arteaga, G. Chen, U. Gangadharmath, L. F. Gomez, D. Kasi, C. Lam, Q. Liang, C. Liu, V. P. Mocharla, F. Mu, A. Sinha, H. Su, A. K. Szardenings, J. C. Walsh, E. Wang, C. Yu, W. Zhang, T. Zhao, and H. C. Kolb, “[18F]T807, a novel tau positron emission tomography imaging agent for Alzheimer’s disease,” Alzheimer’s & Dementia, vol. 9, no. 6, pp. 666–676, Nov. 2013.

[89] A. J. Schwarz, P. Yu, B. B. Miller, S. Shcherbinin, J. Dickson, M. Navitsky, A. D. Joshi, M. D. Devous Sr, and M. S. Mintun, “Regional profiles of the candidate tau PET ligand 18F-AV-1451 recapitulate key features of Braak histopathological stages,” Brain, vol. 139, no. 5, pp. 1539–1550, Mar. 2016.

[90] D. T. Chien, S. Bahri, A. K. Szardenings, J. C. Walsh, F. Mu, M. Su, W. R. Shankle, A. Elizarov, and H. C. Kolb, “Early clinical PET imaging results with the novel PHF-tau radioligand [18F]-T807,” Journal of Alzheimer’s Disease, vol. 34, no. 2, pp. 457–468, Jun. 2013.

[91] S. Shcherbinin, A. J. Schwarz, A. Joshi, M. Navitsky, M. Flitter, W. R. Shankle, M. D. Devous, and M. A. Mintun, “Kinetics of the tau PET tracer 18F-AV-1451 (T807) in subjects with normal cognitive function, mild cognitive impairment, and Alzheimer disease,” Journal of Nuclear Medicine, vol. 57, no. 10, pp. 1535–1542, May 2016.

[92] O. Barret, D. Alagille, S. Sanabria, R. A. Comley, R. M. Weimer, E. Borroni, M. Mintun, N. Seneca, C. Papin, T. Morley, K. Marek, J. P. Seibyl, G. D. Tamagnan, and D. Jennings, “Kinetic modeling of the tau PET tracer 18F-AV-1451 in human healthy volunteers and Alzheimer disease subjects,” Journal of Nuclear Medicine, vol. 58, no. 7, pp. 1124–1131, Dec. 2016.

[93] S. Ellis and A. J. Reader, “Simultaneous maximum a posteriori longitudinal PET image reconstruction,” Physics in Medicine & Biology, vol. 62, no. 17, pp. 6963–6979, Aug. 2017.

[94] P. J. Green, “On use of the EM algorithm for penalized likelihood estimation,” Journal of the Royal Statistical Society: Series B (Methodological), vol. 52, no. 3, pp. 443–452, Jul. 1990.

[95] S. Somayajula, C. Panagiotou, A. Rangarajan, Q. Li, S. R. Arridge, and R. M. Leahy, “PET image reconstruction using information theoretic anatomical priors,” IEEE Transactions on Medical Imaging, vol. 30, no. 3, pp. 537–549, Mar. 2011.

[96] V. Y. Panin, G. L. Zeng, and G. T. Gullberg, “Total variation regulated EM algorithm [SPECT reconstruction],” IEEE Transactions on Nuclear Science, vol. 46, no. 6, pp. 2202–2210, 1999.

[97] S. Ellis and A. J. Reader, “Penalized maximum likelihood simultaneous longitudinal PET image reconstruction with difference-image priors,” Medical Physics, vol. 45, no. 7, pp. 3001–3018, May 2018.

[98] X. Lai, Y. Petibon, G. El Fakhri, and J. Ouyang, “Joint reconstruction of rest/stress myocardial perfusion SPECT,” Physics in Medicine & Biology, vol. 63, no. 13, p. 135019, Jul. 2018.

[99] Y. Rakvongthai, F. Fahey, K. Borvorntanajanya, S. Tepmongkol, U. Vutrapongwatana, K. Zukotynski, G. El Fakhri, and J. Ouyang, “Joint reconstruction of ictal/inter-ictal SPECT data for improved epileptic foci localization,” Medical Physics, vol. 44, no. 4, pp. 1437–1444, Apr. 2017.

[100] M. Schöll, S. N. Lockhart, D. R. Schonhaut, J. P. O’Neil, M. Janabi, R. Ossenkoppele, S. L. Baker, J. W. Vogel, J. Faria, H. D. Schwimmer, G. D. Rabinovici, and W. J. Jagust, “PET imaging of tau deposition in the aging human brain,” Neuron, vol. 89, no. 5, pp. 971–982, Mar. 2016.

[101] H. Cramér. “Mathematical Methods of Statistics”. Princeton University Press, 1999.

[102] T.-T. Lu and S.-H. Shiou, “Inverses of 2 × 2 block matrices,” Computers & Mathematics with Applications, vol. 43, no. 1–2, pp. 119–129, Jan. 2002.

[103] H. V. Henderson and S. R. Searle, “On deriving the inverse of a sum of matrices,” SIAM Review, vol. 23, no. 1, pp. 53–60, Jan. 1981.

[104] C. Cloquet and M. Defrise, “MLEM and OSEM deviate from the Cramer-Rao bound at low counts,” IEEE Transactions on Nuclear Science, vol. 60, no. 1, pp. 134–143, Feb. 2013.

[105] B. Fischl, “FreeSurfer,” NeuroImage, vol. 62, no. 2, pp. 774–781, Aug. 2012.

[106] D. L. G. Hill, P. G. Batchelor, M. Holden, and D. J. Hawkes, “Medical image registration,” Physics in Medicine and Biology, vol. 46, no. 3, pp. R1–R45, Feb. 2001.

[107] J. Ashburner and K. Friston, “Rigid Body Registration,” in Human Brain Function, Elsevier, 2004, pp. 635–653.

[108] J. P. W. Pluim, J. B. A. Maintz, and M. A. Viergever, “Mutual-information-based registration of medical images: a survey,” IEEE Transactions on Medical Imaging, vol. 22, no. 8, pp. 986–1004, Aug. 2003.

[109] T. M. Cover and J. A. Thomas. “Elements of Information Theory”. Wiley-Interscience, 1991.

[110] Mathworks, “MATLAB”, 2019.

[111] D.-J. Kroon and C. H. Slump, “MRI modalitiy transformation in demon registration,” in 2009 IEEE International Symposium on Biomedical Imaging: From Nano to Macro, 2009.

[112] L.-E. Adam, J. Zaers, H. Ostertag, H. Trojan, M. E. Bellemann, and G. Brix, “Performance evaluation of the whole-body PET scanner ECAT EXACT HR+ following

the IEC standard," IEEE Transactions on Nuclear Science, vol. 44, no. 3, pp. 1172–1179, Jun. 1997.

[113] M. E. Casey, H. Gadagkar and D. Newport, "A component based method for normalization in volume PET," in 1995 Proceedings of third International Meeting on Fully Three-dimensional Image Reconstruction in Radiology and Nuclear Medicine, 1995.

[114] K. Thielemans, C. Tsoumpas, S. Mustafovic, T. Beisel, P. Aguiar, N. Dikaios, and M. W. Jacobson, "STIR: software for tomographic image reconstruction release 2," Physics in Medicine and Biology, vol. 57, no. 4, pp. 867–883, Jan. 2012.

[115] I. Polycarpou, K. Thielemans, R. Manjeshwar, P. Aguiar, P. K. Marsden, and C. Tsoumpas, "Comparative evaluation of scatter correction in 3D PET using different scatter-level approximations," Annals of Nuclear Medicine, vol. 25, no. 9, pp. 643–649, Jul. 2011.

[116] J. Qi, R. M. Leahy, C. Hsu, T. H. Farquhar, and S. R. Cherry, "Fully 3D Bayesian image reconstruction for the ECAT EXACT HR+," IEEE Transactions on Nuclear Science, vol. 45, no. 3, pp. 1096–1103, Jun. 1998.

[117] M. Yavuz and J. A. Fessler, "Statistical image reconstruction methods for randoms-precorrected PET scans," Medical Image Analysis, vol. 2, no. 4, pp. 369–378, Dec. 1998.

[118] A. Dagley, M. LaPoint, W. Huijbers, T. Hedden, D. G. McLaren, J. P. Chatwal, K. V. Papp, R. E. Amariglio, D. Blacker, D. M. Rentz, K. A. Johnson, R. A. Sperling, and A. P. Schultz, "Harvard Aging Brain Study: Dataset and accessibility," NeuroImage, vol. 144, pp. 255–258, Jan. 2017.

[119] T. G. Fong, M. A. Fearing, R. N. Jones, P. Shi, E. R. Marcantonio, J. L. Rudolph, F. M. Yang, D. K. Kiely, and S. K. Inouye, “Telephone Interview for Cognitive Status: Creating a crosswalk with the Mini-Mental State Examination,” Alzheimer’s & Dementia, vol. 5, no. 6, pp. 492–497, Nov. 2009.

[120] J. P. Mugler and J. R. Brookeman, “Three-dimensional magnetization-prepared rapid gradient-echo imaging (3D MP RAGE),” Magnetic Resonance in Medicine, vol. 15, no. 1, pp. 152–157, Jul. 1990.

[121] J. Wonderlick, D. Ziegler, P. Hosseini-Varnamkhasti, J. Locascio, A. Bakkour, A. Vanderkouwe, C. Triantafyllou, S. Corkin, and B. Dickerson, “Reliability of MRI-derived cortical and subcortical morphometric measures: Effects of pulse sequence, voxel geometry, and parallel imaging,” NeuroImage, vol. 44, no. 4, pp. 1324–1333, Feb. 2009.

[122] N. A. Macmillan and C. D. Creelman. “Detection Theory”. Psychology Press, 2004.

[123] J. Tukey. “Exploratory Data Analysis”. Addison-Wesely Publishers, 1977.

[124] W. Peterson, T. Birdsall, and W. Fox, “The theory of signal detectability,” Transactions of the IRE Professional Group on Information Theory, vol. 4, no. 4, pp. 171–212, Sep. 1954.

[125] R. Bernard. “Fundamentals of Biostatistics”. PWS Publishers, 2000.

[126] M. D. Devous, A. D. Joshi, M. Navitsky, S. Southekal, M. J. Pontecorvo, H. Shen, M. Lu, W. R. Shankle, J. P. Seibyl, K. Marek, and M. A. Mintun, “Test–retest

reproducibility for the tau PET imaging agent 18F-flortaucipir," Journal of Nuclear Medicine, vol. 59, no. 6, pp. 937–943, Dec. 2017.

[127] C. R. Jack Jr, H. J. Wiste, C. G. Schwarz, V. J. Lowe, M. L. Senjem, P. Vemuri, S. D. Weigand, T. M. Therneau, D. S. Knopman, J. L. Gunter, D. T. Jones, J. Graff-Radford, K. Kantarci, R. O. Roberts, M. M. Mielke, M. M. Machulda, and R. C. Petersen, "Longitudinal tau PET in ageing and Alzheimer's disease," Brain, vol. 141, no. 5, pp. 1517–1528, Mar. 2018.

[128] J. Nuyts, S. Stroobants, P. Dupont, S. Vleugels, P. Flamen, and L. Mortelmans, "Reducing loss of image quality because of the attenuation artifact in uncorrected PET whole-body images," Journal of Nuclear Medicine, vol. 43, no. 8, pp. 1054-1062, Aug. 2002.

[129] C. Byrne, "Iterative algorithms for deblurring and deconvolution with constraints," Inverse Problems, vol. 14, no. 6, pp. 1455–1467, Dec. 1998.

[130] K. Van Slambrouck, S. Stute, C. Comtat, M. Sibomana, F. H. P. van Velden, R. Boellaard, and J. Nuyts, "Bias reduction for low-statistics PET: maximum likelihood reconstruction with a modified Poisson distribution," IEEE Transactions on Medical Imaging, vol. 34, no. 1, pp. 126–136, Jan. 2015.

[131] S. Ahn and J. A. Fessler, "Globally convergent image reconstruction for emission tomography using relaxed ordered subsets algorithms," IEEE Transactions on Medical Imaging, vol. 22, no. 5, pp. 613–626, May 2003.

[132] P. J. Huber, “Robust estimation of a location parameter,” The Annals of Mathematical Statistics, vol. 35, no. 1, pp. 73–101, Mar. 1964.

[133] Z. Wang, A. C. Bovik, H. R. Sheikh, and E. P. Simoncelli, “Image Quality Assessment: From Error Visibility to Structural Similarity,” IEEE Transactions on Image Processing, vol. 13, no. 4, pp. 600–612, Apr. 2004.

[134] J. R. Barrio, “The Irony of PET Tau Probe Specificity,” Journal of Nuclear Medicine, vol. 59, no. 1, pp. 115–116, Nov. 2017.

[135] D. W. Wooten, N. J. Guehl, E. E. Verwer, T. M. Shoup, D. L. Yokell, N. Zubcevik, N. Vasdev, R. D. Zafonte, K. A. Johnson, G. El Fakhri, and M. D. Normandin, “Pharmacokinetic evaluation of the tau PET radiotracer 18F-T807 (18F-AV-1451) in human subjects,” Journal of Nuclear Medicine, vol. 58, no. 3, pp. 484–491, Sep. 2016.

[136] M. Ichise, J.-S. Liow, J.-Q. Lu, A. Takano, K. Model, H. Toyama, T. Suhara, K. Suzuki, R. B. Innis, and R. E. Carson, “Linearized reference tissue parametric imaging methods: application to [11C]DASB positron emission tomography studies of the serotonin transporter in human brain,” Journal of Cerebral Blood Flow & Metabolism, vol. 23, no. 9, pp. 1096–1112, Sep. 2003.

[137] G. Grabner, A. L. Janke, M. M. Budge, D. Smith, J. Pruessner, and D. L. Collins, “Symmetric atlasing and model based segmentation: an application to the hippocampus in older adults,” in Medical Image Computing and Computer-Assisted Intervention – MICCAI 2006, Springer Berlin Heidelberg, 2006, pp. 58–66.

[138] FSL, “FMRIB Software Library,” University of Oxford, 2006.

[139] T. A. Pascoal, M. Shin, M. S. Kang, M. Chamoun, D. Chartrand, S. Mathotaarachchi, I. Bennacef, J. Therriault, K. P. Ng, R. Hopewell, R. Bouhachi, H.-H. Hsiao, A. L. Benedet, J.-P. Soucy, G. Massarweh, S. Gauthier, and P. Rosa-Neto, "In vivo quantification of neurofibrillary tangles with [18F] MK-6240," Alzheimer's Research & Therapy, vol. 10, no. 1, Jul. 2018.

[140] N. J. Guehl, D. W. Wooten, D. L. Yokell, S.-H. Moon, M. Dhaynaut, S. Katz, K. A. Moody, C. Gharagouzloo, A. Kas, K. A. Johnson, G. El Fakhri, and M. D. Normandin, "Evaluation of pharmacokinetic modeling strategies for in-vivo quantification of tau with the radiotracer [18F] MK-6240 in human subjects," European Journal of Nuclear Medicine and Molecular Imaging, vol. 46, no. 10, pp. 2099–2111, Sep. 2019.

[141] T. J. Betthauser, K. A. Cody, M. D. Zammit, D. Murali, A. K. Converse, T. E. Barnhart, C. K. Stone, H. A. Rowley, S. C. Johnson, and B. T. Christian, "In Vivo characterization and quantification of neurofibrillary tau PET radioligand [18F] MK-6240 in humans from Alzheimer disease dementia to young controls," Journal of Nuclear Medicine, vol. 60, no. 1, pp. 93–99, May 2018.

[142] B. J. Hanseeuw, R. A. Betensky, H. I. L. Jacobs, A. P. Schultz, J. Sepulcre, J. A. Becker, D. M. O. Cosio, M. Farrell, Y. T. Quiroz, E. C. Mormino, R. F. Buckley, K. V. Papp, R. A. Amariglio, I. Dewachter, A. Ivanoiu, W. Huijbers, T. Hedden, G. A. Marshall, J. P. Chhatwal, D. M. Rentz, R. A. Sperling, and K. Johnson, "Association of amyloid and tau with cognition in preclinical Alzheimer disease," JAMA Neurology, vol. 76, no. 8, pp. 915-924, Aug. 2019.